University of Nairobi

School of Engineering

PARTIAL ISOTHERMAL SECTIONS OF THE COPPER-RICH CORNER OF THE Al-Cu-Zn SYSTEM AT 200ºC AND 240ºC

BY

Johnson Ngugi

F56/76357/2014

A thesis submitted in partial fulfilment of the requirements for the degree of Master of Science in Mechanical Engineering, in the Department of Mechanical and Manufacturing Engineering of the University of Nairobi

June 2017

DECLARATION

I declare that this thesis is my original work and has not been submitted elsewhere for examination, award of a degree or publication. Where other people's work or my own work has been used, this has properly been acknowledged and referenced in accordance with the University of Nairobi's requirements.
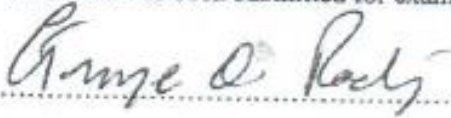
....   29/06/2017

Johnson Ngugi   Date

This thesis has been submitted for examination with our approval as university supervisors.

....   29 – 06 – 2017

Prof. G. O. Rading   Date

University of Nairobi

....   4/8/2017

Prof. L.A. Cornish   Date

University of the Witwatersrand

....   07/07/2017

Dr B.O. Odera   Date

Cape Peninsula University of Technology

DEDICATION

To my mother, Wanjiku Ngugi, for your fervent prayers and impeccable support throughout this journey.

ACKNOWLEDGEMENTS

Anti-Plagiarism Statement

I would like to confirm that this thesis has been written by me and in my own words, except where otherwise explicitly acknowledged. I am aware that the incorporation of material from other works or paraphrase of such material without acknowledgement will be treated as plagiarism, subject to the custom and usage of the subject, according to the University Regulations on Conduct of Examinations.

....

Johnson Ngugi

29/06/2017

Date

ABSTRACT

The Al-Cu-Zn alloy system is well-used because it has demonstrated many useful properties. Currently, Al-Cu-Zn alloys are primarily used as shape memory alloys. Other applications are in catalysis, in electronics and in the manufacture of metal matrix composites. They have also shown great potential to replace the brittle and high-cost Bi and Ni-based solders in applications of up to 350ºC.

The phase equilibria of this system have been the subject of extensive theoretical and experimental assessment since early 20th Century. Some of the features assessed are the liquidus surface, isothermal sections and thermodynamic descriptions using calculation of phase diagrams method. The isothermal sections at 200ºC and 240ºC are incomplete at their copper-rich corners and form the basis for this research.

In this work, 10 ternary alloys with compositions around the copper-rich corner were cast in induction furnaces and each cut into two, sealed in vacuum ampoules and homogenised at 370ºC for 10 days. Then, one set was annealed at 200ºC, and the other set at 240ºC for 28 days. All samples were ground and polished for metallographic examination. Finally, the microstructures of the alloys were characterised using scanning electron microscopes and an energy-dispersive X-ray spectrometer.

Partial isothermal sections at 200ºC and 240ºC were plotted up to 85 at.% Zn and 55 at.% Al. Eight phases were identified at both 200ºC and 240ºC, namely: the binary phases (αCu), γ Cu_9Al_4, η_2 CuAl, γ Cu_5Zn_8, ζ_2 $Cu_{11}Al_9$ and ε $CuZn_4$, and the ternary phases τ $Cu_5Zn_2Al_3$ and τ′ Cu_3ZnAl_4. The γ phase was found to exist as two distinct phases, that is, γ Cu_9Al_4 and γ Cu_5Zn_8. The α_2 Cu_4Al, δ Cu_8Al_5 and β CuZn phases were not observed in any alloy.

The ranges of composition of the τ $Cu_5Zn_2Al_3$, τ' Cu_3ZnAl_4 and ε $CuZn_4$ phases found in this work at 200ºC, and the solubility limit of Al in ε $CuZn_4$ at 240ºC differed with those reported in earlier studies.

NOMENCLATURE

α   Alpha phase

β   Beta phase

γ   Gamma phase

δ   Delta phase

ε   Epsilon phase

η   Eta phase

ζ   Zeta phase

τ   Tau phase

τ′   Tau prime phase

ABREVIATIONS

Am_{Al}	Atomic mass of aluminium
Am_{Cu}	Atomic mass of copper
Am_{Zn}	Atomic mass of zinc
$At.\%_{Al}$	Atomic percent of aluminium
$At.\%_{Cu}$	Atomic percent of copper
$At.\%_{Zn}$	Atomic percent of zinc
BSE	Back-scattered electrons
CALPHAD	Calculation of phase diagrams
CSIR	The Council for Scientific and Industrial Research
DTA	Differential thermal analysis
EDS	Energy-dispersive X-ray spectroscopy
FIB	Focused ion beam
Mintek	The Council for Mineral Technology
NMISA	National Metrology Institute of South Africa
SEM	Scanning electron microscope
SE	Secondary electrons
SMA	Shape memory alloy
XRD	X-Ray Diffraction

TABLE OF CONTENTS

LIST OF FIGURES

LIST OF TABLES

1. INTRODUCTION

1.1. Background Information

The Al-Cu-Zn ternary system is an important alloy system as it forms the basis for many technologically significant alloys [1]. The scope of application of these alloys is also growing [2]. Currently, Al-Cu-Zn alloys with β CuZn are commercially used as shape memory alloys (SMAs) because they undergo reversible martensitic transformations which impart shape memory behaviours [3, 4]. Al-Cu-Zn alloys are also used as catalysts [5, 6] and as matrices for particle reinforced composites [7]. Several multi-component alloy systems are based on this system; for example, the Al-Cu-Zn-Mg quaternary system from which the high specific strength 7075 Al alloy, which finds wide use in general aerospace and automobile applications, is derived [8].

The phase equilibria of this system have been the subject of considerable experimental and theoretical assessments by many researchers over the years, as reviewed by Liang and Chang [8]. Köster [9] assessed the entire liquidus surface, which was later modified by Arndt and Moeller [10]. Ghosh et al. [1] reviewed all isothermal sections assessed by various researchers until 2002. They range from 200ºC to 700ºC. It is worth noting that those at 200ºC, 240ºC and 300ºC are incomplete at the copper-rich corner.

The thermodynamic description of the system is now well established using CALPHAD (Calculation of Phase Diagrams) after studies by Liang and Chang [8], Liang and Schmid-Fetzer [11] and Miettinen [12]. Liang and Chang [8] gave a full thermodynamic description. However, it was inconclusive as they were limited by insufficient experimental data in the Cu-rich region and near the Al-Cu binary edge, and a general lack of thermodynamic data on the system in the

1

literature at the time. Miettinen [12] carried on with their work but focused on the Cu-rich corner. Liang and Schmid-Fetzer [11] gave a comprehensive reassessment of the entire composition range.

Phase stability and the effect of phase transformations on mechanical properties such as hardness have also been investigated. Chen et al. [13] settled the controversy surrounding the stability of the ternary intermetallic, τ' Cu_3ZnAl_4, phase at low temperatures by showing that the phase is indeed stable at room temperature. Villegas-Cardenas et al. [14] investigated the effect of small additions of copper on hardness in Zn-rich aluminium alloys and observed a positive correlation between the two which they attributed to the formation of copper-containing θ Cu_8Al_5 and τ' Cu_3ZnAl_4 phases.

Al-Cu-Zn alloys with β CuZn microstructures are more economical for use as SMAs than Ni-Ti alloys [1]. They can also be fabricated more easily [15]. However, their complicated ageing effects, coupled with their metastability, both in the parent and the martensitic phases, hinder their reliability and performance above room temperature. Stabilisation of martensite has been proposed as a solution [16]. According to Zhou et al. [15], many researchers have endeavoured to do this. Zhou et al. [15] assessed martensite's ability to order by atom exchange when aged isothermally.

Recently, Al-Cu-Zn alloys have been targeted by Kim et al. [17] for application as lead-free solders in the aerospace, automobile and energy industries for temperatures up to 623K. Kim et al. [17] assessed the potential of Zn-rich Al-Cu-Zn alloys with microstructures containing ϵ $CuZn_4$, (ηZn) and (αAl) phases to replace the brittle and high-cost Bi and Ni-based solders currently in use. The solder candidates chosen were in the range Zn-(4-6 wt%)Al-(1-6 wt%)Cu

with the appropriate melting temperature range of 372–400ºC. They exhibited a high potential to be used as high-temperature, lead-free solders.

In summary, the Al-Cu-Zn system has demonstrated immense potential for alloy development both for present and future use. Therefore, there is a need to continually assess the system to ensure that the latest information is included.

1.2. Problem Statement

As already highlighted, immense effort has gone into the study of the Al-Cu-Zn system [1]. However, there are still gaps in knowledge and contentious areas that require further investigation. To be specific, the isothermal sections reviewed by Ghosh et al. [1] at 200ºC, as assessed by Koster and Moeller [18] and Arndt and Moeller [19], and at 240ºC, as assessed by Gebhardt [20], are still incomplete at their Cu-rich corners as shown in Figures 2.7 and 2.8 respectively. The range of compositions of the Cu-rich phases such α_2 Cu_4Al, β $CuZn$, γ Cu_9Al_4 and γ Cu_5Cn_8 as well as their boundaries with respect to each other, are not known at these temperatures.

1.3. Justification of the Study

Since the Al-Cu-Zn ternary system is the basis for many technologically important alloys whose fields of application are growing, gaining fundamental knowledge of the phases present, their composition ranges and their boundaries at the Cu-rich corner of this system at 240ºC and 200ºC is important.

This information, if acquired, can aid the processes of alloy design/development and heat treatment. For instance, engineers could use this information to predict the microstructure,

3

properties and behaviour of their alloys whose compositions lie within these regions and therefore develop them accordingly.

1.4. Objectives of the Study

1.4.1. General Objective

The general objective of this research is to gain fundamental knowledge of the phase boundaries at the Cu-rich corner of the Al-Cu-Zn ternary system at 240ºC and 200ºC.

1.4.2. Specific Objectives

(i)   To plot a partial isothermal section of the Cu-rich corner (up to 55 at.% Al and 85 at.% Zn) of the Al-Cu-Zn system at 200ºC.

(ii)   To plot a partial isothermal section of the Cu-rich corner (up to 55 at.% Al and 85 at.% Zn) of the Al-Cu-Zn system at 240ºC.

(iii)   To identify the phases present at the Cu-rich corner of the Al-Cu-Zn isothermal sections at 200ºC and 240ºC.

(iv)   To compare the results of this study with the earlier isothermal sections of Koster and Moeller [18] at 200ºC and of Gebhardt [20] at 240ºC.

2. LITERATURE REVIEW

2.1. Introduction

Alloy phase diagrams are important tools for metallurgists, materials engineers, and materials scientists. They are useful in:

a) Development of alloys for specific applications;

b) Design and control of heat treatment procedures to develop suitable microstructures that would in turn produce the required mechanical properties for a particular application;

c) Alloy fabrication into the final shape for use; and

d) Providing solutions to problems that arise in specific alloys during their performance in industrial applications, thus improving product predictability [21].

The focus of this research is on the Al-Cu-Zn ternary system. Before this system can be fully described, it is important to first understand its respective binary phase diagrams, that is, the Al-Cu, the Al-Zn, and the Cu-Zn systems.

2.2. Binary Systems

This section summarises available literature on the binary systems of Al-Cu-Zn.

2.2.1. Aluminium-Copper System

The Al-Cu system has been the subject of extensive investigation. Most investigations have focused on the Al-rich part, due to the importance of Al-based alloys in the transport industry [22]. The most widely accepted complete assessment of this binary system is that of Murray [23] published in 1985 and is shown in Figure 2.1 [23]. Murray [23] described the equilibrium phase diagram and provided information on metastable phase equilibria. The system contains 12

intermetallic compounds (θ CuAl$_2$, η_1 CuAl, η_2 CuAl, ζ_1 Cu$_{11}$Al$_9$, ζ_2 Cu$_{11}$Al$_9$, ε_1, ε_2, γ_0, γ_1 Cu$_9$Al$_4$, β_0, β Cu$_3$Al, and α_2 Cu$_4$Al), seven of which are stable only at high temperatures (η_1 CuAl, ζ_1 Cu$_{11}$Al$_9$, ε_1, ε_2, γ_0, β_0 and β Cu$_3$Al). More recent investigations have been done by Liu et al. [24] in 1998, Riani et al. [25] in 2004 and Ponweiser et al. [26] in 2011. Liu et al. [24] reassessed the Cu-rich part, Riani et al. [25] combined the work of Liu et al. [24] and Murray [23], and Ponweiser et al. [22] gave a comprehensive reassessment of the system shown in Figure 2.2 [22]. The thermodynamic description of the system was given by Saunders [26].
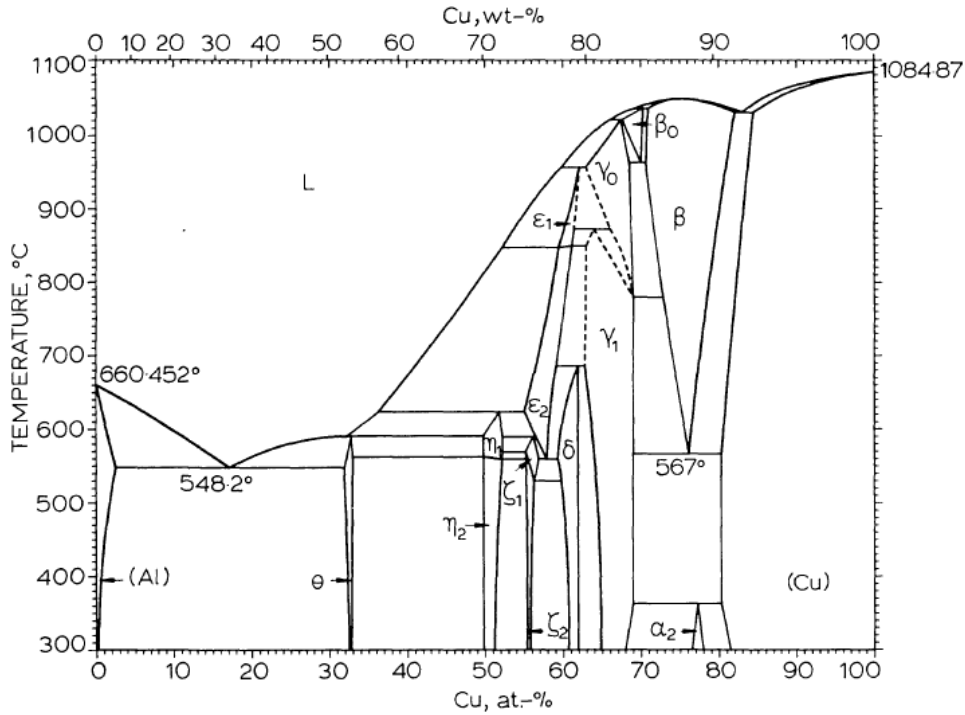
Figure 2.1: Al-Cu phase diagram by Murray [23].

There is complete agreement by all researchers on the phase equilibrium data in the Al-rich region. Friaf [27] investigated the structure of the binary phase θ CuAl$_2$ in 1927 and observed a tetragonal structure. According to Ponweiser and Richter [28], θ CuAl$_2$ shows thermal stability

6

up to between 590ºC and 592ºC where it decomposes peritectically. Additionally, this phase has a composition of 32.4 at.% Cu at 592ºC [28].

Preston [29] carried out structural investigations of the compound η CuAl and found an orthorhombic structure in a sample quenched from 602ºC. Bradley et al. [30] studied slowly cooled samples of the same composition but noted some basic differences in the orthorhombic crystal structure reported by Preston [29]. Bradley et al. [30] proposed two η structures (η_1 CuAl and η_2 CuAl) with an allotropic transformation $\eta_1 \rightarrow \eta_2$ and suggested a monoclinic or orthorhombic structure for the low-temperature phase, η_2 CuAl. El-Boragy et al. [31] found the structure of the low-temperature phase, η_2 CuAl, to be monoclinic. Lukas and Lebrun [32] agreed with Preston [29] by suggesting an orthohombic structure for the high-temperature phase, η_1, with lattice parameters: $a = 4.087$ Å, $b = 12.00$ Å and $c = 8.635$ Å. Ponweiser et al. [22] confirmed the orthohombic structure of the η_1 CuAl phase with slightly different lattice parameter, $a = 4.1450(1)$ Å, $b = 12.3004(4)$ Å and $c = 8.720(1)$. Ponweiser et al. [22] also used differential thermal analysis (DTA) to show that $\eta_1 \rightarrow \eta_2$ is a first order transition.

The high-temperature ε_1 and ε_2 phases were first determined by Stockdale [33] in 1924. El-Boragy [31] later used high-temperature powder X-Ray diffraction (XRD) to study the structure of ε_2 and found a NiAs-type (B8$_1$ or hexagonal) structure with the partial occupation of interstitial positions. Liu et al. [24] confirmed this structure. According to Ponweiser et al. [22], the structure of ε_1 was yet to be solved in 2011. The phase diagrams given by Murray [23] and Liu et al. [24] suggest that $\varepsilon_1 \rightarrow \varepsilon_2$ is a high order transition.
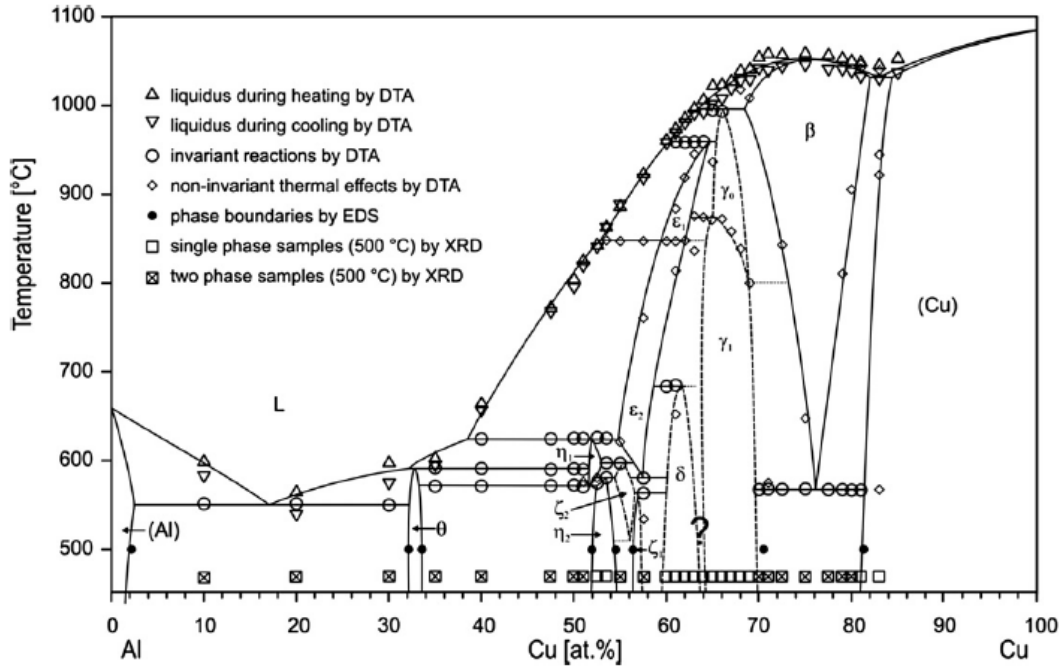
Figure 2.2: Al-Cu system by Ponweiser et al. [22].

Preston [29] and Bradley et al. [30] described the region near the compounds ζ_1 $Cu_{11}Al_9$ and ζ_2 $Cu_{11}Al_9$ which are high-temperature and low-temperature modifications. A transition temperature between 530°C and 570°C was suggested by Murray [23], depending on the composition of the phase. Gulay and Harbrecht [34] solved the crystal structures of the ζ_1 $Cu_{11}Al_9$ and ζ_2 $Cu_{11}Al_9$ phases. A sample with the composition $Al_{42.5}Cu_{57.5}$ (at.%) showed an fcc structure (*Fmm*2, Al_3Cu_4-type) designated as ζ_1 $Cu_{11}Al_9$, while the ζ_2 $Cu_{11}Al_9$ phase (*Imm*2, Al_3Cu_4-δ-type) was found in a sample with the nominal composition $Al_{43.2}$ $Cu_{56.8}$ (at.%). This contradicted the results of Dong et al. [35] who had earlier found that the structure with the lower Cu content had a face-centred symmetry. Gulay and Harbrecht [34] further found that the Cu-rich phase, ζ_1 $Cu_{11}Al_9$, was stable at 400°C which disagreed with Murray's [23] results which showed that ζ_1 $Cu_{11}Al_9$ was only stable above 530°C. Ponweiser et al. [22] confirmed Gulay's and Harbrecht's [34] results.

8

Dong et al. [35] found a mixture of an orthorhombic face-centred structure, an orthorhombic body-centred structure and small amounts of γ_1 Cu_9Al_4 in as-cast samples with the composition Al_3Cu_4. Annealing at 500ºC made the face-centred structure the major phase. Bradley et al. [31] reported three different phases in the range from 60 to 70 at.% Cu: a cubic γ_1 Cu_9Al_4, a monoclinic and a rhombohedral phase. Westman [36] found the rhombohedral structure to have the space group $R3m$ and confirmed the existence of a third phase in this region. No researchers included this controversial third phase in their assessed diagrams. It was very difficult to distinguish between two confirmed phases, γ_1 Cu_9Al_4 and δ Cu_8Al_5, as they had very similar XRD patterns [26, 28]. Seshadri and Downie [37] distinguished between these two phases by the abrupt change in expansion coefficients between the γ_1 Cu_9Al_4 and δ Cu_8Al_5 phases.

Ponweiser et al. [22] had a special interest in the transition of the high-temperature phase, γ_0, to the low-temperature phase, γ_1 Cu_9Al_4 since there was no consensus in literature. Differential thermal analyses of samples within that phase field showed very weak thermal effects apparently varying with the composition. No evidence for an invariant decomposition of γ_1 Cu_9Al_4 was observed in any of the samples investigated. Therefore, Ponweiser et al. [22] reached the same conclusion as Liu et al. [24]: the transition $\gamma_1 \rightarrow \gamma_0$ is of a higher order. Ponweiser et al. [22] also carried out structural analysis of a sample with the nominal composition $Al_{32}Cu_{68}$ (at.%) which confirmed the presence of γ_0 (I-$43m$, Cu_5Zn_8-type) and gave a lattice parameter of $a = 8.8692(1)$ Å at 900ºC. The high-temperature phase, γ_1 Cu_9Al_4, also crystallized as a cubic structure of the Cu_5Zn_8-type.

According to Murray [23], β Cu_3Al is a bcc solid solution that is only stable at high temperature having a composition in the range 70.6 – 82 at.% Cu. It melts congruently at about 1049ºC where it has an approximate composition of 75 at.% Cu. Murray [23] included the high-temperature

9

phase, β_0, in his diagram although its existence is yet to be confirmed. Neither Ponweiser et al. [22] nor Liu et al. [24] observed β_0. All DTA effects observed by Ponweiser et al. [22] in this composition area could be explained by the formation of β Cu_3Al and γ_0.

Murray [23] gave a comprehensive overview of the phase fields between γ_1 Cu_9Al_4 and (αCu).This region is dominated by β Cu_3Al and its decomposition to γ_1 Cu_9Al_4 and (αCu). Murray [23] proposed a decomposition temperature of between 560ºC and 575ºC. Sluggishness of the reaction $\beta \leftrightarrow \gamma_1 + (Cu)$ was suggested to account for this spread. The low-temperature phase α_2 Cu_4Al has a face-centred cubic structure with a long-period superlattice structure which is a variant of $L1_2$ and DO_{22} structures [23].

2.2.2. Copper-Zinc System

Owing to its technological significance, the Cu-Zn binary phase diagram has been widely investigated, as reviewed by Kowalski and Spencer [38]. The phase diagram is generally well established, and there are no major disagreements between the systems assessed and reviewed by Raynor [39], Hansen and Anderko [40], Massalski et al. [41], Miodownik [42] and Predel [43]. The only areas that seem unresolved are most phase boundaries at lower temperatures. Figure 2.3 represents the phase diagram assessed by Miodownik [42]. It is similar to the work of Raynor [39]. Roberts-Austen [44] assessed the liquidus. The thermodynamics of the system have also been determined with several descriptions available [45-49].

West [50] reviewed the (αCu) phase. It has an extensive phase field with a maximum zinc content of 38.95 wt% at 454ºC. At the first peritectic temperature of 902ºC, the zinc content is 32.5 wt%. At 150ºC, where the phase boundary has not been established, the zinc content is about 33wt%. Alloys with this phase are ductile and malleable with their colour ranging from red

to golden yellow and paler yellow with a greenish tinge. Predel [43], in his review of the physical properties of the (αCu) phase at 25 at.% Zn, noted anomalies in the specific heat, lattice parameters, calorific measurements, thermoelectric properties, electric resistivity, hardness, X-ray diffraction and heat capacity values by different researchers, which he attributed to order-disorder reactions.
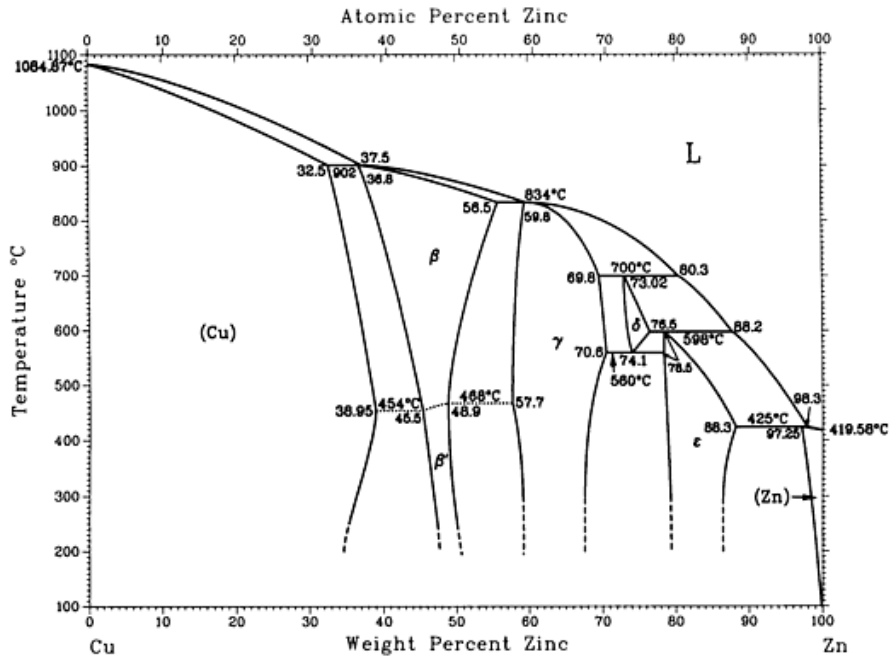
Figure 2.3: Cu-Zn phase diagram by Miodownik [42].

The β CuZn phase has a body-centred cubic crystal structure that results from the first peritectic reaction at 902ºC: L + α → β [50]. Balesdent [51] proposed that the β → β′ transition is not a first order reaction, but an order-disorder reaction. This transition was later confirmed by Walker et al. [52] when they carried out neutron diffuse scattering experiments on mono-crystals containing 53.2 at.% Zn. It, therefore, follows that there is no two-phase region. Whereas β′ CuZn is a super-structure of the CsCI-type (ordered bcc), β CuZn is a bcc structure. The β′ CuZn phase is stable below 454ºC and its lattice parameter at the same temperature and with a

11

composition of 54.8 at.% Zn is $a = 0.2949$ nm. Predel [43] noted that there is no agreement on the temperature at which β′ decomposes.

Von Heidenstamm et al. [53] investigated the structure and lattice parameter of the γ Cu₅Zn₈ phase. It has a Cu₅Zn₈-type cubic structure with: $a = 0.8869$ nm at 500ºC. These observations were confirmed by Iwasaki et al. [54] who further established that there is no change in the structure of γ Cu₅Zn₈ up to a pressure of 20 GPa, with the only notable change being a reduction in the lattice parameter.

The δ CuZn₃ phase is a high-temperature bcc phase of the W structure-type. Its lattice constant was $a = 0.3001$ nm for an alloy with 74.5 at.% Zn at 600ºC [43]. The δ CuZn₃ phase is stable between 558ºC and 700ºC, with maximum solid solution range from about 74 to 77 wt% Zn at 598ºC [55].

The ε CuZn₄ phase has a cph crystal structure. It is stable below 598ºC, with a maximum range at 424°C from about 79 to 87 wt% Zn [43].

The β CuZn, γ Cu₅Zn₈, δ CuZn₃, and ε CuZn₄ phases all melt incongruently [43]. Table 2.1 shows the peritectic and eutectoid reactions in the Cu-Zn system as reported by Tesfaye and Taskinen [55].

Table 2.1: Reactions of the Cu-Zn binary system [55].

Reaction	Composition (at. % Zn)	T (ºC)	Reaction type
α + L ⟷ β	36.1 − 36.8	902	peritectic
β + L ⟷ γ	59.1	834	peritectic
γ + L ⟷ δ	72.45 − 79.8	700	peritectic
δ + L ⟷ ε	78.0 − 87.9	598	peritectic
ε + L ⟷ η	97.17 − 98.25	425	peritectic
δ ⟷ γ + ε	70.0 − 78.0	560	eutectoid

2.2.3. Aluminium-Zinc System

Two different phase diagrams have been published for the system and there is considerable controversy in literature as to which is representative. The first was assessed by Presnyakov et al. [56] in 1961 and modified by Goldak and Parr [57] in 1963 and is shown in Figure 2.4, while the other was reported by Murray [58] in 1985 and is given in Figure 2.5. The controversy surrounds: a peritectic transformation and a second monotectoid reaction at 443ºC and 340ºC respectively, an intermetallic phase, β, between 49.77 at.% Zn and 63.13 at.% Zn at 340ºC, and a narrow two-phase (α′ + β) region at 51.48 at.% Zn at 340ºC. All these four features are present in the diagram modified by Goldak and Parr [57] but conspicuously absent in Murray's [58] diagram.
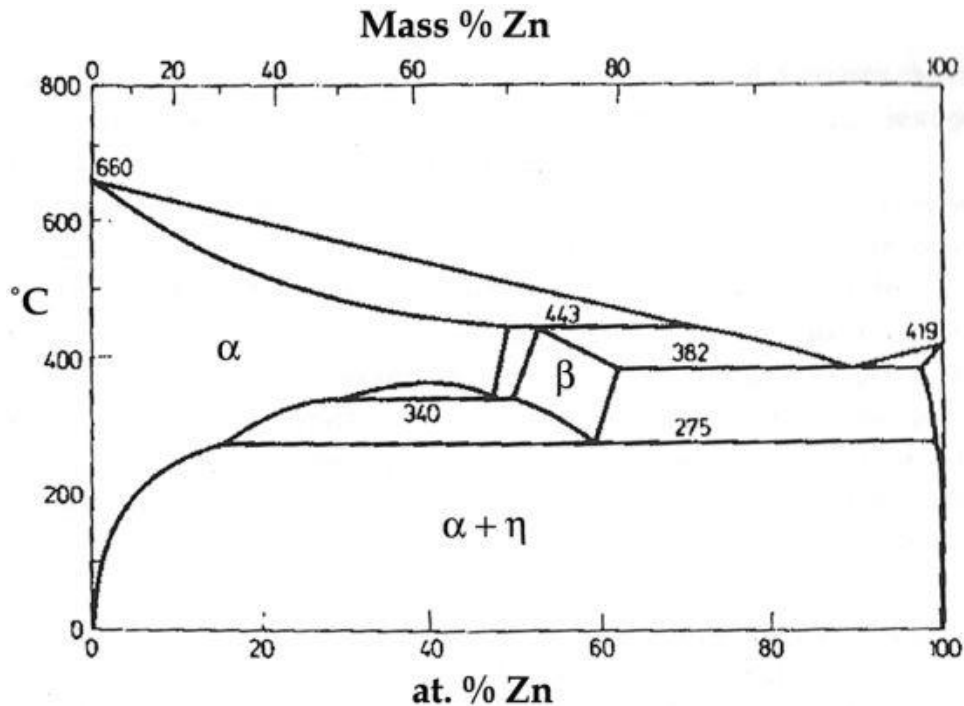
Figure 2.4: Al-Zn binary phase diagram modified by Goldak and Parr [57].

According to Shepherd [59] investigations into the phase equilibria of the Zn-Al system started in the final years of the 19th Century when it was observed that addition of zinc gave aluminium superior casting properties. Shepherd [59] and later Ewen and Turner [60] were the first researchers to report the high-temperature β phase. However, β disappeared in the late 1930s when Owen and Pickup [61] did not observe the phase and the peritectic reaction using high-temperature X-rays. It was not until Presnyakov et al. [56] and Goldak and Parr [57] observed anomalies in lattice parameters at high temperatures that β was reinstated.

Studies by Nayak [62] and Martinez-Flores and Torres Villasenor [63] and Sandoval-Jimenez et al. [64] confirmed the presence of β. Nayak [62], who focused on a small portion of the diagram, observed lattice parameters anomalies at 340ºC that could only be accounted for by an (α + β) two-phase region. Nayak [62] further observed that the lattice constant of β decreased slightly from 0.404 nm to 0.403 nm at 70 wt% Zn and 76 wt% Zn respectively. Martinez-Flores and Torres Villasenor [63], using high temperature X-ray diffraction, observed extra reflections on the diffraction peaks of β at 78.2 wt% Zn which corresponded to a triclinic structure with cell parameters: $a = 0.405057$ nm, $b = 0.403466$ nm, $c = 0.403437$ nm and α = 90.22º, β = 89.99º, γ = 90.23º. They attributed this fcc to triclinic structure transition to a weak distortion of the fcc phase which occurred when the Zn content reached 70.6 wt%.

Sandoval-Jimenez et al. [64] confirmed the triclinic structure of β using high-temperature electron diffraction and high-temperature X-ray diffraction which gave similar cell parameters. Martinez-Flores and Torres Villasenor [63] argued that if β was to be accepted as a separate intermetallic phase, then Presnyakov's [56] diagram would account for all experimental observations. However, Murray [58] did not report β. Murray [58] also quoted the thermodynamic implausibility of having a two-phase region between two structurally identical

14

fcc solid solution phases of virtually equal compositions as strong evidence against the existence of such a region. Since this study will focus on much lower temperatures where there is no significant disparity between the two diagrams; it is beyond its scope to determine which of these two diagrams is correct. However, Murray's [58] diagram will be adopted in this study.
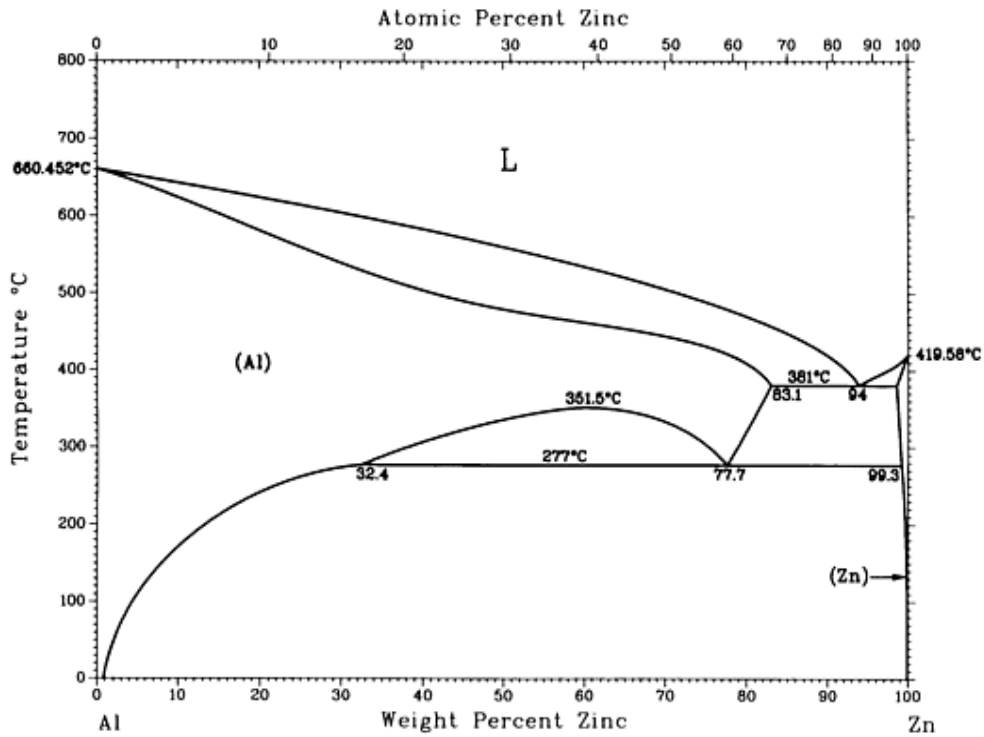
Figure 2.5: Al-Zn phase diagram reported by Murray [58].

In general, the (αAl) solid solution has a fcc crystal structure with an extensive composition range that is interrupted by a miscibility gap [58]. This solid solution is sometimes referred to as either α phase or α' phase in order to differentiate between the Al-rich and the Zn-rich compositions respectively. (ηZn) has a cph structure [58]. (αAl) forms a eutectic with (ηZn) at 381℃ [58]. There is a slight disagreement between Murray [58] and Goldak and Parr [57] on the temperature at which the first monotectoid reaction occurs, that is, 277℃ for Murray [58] and

275ºC from Goldak and Parr [57]. The (Al) solidus curve has an inflection caused by its nearness to the face-centred cubic miscibility gap in regions near equi-atomic compositions [58].

2.3. Al-Cu-Zn System

The phase equilibria of the system have received considerable attention over the years since early twentieth century as reviewed by Ghosh et al. [1]. The entire liquidus surface was first reported by Köster [9] which was later modified Arndt and Moeller [10]. Figure 2.6 represents this liquidus surface projection as reviewed by Ghosh et al. [1]. Ghosh et al. [1] further noted that the liquidus surface that was later given by Wanatabe [65] did not agree with the assessments of Köster [9] and Arndt and Moeller [10]. Miettinen [12] calculated the liquidus surface of the Cu-rich corner using available experimental data.

Figure 2.6: Liquidus surface of the Al-Cu-Zn system [1].

16

Several isothermal sections of the system have been reported. Köster [9] assessed the first isothermal sections at 350ºC. Köster and Moeller [66] reassessed the isothermal section at 350ºC and further reported other sections at 700ºC, 600ºC, 550ºC, 500ºC and 400ºC. Gebhardt [20] evaluated isothermal sections at 350ºC, 300ºC and 240ºC. Arndt and Moeller [19] reported an isothermal section at 650ºC and reassessed those at 700ºC, 600ºC and 550ºC. Arndt and Moeller [10] later gave sections at 350ºC and 200ºC.

Virtually all isothermal sections by the above researchers are in agreement. It is worth mentioning that Cu-rich corners of most of these sections were incomplete and were completed with isothermal data derived from the earlier works of Bauer and Hansen [67-69]. However, the Cu-rich corners of the isothermal sections at 200ºC, 240ºC, and 300ºC are largely unresolved. These sections are given in Figure 2.7 [1], Figure 2.8 [1] and Figure 2.9 [1] respectively. The original works of Köster and Moeller [19] and Gehardt [20] at 200ºC and 240ºC respectively are given in Figures 2.10 and 2.11. Figure 2.12 [1] is a complete isothermal section at 350ºC.

The latest experimental isothermal section assessment of the system was done by Murphy [70]. Murphy [70] studied the solid-phase reactions occurring at the low copper part of the Al-Cu-Zn system and assessed Al-rich isothermal sections at 350ºC, 290ºC, 280ºC, 270ºC, and 250ºC.

Thermodynamic descriptions have been done by Liang and Chang [8], Liang and Schmid-Fetzer [11] and Miettinen [12]. Most of the calculated models by Liang and Chang [8] agreed with the experimental data assessed by Borggren and Selleby [71], although there were significant discrepancies in the liquidus projections. Liang and Chang's [8] description was limited in scope since they were restricted by insufficient experimental data in the Cu-rich region and near the Al-Cu binary edge, and a general lack of thermodynamic data on the system in the literature at the

17

time. Miettinen [12] optimized the thermodynamic description of the Cu-rich corner, although according to Liang and Schmid-Fetzer [11], Miettinen's [12] description could not accurately reproduce the constituent binary diagrams. The description reported by Liang and Schmid-Fetzer [11] is recent and represents a reassessment of Liang and Chang's [8] earlier work, and cover the entire composition range.
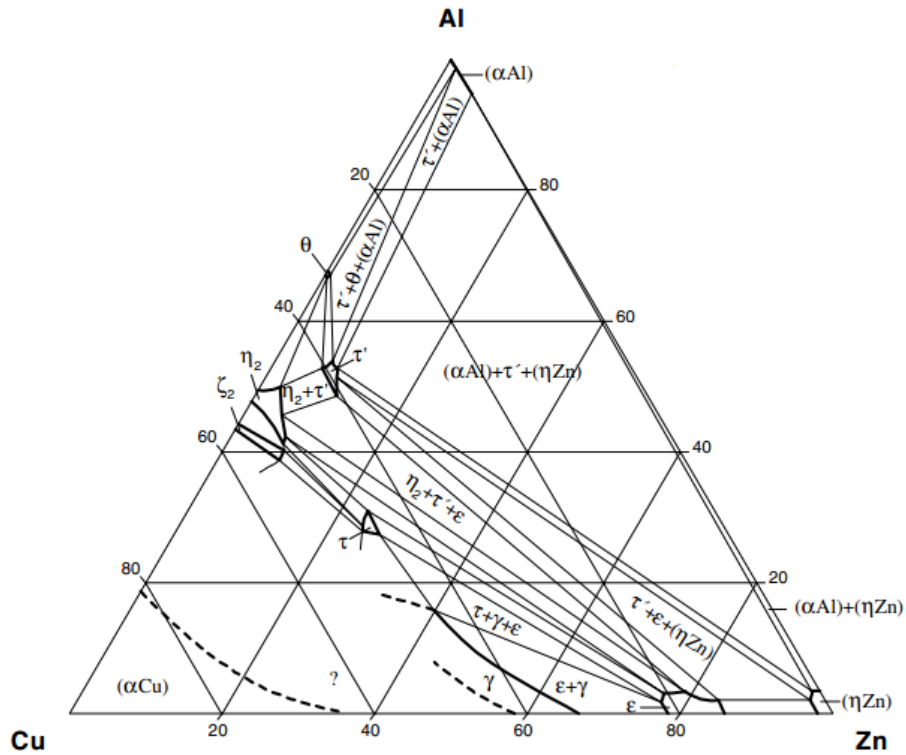
Figure 2.7: Isothermal section of the Al-Cu-Zn system at 200ºC (at.%) [1].

Van et al. [72] determined the thermodynamic properties of the ternary alloys containing 25 to 62 at.% Al via electromotive force measurements between 420ºC and 920ºC in an aluminium concentration cell.

18
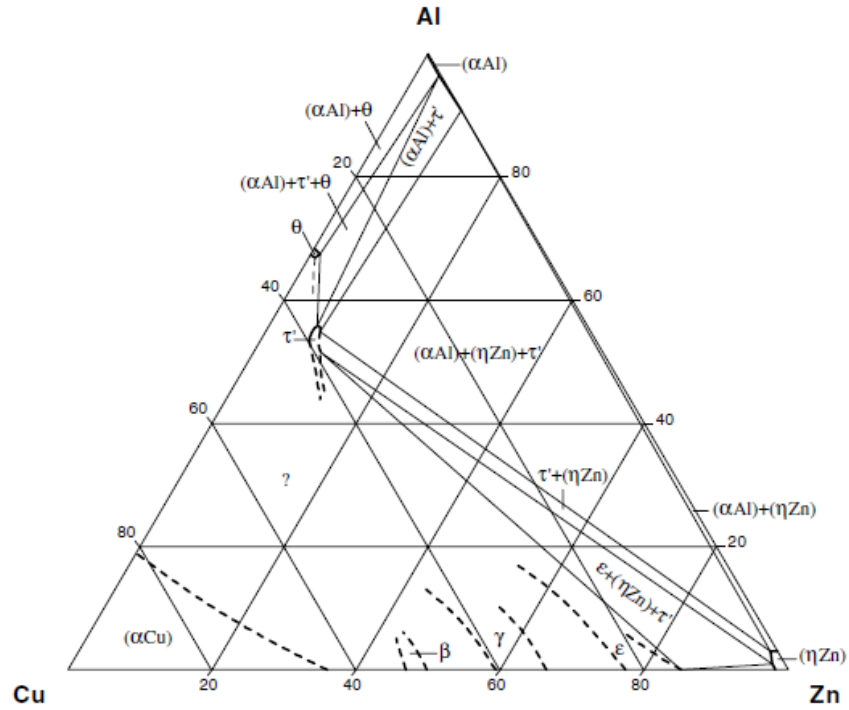
Figure 2.8: Isothermal section of the Al-Cu-Zn system at 240ºC(at.%) [1].
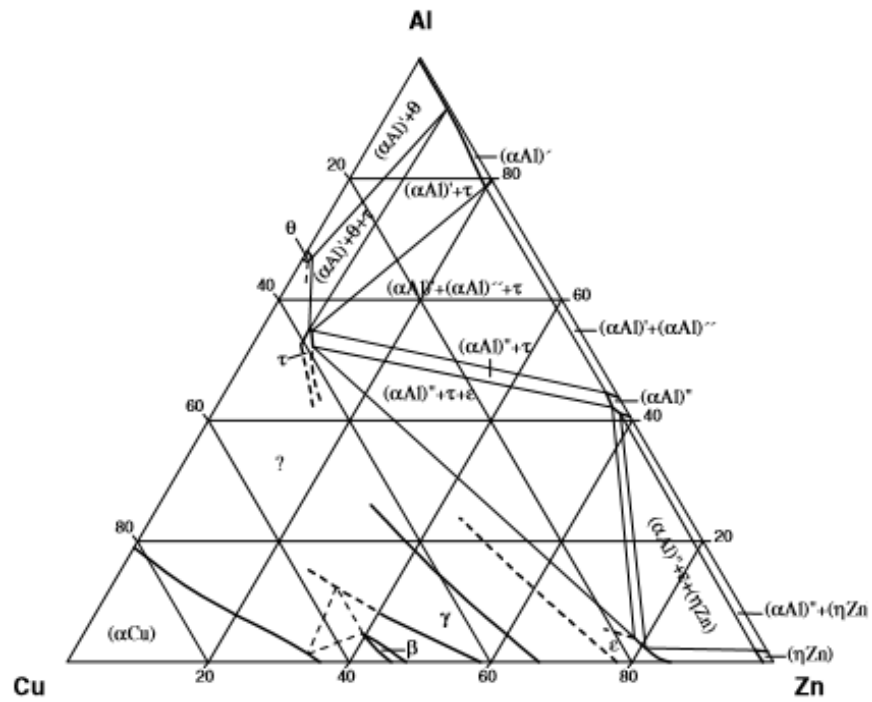
Figure 2.9: Isothermal section of the Al-Cu-Zn system at 300ºC (at.%) [1].

19

Figure 2.10: Isothermal section of the Al-Cu-Zn system at 200ºC by Köster and Moeller [19] (wt%).

Figure 2.11: Isothermal section of the Al-Cu-Zn system by Gebhardt [20] at 240ºC (wt%).

20
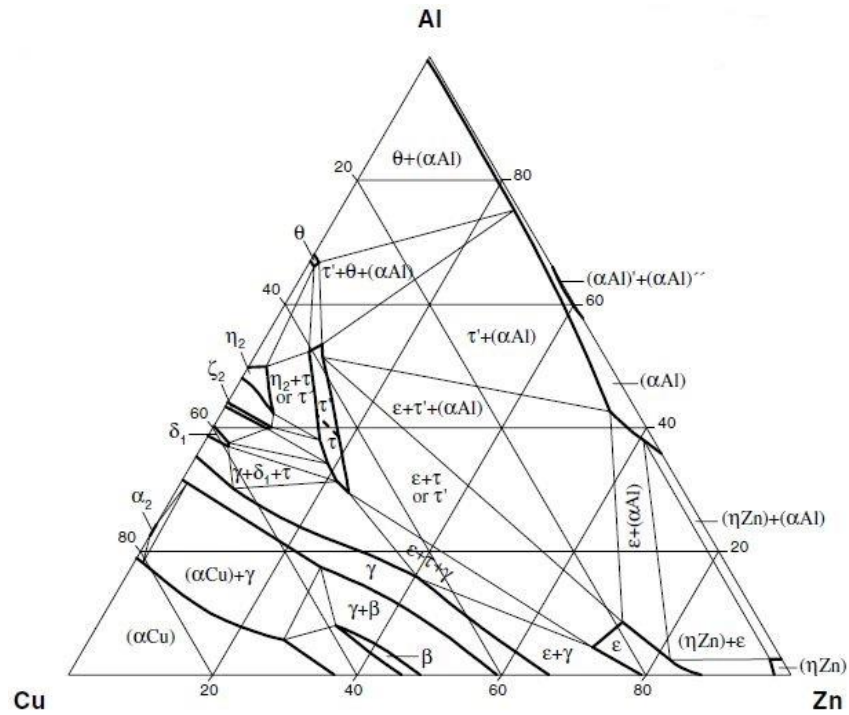
Figure 2.12: Isothermal section of the Al-Cu-Zn system at 350ºC [1].
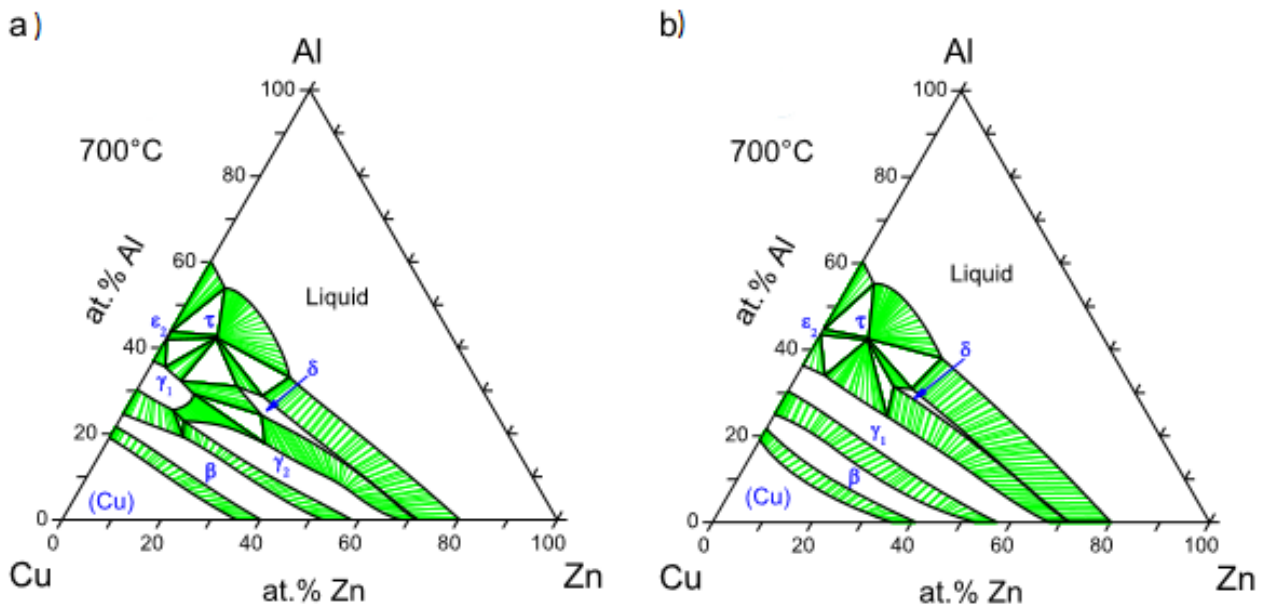
Figure 2.13: Isothermal sections of Al-Cu-Zn at 700ºC: a) by Liang and Schmid-Fetzer [11]; b) by Liang and Chang [8].

21

The solid phase equilibria are well established. Generally, the solubility of Cu in (αAl) increases with an increase in Zn content in the θ Cu_8Al_5 phase. However, the opposite is true in the (αAl) + τ $Cu_5Zn_2Al_3$ two-phase field [1].

Gebhardt [73] and Phillips [74] agree on the solid solubility of Cu in (αAl) at 240ºC, 300ºC, and 350ºC. However, the solid solubility of Zn in (αAl) is considerably higher in Gebhardt's [73] results than Phillips' [74]. Hume-Rothery [75] used the electron concentration factor to determine the solid solubility of Al and Zn in (αCu). When he added Al to Cu-Zn alloys, he observed that the solubility range of (αCu) against β CuZn did not increase, but remained at a constant electron concentration, over a wide range of compositions. Conversely, when he added Zn to Al-Cu alloys, he detected an immediate departure of the solubility range from the simple concentration rule. Murphy [70] and Gebhardt [20, 73] reported the solid solubility of Al and Cu in (ηZn). They agreed that at 375ºC, the maximum solubility is about 1.3 wt% Al and 2.8 wt% Cu and at 275ºC the maximum solubility is about 0.8 wt% Al and 1.7 wt% Cu.

The β phase is disordered and exhibits a *cI*2, W structure at elevated temperatures which transforms to the ordered CsCI or Fe_3C-type structure at low temperatures. It shows a continuous series of intermetallics from β Cu_3Al to β CuZn [1]. Although Bauer and Hansen [67] did not actually study the single phase γ phase, they proposed that it forms a continuous series of solid solutions from the Al-Cu side (γ Cu_9Al_4, cP52 structure) to the Cu-Zn side (γ Cu_5Zn_8, cI52 structure) at elevated temperatures. This proposition was cited in several subsequent works [8-10, 19, 20 and 66].

However, a recent review of the γ phase by Liang and Schmid-Fetzer [11] disputes this interpretation on the basis of studies by Köster and Moeller [76], which reported both Zn-rich γ phase (γ Cu_5Zn_8) and Zn-poor γ phase (γ Cu_9Al_4), and Kandaurov et al. [77] and Ashrimbetov et al. [78] which reported a two-phase region between γ Cu_9Al_4 and γ Cu_5Zn_8. In their re-examination, Liang and Schmid-Fetzer [11] confirmed the presence of γ Cu_9Al_4 in the Al-Cu side and γ Cu_5Zn_8 in the Cu-Zn side. This disagreement is illustrated by Figure 2.13. Figure 2.13 (a) and Figure 2.13 (b) are isothermal sections at 700ºC evaluated by Liang and Schmid-Fetzer [11] and Liang and Chang [8] respectively. Whereas there are two γ phases ($γ_1$ and $γ_2$) in Figure 2.13 (a), there is only one γ phase in Figure 2.13 (b) and it is continuous.

Köster [9] and Köster and Moeller [76] originally assumed that $η_1$ CuAl, τ $Cu_5Zn_2Al_3$, τ′ Cu_3ZnAl_4, δ Cu_8Al_5 and $ε_2$ phases had one common field of homogeneity at elevated temperatures. However, Arndt and Moeller [10] later contradicted these assumptions. The $η_1$ CuAl and τ $Cu_5Zn_2Al_3$ phases were found to be different phases at all temperatures, while $ε_2$ and δ Cu_8Al_5 phases had different crystal structures and thus it is very unlikely to form a continuous series of solid solutions. Complete solubility between the $ε_2$ phase of the Al-Cu binary system and the δ Cu_8Al_5 phase of the Cu-Zn binary system above 680ºC has been proposed by Köster [9] and Arndt and Moeller [10].

Köster [9] observed that the θ $CuAl_2$ phase could dissolve up to 2 to 3 wt% Zn without significantly affecting its lattice parameters and properties. In addition, Köster [9] noticed that the ε $CuZn_4$ phase could dissolve up to about 12 wt% Al at about 600ºC with the solubility decreasing with decreasing temperature.

Arndt and Moeller [10] found that at temperatures below 250ºC, the ternary phase, τ $Cu_5Zn_2Al_3$, had two separate ranges of homogeneity, that is, τ $Cu_5Zn_2Al_3$ and τ' Cu_3ZnAl_4. These different structures do not necessarily exclude a single range of homogeneity at higher temperatures owing to the fact that τ' Cu_3ZnAl_4 phase has a *hR*9 structure which is a superstructure of the CsCl-type with ordered vacancies. Whereas τ $Cu_5Zn_2Al_3$ is formed via a univariant peritectic reaction between ε_2 and the liquid at about 740ºC, the τ' Cu_3ZnAl_4 phase appears between 600ºC and 550ºC close to the Al-rich end of the homogeneity range of the τ $Cu_5Zn_2Al_3$ phase. Table 2.2 shows the crystallographic data of the solid phases of this system [1].

In conclusion, the Al-Cu-Zn system is widely researched having received attention since 1911 as reviewed by Köster and Moeller [76]. However controversies and gaps in knowledge still exist. Most controversy surrounds the nature of the γ phase with different results published. Whereas studies by researchers such as Köster and Moeller [76], Kandaurov et al. [77] and Ashrimbetov et al. [78] reported both γ Cu_9Al_4 and γ Cu_5Zn_8 phases, others [8-10, 19, 20 and 66] reported a continuous phase field of single phase γ from the Cu-Zn side to the Al-Cu binary side.

The most notable gaps are in the isothermal sections. The isothermal sections at 200ºC, 240ºC and 300ºC are incomplete at their Cu-rich corners. The present work is an attempt to provide isothermal data at the Cu-rich corner of the system at 200ºC and 240ºC up to 55 at.% Al and 85 at.% Zn.

Table 2.2: Crystallographic information of the Al-Cu-Zn system solid phases [1].

Phase/ Temperature Range [°C]	Pearson Symbol/ Space Group/ Prototype	Lattice Parameters [pm]	Comments/References
(αAl) $\leq$ 660.452	$cF4$ $Fm\bar{3}m$ Cu	$a = 404.96$	pure Al at 25°C, [Mas2] dissolves up to 2.48 at.% Cu at 548.2°C [2003Gro]
(αCu) $\leq$ 1084.87	$cF4$ $Fm\bar{3}m$ Cu	$a = 361.48$	pure Cu at 25°C, [V-C] dissolves up to 19.7 at.% Al at 559°C [2003Gro]; disolves up to 35.84 at.% Zn at 300°C [2003Leb]
(ηZn) $\leq$ 419	$hP2$ $P6_3/mmc$ Mg	$a = 266.46$ $c = 494.61$	pure Zn at 22°C, [V-C] dissolves up to 1.5 at.% Cu at 424°C [2003Leb]
θ, $CuAl_2$ $\leq$ 591	$tI12$ $I4/mcm$ $CuAl_2$	$a = 605.0$ $c = 487.0$	from 31.9 to 33.0 at.% Cu at 33.3 at.% Cu, [1985Mur]
η_1, CuAl(h) 624-560	$o*32$	$a = 408.7$ $b = 1200$ $c = 863.5$	49.8 to 52.4 at.% Cu [V-C2, Mas2, 1985Mur] Pearson symbol: [1931Pre]
η_2, CuAl(r) $\leq$561	$mC20$ $C\,2/m$ CuAl(r)	$a = 1206.6$ $b = 410.5$ $c = 691.3$ $\beta = 55.04°$	[1985Mur], from 49.8 to 52.3 at.% Cu
ζ_1, $-Cu_{47.8}Al_{35.5}$(h) 590-530	$oF88 - 4.7$ $Fmm2$ $Cu_{47.8}Al_{35.5}$	$a = 812$ $b = 1419.85$ $c = 999.28$	55.2 to 59.8 at.% Cu, [Mas2, 1994Mur] structure: [2002Gul]
ζ_2, $Cu_{11.5}Al_9$(r) $<$ 570	$oI24 - 3.5$ $Imm2$ $Cu_{11.5}Al_9$	$a = 409.72$ $b = 703.13$ $c = 997.93$	55.2 to 56.3 at.% Cu, [Mas2, 1985Mur] structure: [2002Gul]
ε_1, $Cu_{100-x}Al_x$ 958-848	cubic ? -	-	$37.9 \leq x \leq 40.6$ [1985Mur]
ε_2, $Cu_{1+x}Al$ 850-560	$hP6$ $P6_3/mmc$ Ni_2In	$a = 414.6$ $c = 506.3$	$0.22 \leq x \leq 0.57$ [1985Mur]
δ_1, $Cu_{100-x}Al_x$	$hR*$ -	$a = 869.0$ $\alpha = 89.78°$	$38.1 \leq x \leq 40.7$ [1985Mur]
γ_0, $Cu_{100-x}Al_x$ 1037-800	$cI52$ $I\bar{4}3m$ Cu_5Zn_8-	-	$31 \leq x \leq 40.2$ [1985Mur]
γ, $Cu_5(Cu_xZn_{2-2x}Al_x)_7$	$cP52$ $P\bar{4}3m$	$a = 870.68$	Zn free 69.23 at.% Cu, [V-C2]
γ, Cu_9Al_4 $<$ 890	Cu_9Al_4	$a = 886.9$	Al free [V-C2] Cu_9Al_4 is ordered with Cu and Al on 2nd sites,
γ, Cu_5Zn_8 $<$ 835	$cI52$ $I\bar{4}3m$ Cu_5Zn_8		$cP52$-Cu_9Al_4 type

Phase/ Temperature Range [°C]	Pearson Symbol/ Space Group/ Prototype	Lattice Parameters [pm]	Comments/References
α_2, $Cu_{100-x}Al_x$ ≤ 363°C	$TiAl_3$-type long period super- lattice	$a = 366.6$ $c = 367.5$	$22 \leq x \leq 23.5$ at 77.9 at.% Cu, [1985Mur]
β', CuZn(r) ≤ 468	cP2 $Pm\bar{3}m$ CsCl	$a = 295.9$	at 49.5 at % Zn [V-C2], from 44.8 to 50.0 at.% Zn
δ, $CuZn_3$ 700-560	hP3 $P\bar{6}$ $CuZn_3$	$a = 427.5$ $c = 259.0$	[V-C2], from 72.4 to 76.0 at.% Zn [1985Mur]
ε, $\approx CuZn_4$ ≤ 598	hP2 $P6_3/mmc$ Mg	$a = 274.18$ $c = 429.39$	[V-C2], from 78 to 88.0 at.% Zn
β, (Cu,Zn,Al) β, CuZn(h) 903-454 β, CuAl 1049-559	cI2 $Im\bar{3}m$ W	$a = 299.67$ $a = 285.64$ $a = 294.6$	[V-C2], from 36.1 to 55.8 at.% Zn at 672°C in two-phase field, [1985Mur] at 75.7 at.% Cu, 580°C [1985Mur] solid solubility range: 70.6 to 82.0 at.%Cu
* τ, $\approx Cu_5Zn_2Al_3$ < 740 * τ', $\approx Cu_3Zn$	$\approx cP2$ CsCl hR9	$a = 290.4$ $a = 293.2$ $a = 867.6$ $\alpha = 27.41°$	$Cu_{40}Zn_7Al_{53}$ [1942Koe] at $Cu_{46}Zn_{20}Al_{34}$ [1942Koe] rhombohedral superstructure of 5 CsCl lattice [1942Koe], [1975Mur, 2000Dor]

3. METHODOLOGY

3.1. Sample Preparation

3.1.1. Sample Compositions and Materials

For this study, 12 sample compositions targeting multi-phase regions were selected around the Cu-rich corner of the Al-Cu-Zn ternary triangle. The same 12 samples whose selection was based on the isothermal section at 240ºC in Figure 3.1 were used for isothermal studies at 200ºC.

The atomic percentages were then converted to weight percentages to aid weighing for sample preparation. Equation 3.1 is the formula used to calculate the weight of Cu in 5g of sample alloy.

$$Weight\ of\ Cu\ in\ 5g\ of\ alloy = \frac{(At.\%_{Cu} \times Am_{Cu})}{(At.\%_{Cu} \times Am_{Cu}) + (At.\%_{Zn} \times Am_{Zn}) + (At.\%_{Al} \times Am_{Al})} \times 5g\ \ldots\ldots.Eq.\ 3.1$$

Where:

$At.\%_{Cu}, At.\%_{Zn}$ and $At.\%_{Al}$ are the atomic percentages of Cu, Zn and Al respectively while

$Am_{Cu}, Am_{Zn}, Am_{Al}$ are the atomic mass numbers of Cu, Zn and Al respectively.

The atomic and weight percentage compositions, together with calculated masses of each constituent element required to make a 5-gram alloy, are recorded in Table 3.1.

Pure aluminium (99.9%), copper (99.9%) and zinc (99.9%) pellets were procured from Goodfellow in the United Kingdom. Powders would have been preferred but pellets were more cost effective. The calculated masses of each element required to make 5g samples in Table 3.1 were weighed using an electronic balance with an accuracy of 0.01g and then mixed in preparation for casting.
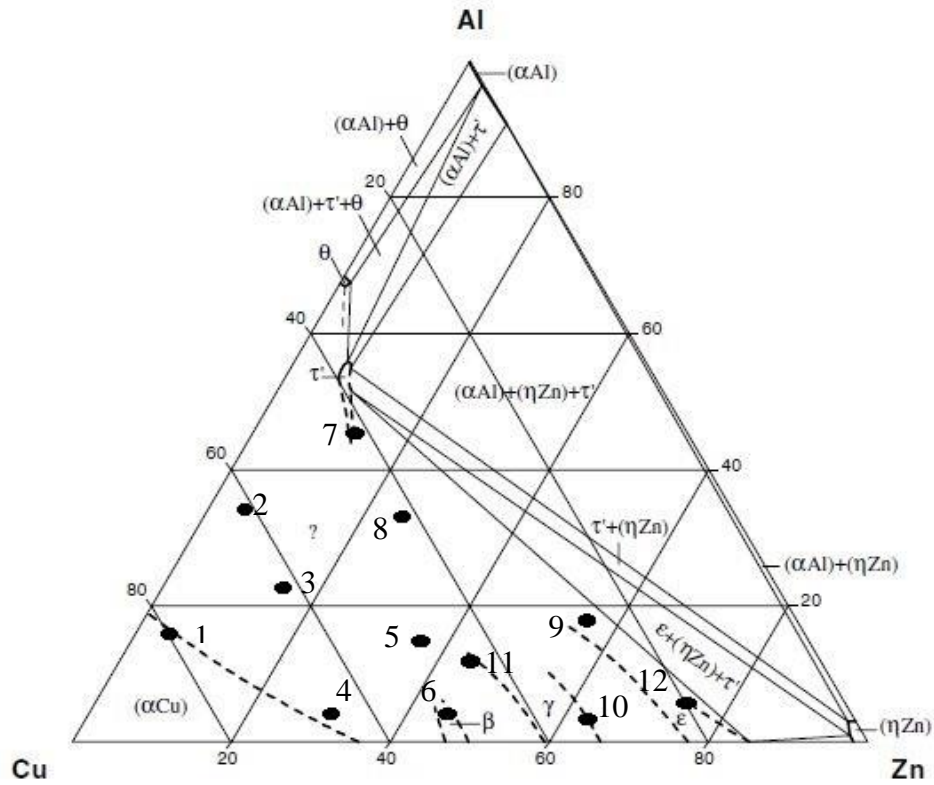
Figure 3.1: Alloy composition locations on the Al-Cu-Zn ternary triangle at 240ºC reviewed by Ghosh [1].

Table 3.1: Selected alloy sample compositions.

SAMPLE	Cu			Zn			Al		
	at.%	wt%	wt in 5g	at.%	wt%	wt in 5g	at.%	wt%	wt in 5g
1	80.0	87.9	**4.394**	4.2	4.8	**0.238**	15.8	7.4	**0.368**
2	62.1	75.7	**3.786**	6.3	7.9	**0.396**	31.6	16.4	**0.818**
3	62.1	69.8	**3.489**	17.9	20.7	**1.034**	20.0	9.5	**0.477**
4	65.8	66.6	**3.330**	30.5	31.8	**1.590**	3.7	1.6	**0.079**
5	50.5	54.6	**2.731**	34.7	38.6	**1.931**	14.7	6.8	**0.338**
6	50.5	51.1	**2.555**	45.3	47.1	**2.355**	4.2	1.8	**0.090**
7	43.0	57.3	**2.865**	13.0	17.8	**0.891**	44.0	24.9	**1.245**
8	45.0	53.9	**2.696**	25.0	30.8	**1.541**	30.0	15.3	**0.763**
9	28.0	30.7	**1.535**	54.0	60.9	**3.046**	18.0	8.4	**0.419**
10	33.0	33.0	**1.648**	64.0	65.8	**3.288**	3.0	1.3	**0.064**
11	43.0	45.8	**2.292**	44.0	48.3	**2.413**	13.0	5.9	**0.294**
12	20.0	20.2	**1.010**	74.0	76.9	**3.847**	6.0	2.9	**0.143**

3.1.2. Sample Casting

3.1.2.1. Arc Melting at the Council for Mineral Technology (Mintek), South Africa

The samples were at first taken to Mintek, South Africa for melting in an arc furnace to make the samples. In preparation, the furnace dome was evacuated to remove oxygen and then argon gas was pumped in. The process was repeated thrice to remove as much oxygen as possible. Prior to melting, a lump titanium metal was melted to react with the remaining oxygen. However, arc melting proved unsuccessful to prepare the samples. Zinc, which has a high vapour pressure, vaporised in all sample compositions (at 907ºC) before copper could melt (at 1085ºC). Therefore, no sample was successfully cast. Figure 3.2 shows the samples in the arc furnace before and after melting.
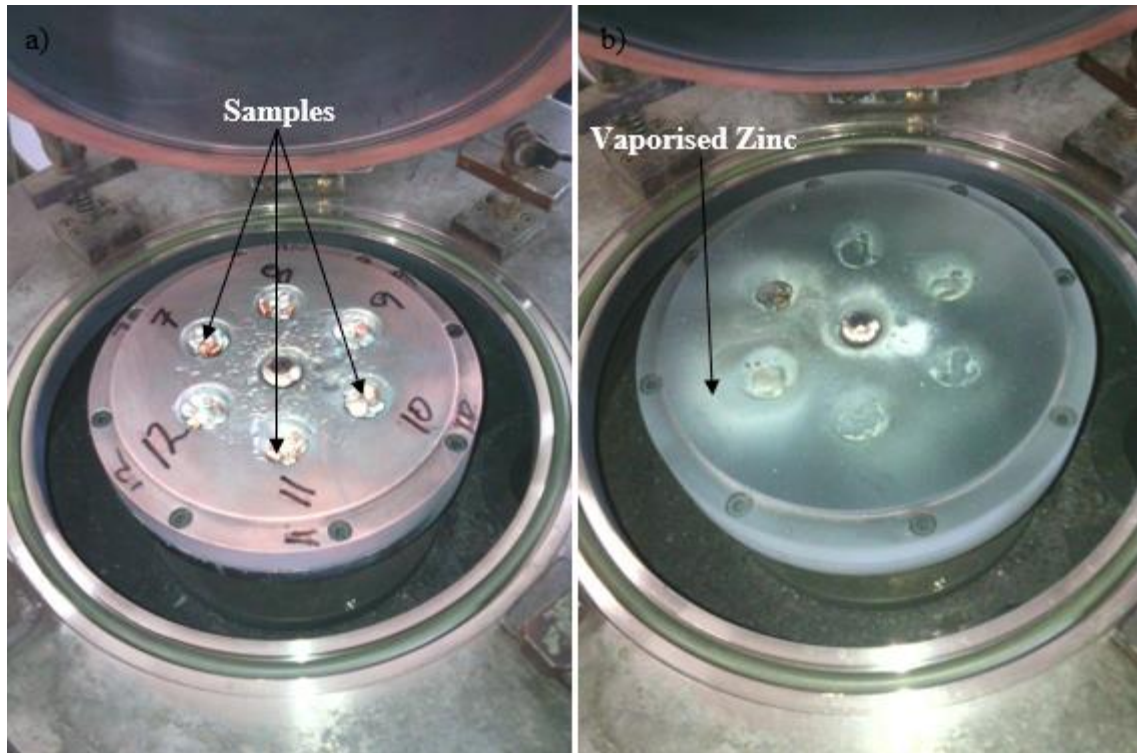
Figure 3.2: Copper hearth of the arc melt at Mintek: a) before melting; b) after melting.

3.1.2.2. Induction Furnace Casting at the School of Chemical and Metallurgical Engineering, University of the Witwatersrand, South Africa

Fresh sample compositions of 10g each were prepared to be melted in a Hot Platinum induction furnace at the School of Chemical and Metallurgical Engineering, University of the Witwatersrand, South Africa. Excess zinc was added to each sample composition to compensate for the expected loss during melting. The induction furnace was evacuated and argon gas flushed in before melting. However, only Samples 1 and 2 were successfully prepared with minor losses. For the rest of the samples, the excess zinc was not enough to avoid the problems encountered in arc melting.

3.1.2.3. Induction Furnace Casting at the Council for Scientific and Industrial Research (CSIR), South Africa

From the first induction furnace attempt, it became obvious that the components would have to be added in stages in an attempt to reduce the losses. In the first trial, the matrix (component with highest composition) was melted first, followed by the smallest component then the other component added last. When this did not work, Zn was melted with Cu to increase the boiling point of the alloy and then Al was added. However, surface tension effect stopped mixing. The crucible and induction coil used at CSIR are shown in Figure 3.3.

The successful method involved melting Cu first, and then adding Al to lower the liquidus of the mixture close to or below the boiling point point of Zn. Zn was added last while stirring the mixture using a ceramic rod to encourage mixing. Since loss of Zn was still experienced, excess Zn was used for all samples to compensate for the losses. Only eight samples were successfully prepared using this method. All attempts made to prepare Samples 4 and 6 were not successful. Since no inert gas was used, oxide contaminations were expected in the samples

30
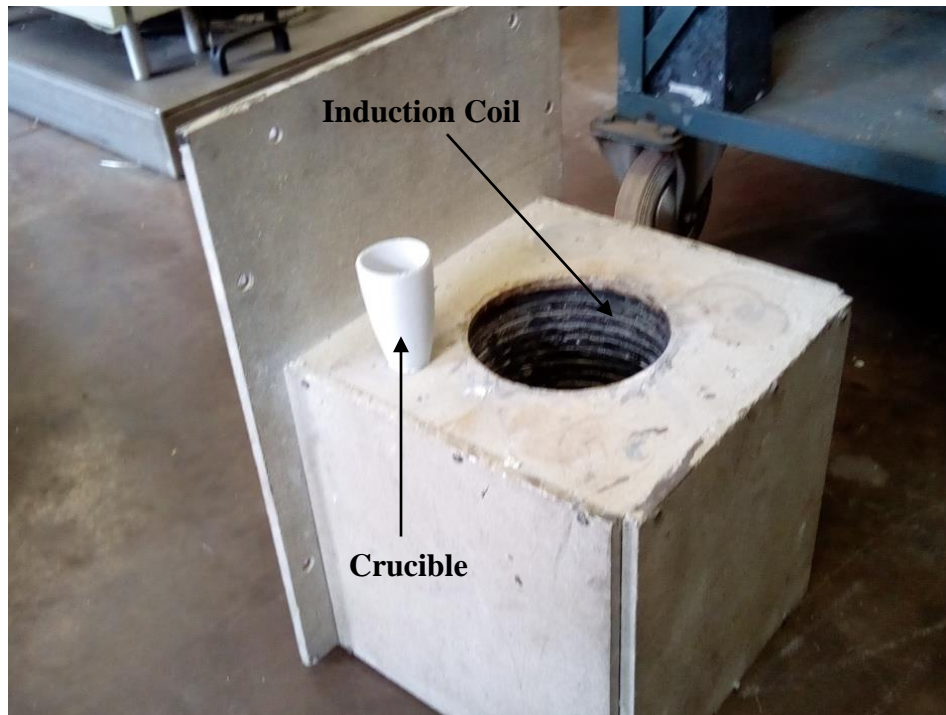
Figure 3.3: Crucible and induction coil used at the CSIR.

3.2. Heat Treatment

Each of the 10 alloy samples was cut into 4 pieces using an SBT (South Bay Technology) Low-Speed Diamond Wheel Saw (Model 650) shown in Figure 3.4 to create 4 separate sets of samples.

Two sets were separately sealed in silica glass tubes using an oxy-acetylene torch as a 2 Pa partial-pressure vacuum pump removed air from the open end to create vacuum ampoules. This was done to prevent oxidation of the alloy samples during heat treatment. The remaining two sets were stored for future use.
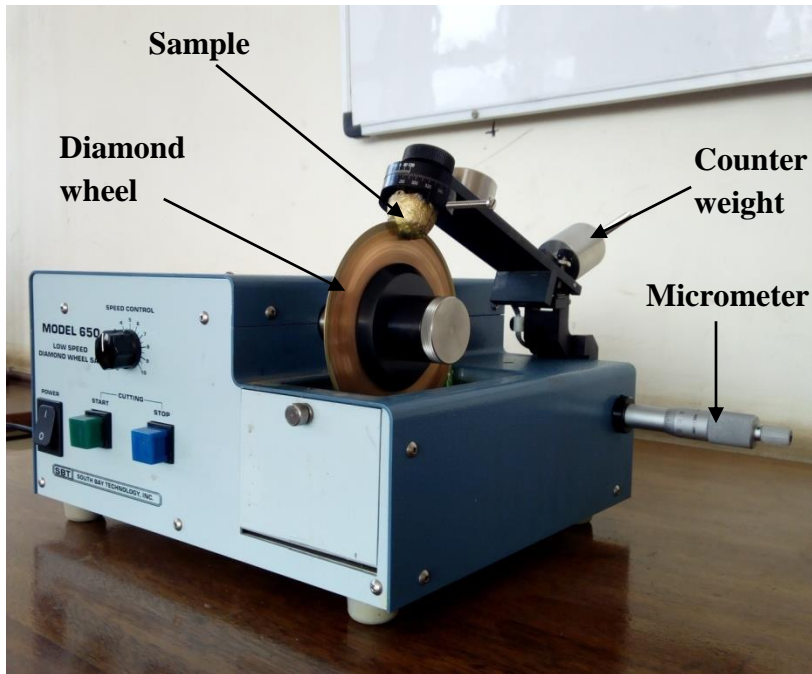
Figure 3.4: SBT (Model 650) low-speed diamond wheel cutter used to section the as-cast alloy samples.

Figure 3.5: Set of vacuum-sealed samples in the Elsklo LN 2 furnace.

The two sets of samples that were separately sealed were homogenised at 370ºC for 10 days (240 hours) in an Elsklo LN 2 muffle furnace shown in Figure 3.5. Each set was then annealed for four weeks; one at 240ºC and the other at 200ºC. Finally, each set was rapidly quenched in cold water to arrest diffusion and the silica glass ampoule broken to retrieve the samples.

3.3. Metallographic Preparation

All alloy samples were first ground on successive grades of emery papers from #600 to #1200 mounted on a couple of rotating disks. Samples were washed each time before moving to the next stage. The emery papers were then replaced by polishing cloths for polishing with 6µm, 1µm and 0.25µm diamond pastes. In between polishing, each sample was washed and viewed under a light microscope to ensure that all scratches were removed prior to SEM/EDS studies. The equipment used for grinding and polishing is shown in Figure 3.6.
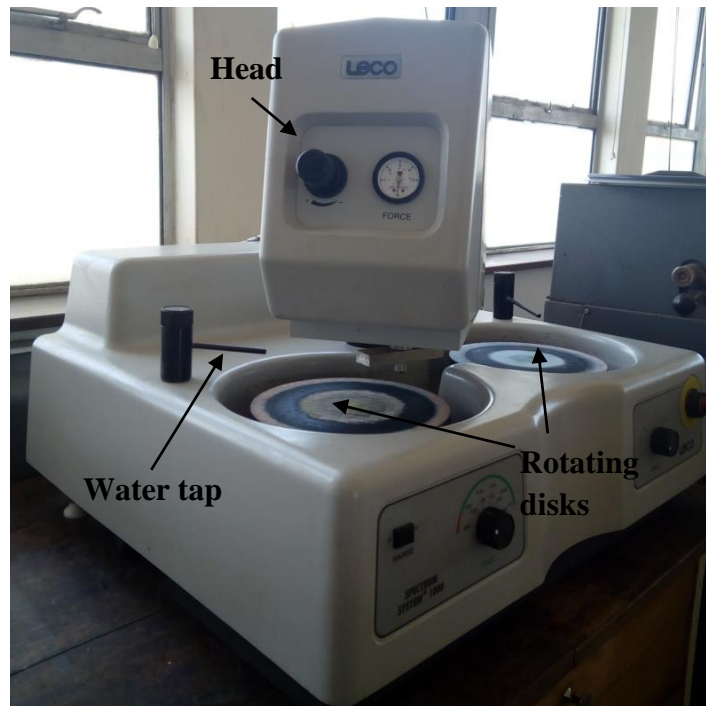
Figure 3.6: Spectrum System 1000 used for grinding and polishing.

3.4. Sample Analysis

Sample analysis was done at the National Metrology Institute of South Africa (NMISA). The primary equipment used for these analyses was a Leo 1525 Field Emission scanning electron microscope (SEM) coupled with an Oxford 15mm^2 Silicon Drift energy-dissipative x-ray spectroscopy (EDS) detector. A Centaurus back-scattered electron (BSE) detector was used to distinguish different phases using their atomic number differences. This SEM/EDS set-up is shown in Figure 3.7.
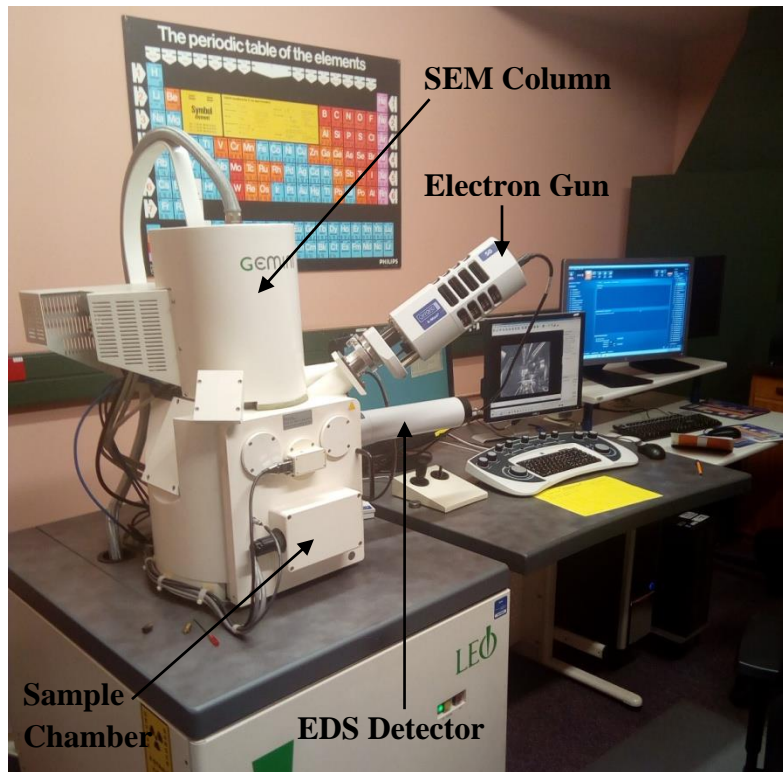
Figure 3.7: Leo 1525 Field Emission SEM/ Oxford 15mm2 Silicon Drift EDS Detector set-up used at NMISA.

All imaging and analyses were done at a voltage of 15kV, a working distance that varied between 15.0 and 16.0 mm, and an aperture size between 60 and 120 µm. At least five analyses were done per phase and an additional 5 overall analyses (at low magnification of $\times 70$) were

done for each sample. The ensuing EDS spectra were interpreted using Aztec EDS Analysis software.

Selected samples that showed poor contrast under the Leo 1525 Field Emission SEM were further analysed using the Crossbeam 540 Focused Ion Beam (FIB) SEM in Figure 3.8.
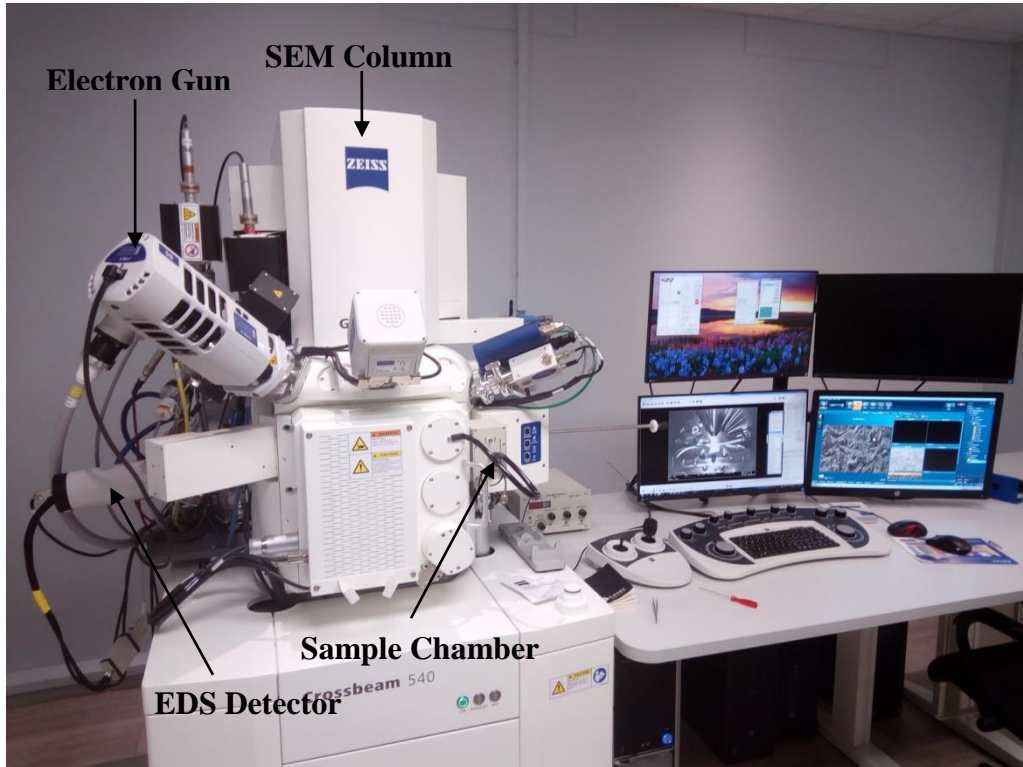
Figure 3.8: Crossbeam 540 FIB-SEM used at NMISA.

3.5. Data Interpretation

Before plotting any EDS data, binary edges at the two isothermal temperatures were plotted from the three respective binary phase diagrams. The binary diagrams used were: Al-Cu by Murray [23], Cu-Zn by Miodownik [42] and Al-Zn by Murray [58].

Then, the average EDS data of each sample (phases and overall) were plotted on the same ternary composition grid. This was done separately for all samples: 10 for alloys annealed at 200ºC, and 10 for alloys annealed at 240ºC. Binary phases present were identified by comparing their composition plots with the composition of known phases of the respective binary diagrams. The ternary τ and τ' phases were identified using the isothermal section at 350ºC reviewed by Ghosh [1].

Finally, the EDS data of every sample annealed at 200ºC were plotted on the same grid. The same was repeated for samples annealed at 240ºC. Since each data point representing a phase lies on a phase boundary, lines were drawn to join data points that were deduced to represent the same phases. Finally, these lines were extrapolated to meet corresponding phase boundaries on the binary edges on the ternary grid where necessary.

4. RESULTS

4.1. Comparison of Targeted and Actual Sample Composition

The actual compositions of the cast samples were compared with their target compositions in Table 4.1 to determine how close the two were.

Table 4.1: Target sample compositions versus actual sample compositions.

Sample	Target Composition (at.%)			Actual Composition (at.%)		
	Al	Cu	Zn	Al	Cu	Zn
1 (a)	15.8	80	4.2	14.9±0.2	68.6±0.2	16.5±0.3
1 (b)	15.8	80	4.2	16±0.2	78.9±0.2	5.1±0.3
2 (a)	31.6	62.1	6.3	27.8±0.3	55.5±0.2	16.6±0.3
2 (b)	31.6	62.1	6.3	19±0.2	74.5±0.3	6.5±0.4
3	20	62.1	17.9	14.3±0.3	42.2±0.3	43.5±0.5
5	14.7	50.5	34.7	13±0.1	36.9±0.2	50.2±0.1
7	44	43	13	41.9±0.4	42.2±0.6	15.9±0.3
8	30	45	25	25.8±0.5	38.9±0.3	35.3±0.8
9	18	28	54	21±1.6	22.3±0.6	56.7±2.0
12	6	20	74	10.9±1.6	17.4±1.5	71.8±1.6

For Samples 1 and 2, (a) denotes the samples that were prepared at CSIR and (b) denotes the samples that were prepared at the School of Chemical and Metallurgical Engineering, University of the Witwatersrand. Samples 3, 5, 7, 8, 9 and 12 were all prepared at CSIR.

Only Sample 1 (b) was close to its target composition. There were significant shifts in composition in all other samples. These shifts was primarily attributed to the use of excess Zn to compensate for the expected Zn loses, and the use of pellets rather than powders. Even though pellets are more cost effective than powders, it was difficult to achieve accurate weight proportions of each constituent element in a sample using pellets.

4.2. Sample Analyses

BSE images were obtained for all samples for phase characterisation. Selected secondary electron (SE) images were obtained for samples with significant porosity. This section contains these images, EDS phase and overall composition data, and subsequent plots on the ternary composition grid.

4.2.1. Alloys Heat-Treated at 200°C

4.2.1.1. Sample 1 (a), Average Composition Al$_{14.9}$Cu$_{68.6}$Zn$_{16.5}$ (at.%)

Sample 1 (a) had a medium grey phase and a fine eutectic as shown in Figure 4.1. The dark grey phase in the eutectic was too small to be analysed independently. Therefore, the eutectic was analysed as areas. The EDS analyses of the overall composition, medium grey phase and the eutectic are shown in Table 4.2. The overall analysis was on the tie line as shown in Figure 4.2, implying that all major phases were accounted for.
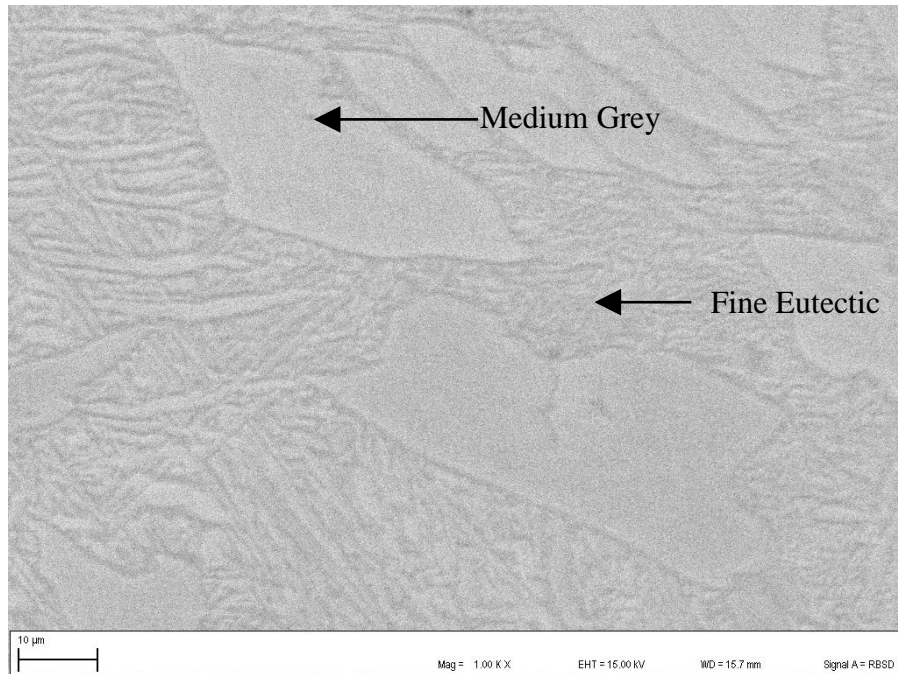
Figure 4.1: SEM-BSE image of Sample 1 (a) annealed at 200ºC showing a medium grey phase and a fine eutectic.

Table 4.2: EDS data for Sample 1 (a) annealed at 200ºC.

Phase Description	Composition (at.%)			Phase
	Cu	Zn	Al	
Overall	68.6±0.2	16.5±0.3	14.9±0.2	—
Medium Grey	71.8±0.4	16.7±0.5	11.5±0.1	(αCu)
Fine Eutectic	67.7±0.7	16.7±0.6	15.6±0.3	(αCu) + γ Cu_9Al_4
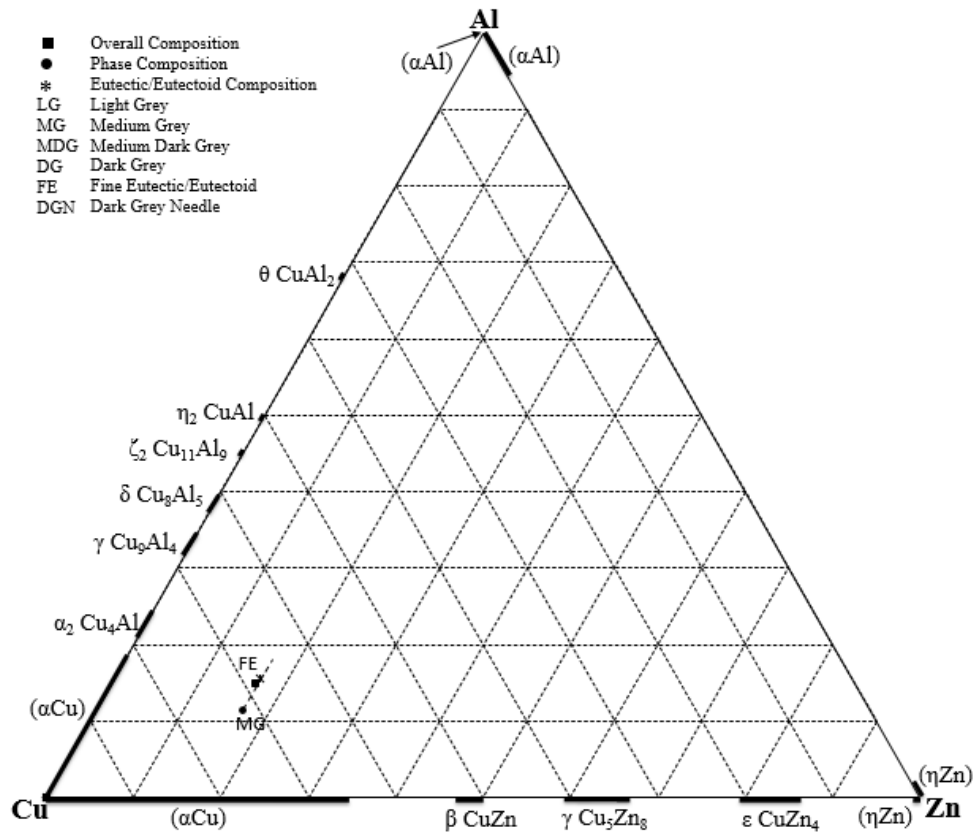
Figure 4.2: Composition plot of Sample 1 (a) annealed at 200°C (at.%).

4.2.1.2. Sample 1 (b), Average Composition $Al_{15.8}Cu_{79.1}Zn_{5.1}$ (at.%)

The SEM-BSE image of Sample 1 (b) in Figure 4.3 shows a medium grey matrix which was clearly dendritic before annealing, and a dispersed eutectic. Polishing did not remove all scratches from this sample. The dark grey phases in the eutectic were less than two microns across, therefore they could not be analysed separately and accurately. Area analyses of the eutectic were taken. The scatter in the EDS data in Table 4.3 was reasonably low. Figure 4.4 is a plot of this data on a ternary grid. The dark spots in the image are oxides, from the oxygen peaks in the overall analysis spectrum in Figure 4.5.
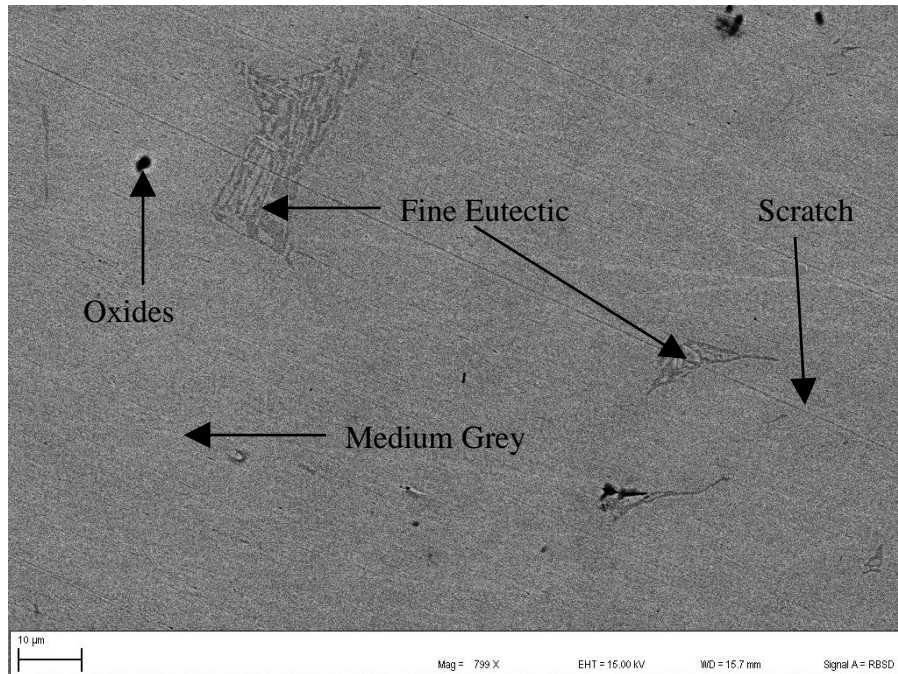
Figure 4.3: SEM-BSE image of Sample 1 (b) annealed at 200ºC showing a medium grey matrix and a dispersed fine eutectic.

Table 4.3: EDS data for Sample 1 (b) annealed at 200ºC.

Phase Description	Composition (at.%)			Phase
	Cu	Zn	Al	
Overall	79.1±0.2	5.1±0.3	15.8±0.2	—
Medium Grey	79.1±0.2	5.4±0.1	15.5±0.2	(αCu)
Fine Eutectic	72.8±0.8	4.5±0.2	22.7±0.9	(αCu) + γ Cu$_9$Al$_4$
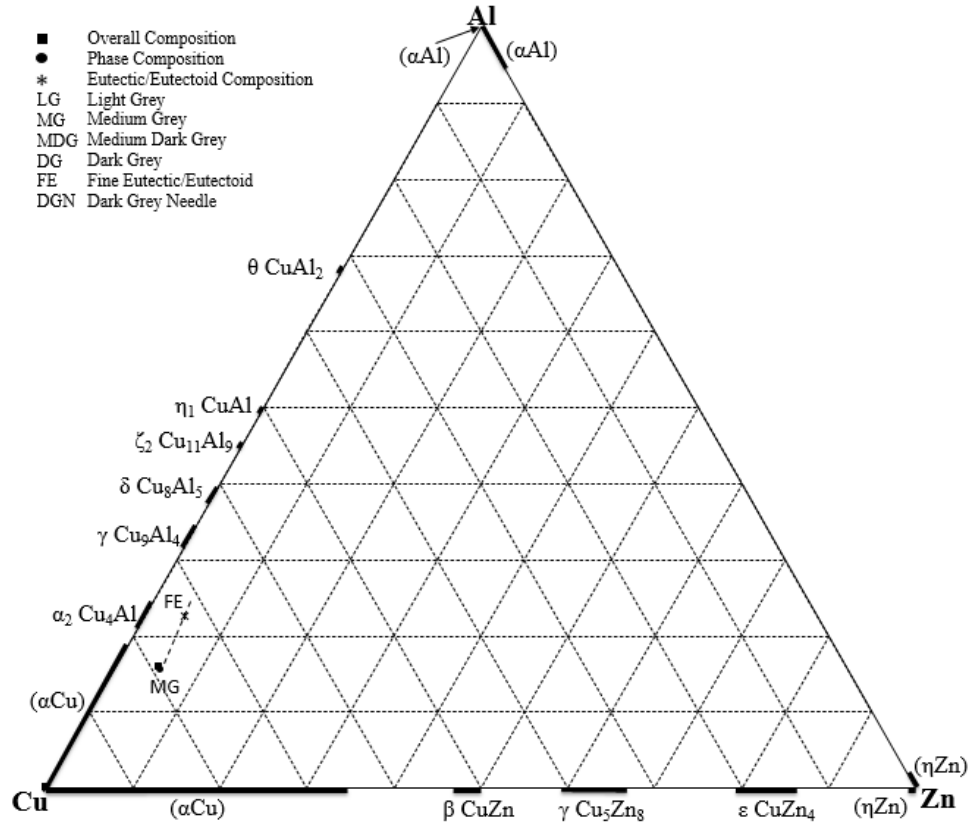
Figure 4.4: Composition plot of Sample 1 (b) annealed at 200ºC.
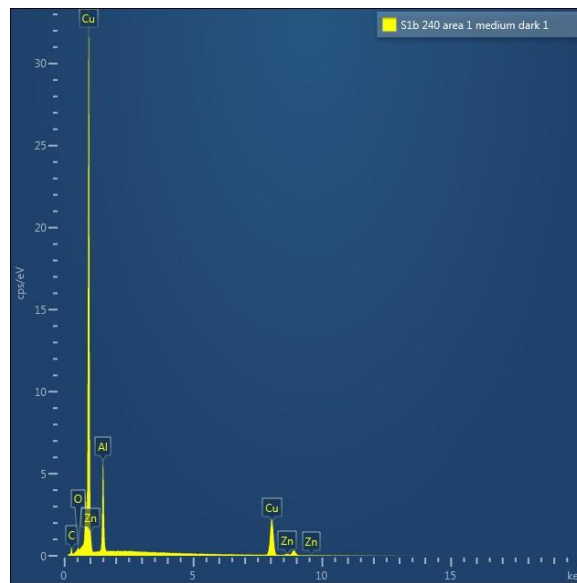
Figure 4.5: EDS spectrum of Sample 1 (b) showing oxygen and carbon peaks in the analysis of the phase with the medium dark contrast.

4.2.1.3. Sample 2 (a), Average Composition $Al_{27.8}Cu_{55.6}Zn_{16.6}$ (at.%)

There was poor contrast between the phases of Sample 2 (a) in the SEM-BSE image as shown in Figure 4.6. Nevertheless, two different phases were identified: a medium grey matrix and a dark grey precipitate. The scatter in the EDS data of the dark grey precipitates in Table 4.4 was comparatively higher than in the data of the medium grey matrix. The plots of the average compositions of the dark grey precipitates and medium grey matrix are shown in Figure 4.7. The dark spots in Figure 4.6 are carbon and oxide inclusions confirmed by the oxygen and carbon peaks in the EDS spectrum in Figure 4.8. The carbon and oxygen contaminations most likely occurred during casting.
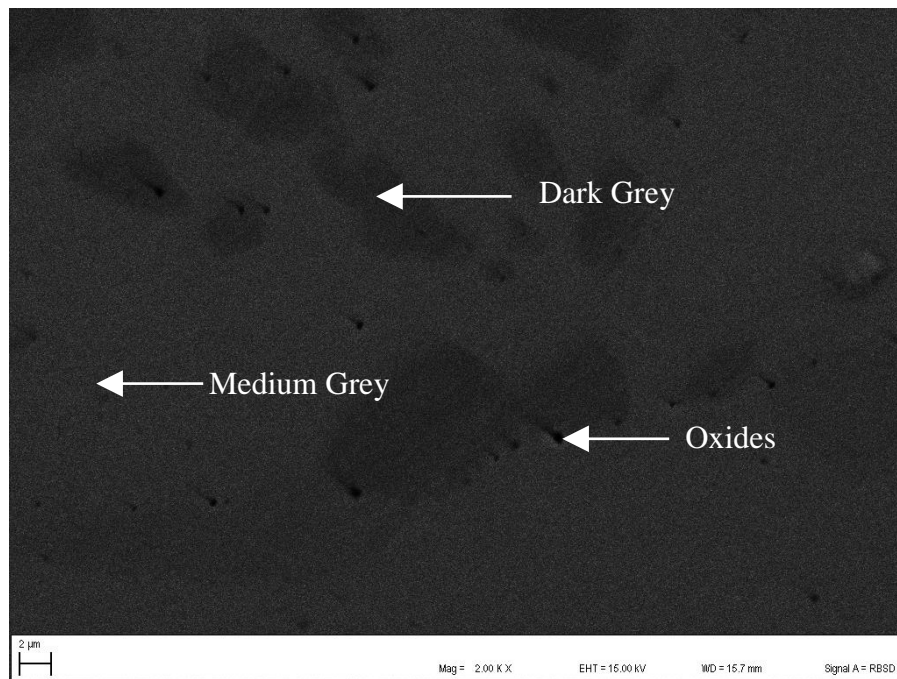
Figure 4.6: SEM-BSE image of Sample 2 (a) annealed at 200ºC showing a medium grey matrix and a dark grey precipitate.

43

Table 4.4: EDS data for Sample 2 (a) annealed at 200ºC.

Phase Description	Composition (at.%)			Phase
	Cu	Zn	Al	
Overall	55.6±0.2	16.6±0.3	27.8±0.3	—
Medium Grey	58.2±0.1	13.3±0.1	28.5±0.1	γ Cu_9Al_4
Dark Grey	48.4±0.6	26.8±1.0	24.8±0.4	τ $Cu_5Zn_2Al_3$
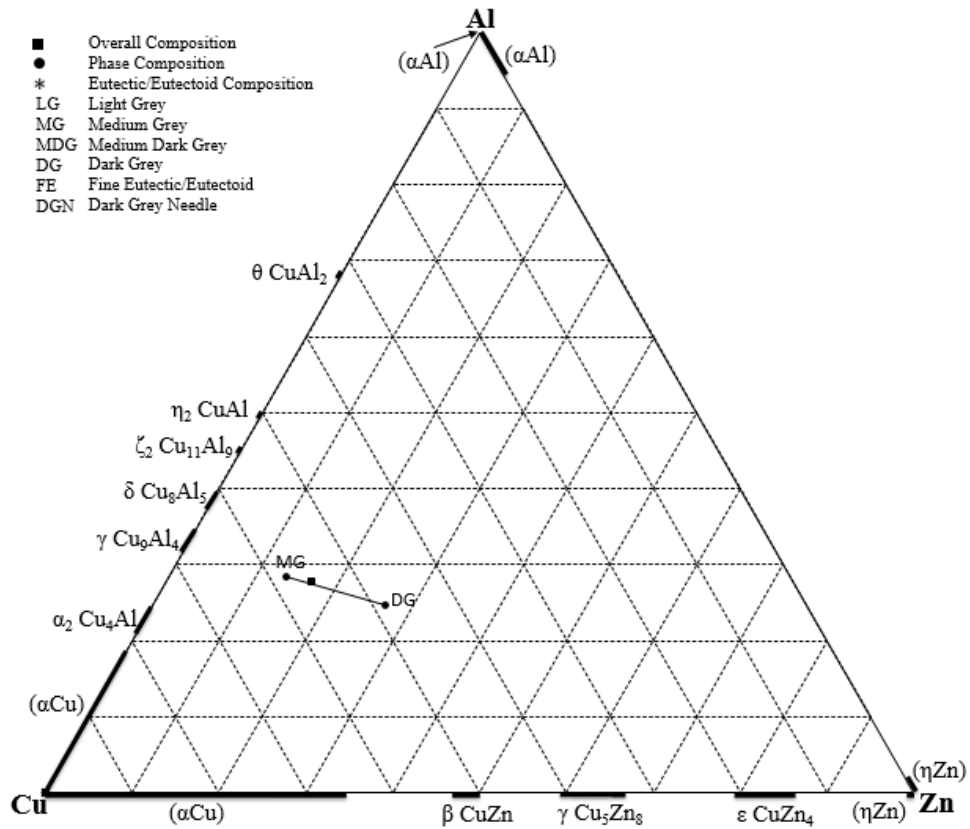
Figure 4.7: Composition plot of Sample 2 (a) annealed at 200ºC.
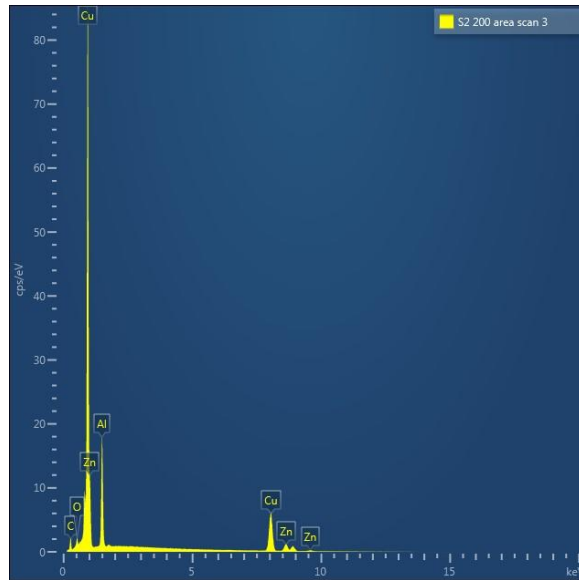
Figure 4.8: EDS spectrum of an area scan of Sample 2 (a) showing oxygen and carbon peaks.

4.2.1.4. Sample 2 (b), Average Composition Al$_{18.6}$Cu$_{75.3}$Zn$_{6.1}$ (at.%)

Sample 2 (b) showed very little contrast under the Leo 1525 Field Emission Gun SEM. Examination of the sample under a Crossbeam 540 FIB-SEM revealed a medium grey phase in a light grey matrix as shown in Figure 4.9. Metallographic preparation did not remove all the scratches. Their EDS data recorded in Table 4.5. Since the overall composition was on the tie line joining the two phases according to Figure 4.10, all the major phases present were analysed. The dark spot are oxides confirmed by the oxygen peaks in Figure 4.11.
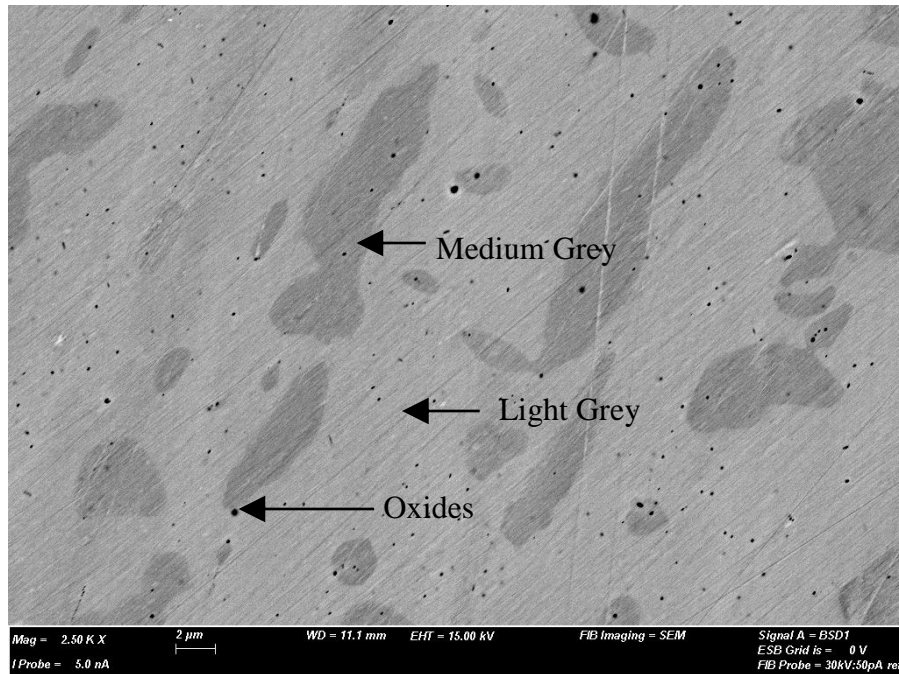
Figure 4.9: SEM-BSE image of Sample 2 (b) annealed at 200ºC showing a medium grey phase in a light grey matrix.

Table 4.5: EDS data for Sample 2 (b) annealed at 200ºC.

Phase Description	Composition (at.%)			Phase
	Cu	Zn	Al	
Overall	75.3±0.3	6.1±0.4	18.6±0.2	—
Light Grey	72.8±0.4	6.3±0.2	20.9±0.5	γ Cu_9Al_4
Medium Grey	77.5±0.3	6.1±0.2	16.4±0.2	(αCu)
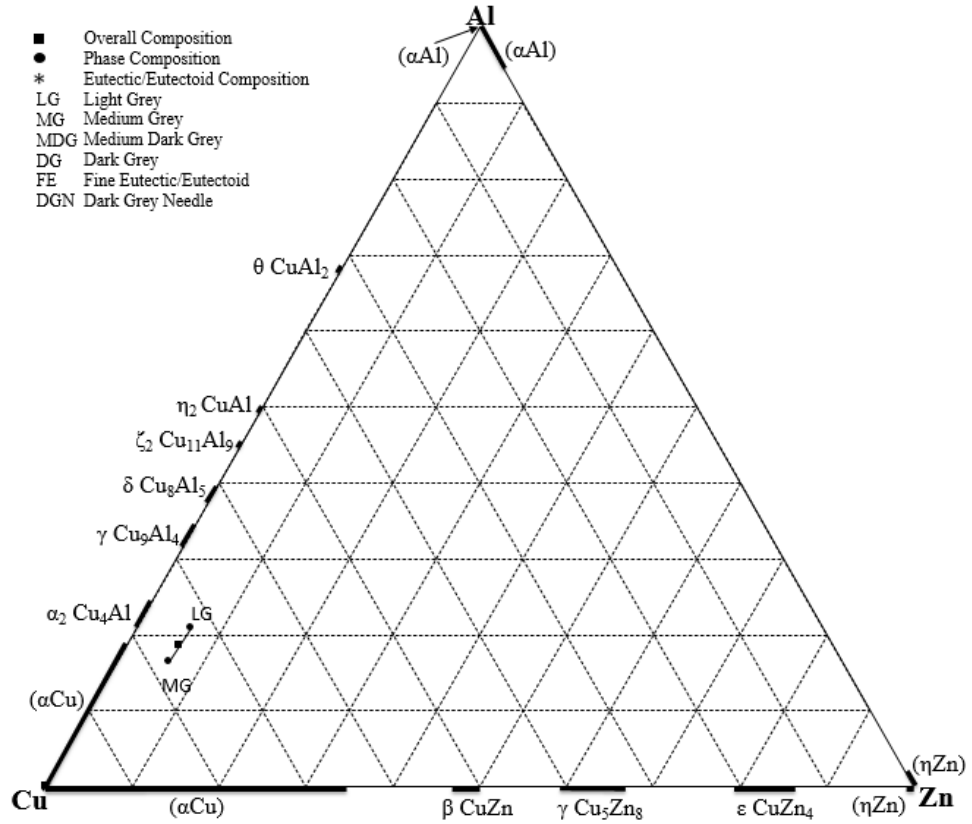
Figure 4.10: Composition plot of Sample 2 (b) annealed at 200ºC.
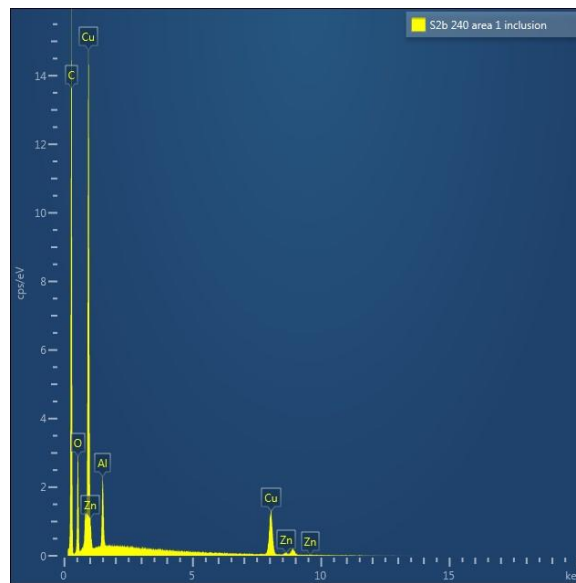
Figure 4.11: EDS spectrum of an inclusion in Sample 2 (b) showing high oxygen and carbon peaks.

47

4.2.1.5. Sample 3, Average Composition $Al_{14.3}Cu_{42.2}Zn_{43.5}$ (at.%)

The SEM-BSE image of Sample 3 in Figure 4.12 shows medium dark grey and dark grey phases in a light grey matrix. The scatter for all phases in Table 4.6 was reasonably low since they were all large. Sample 3 may not have been completely homogeneous since the plot of the overall composition lay on a tie line rather than within the triangle in Figure 4.13.
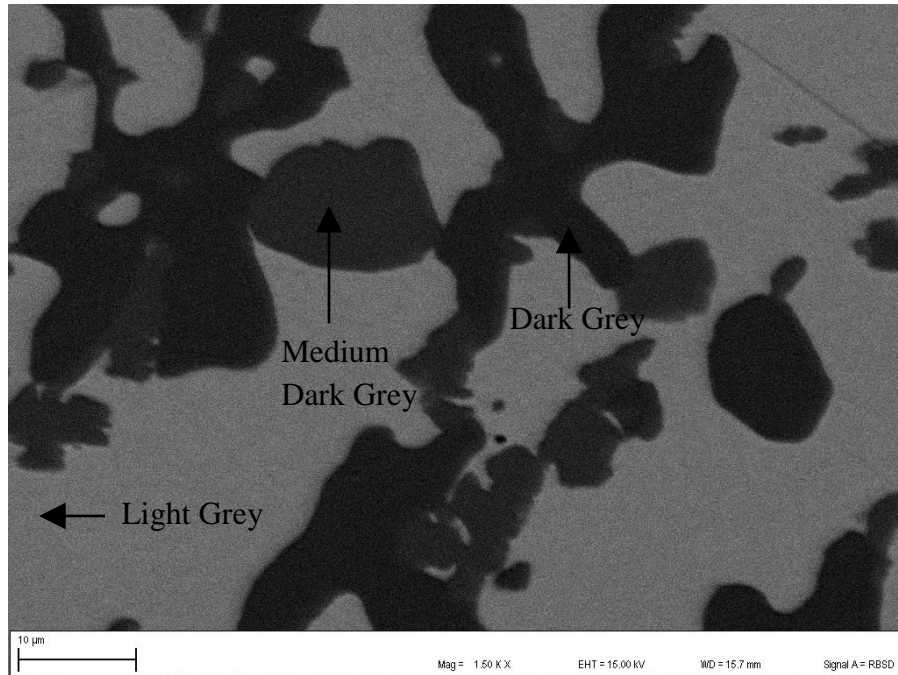
Figure 4.12: SEM-BSE image of Sample 3 annealed at 200ºC showing medium dark grey and dark grey phases in a light grey matrix.

Table 4.6: EDS data for Sample 3 annealed at 200ºC.

Phase Description	Composition (at.%)			Phase
	Cu	Zn	Al	
Overall	42.2±0.3	43.5±0.5	14.3±0.3	—
Light Grey	37.4±0.1	56.9±0.2	5.7±0.2	γ Cu_5Zn_8
Dark Grey	48.0±0.1	28.4±0.1	23.6±0.1	τ $Cu_5Zn_2Al_3$
Medium Dark Grey	57.2±0.4	16.0±0.9	26.8±0.6	γ Cu_9Al_4
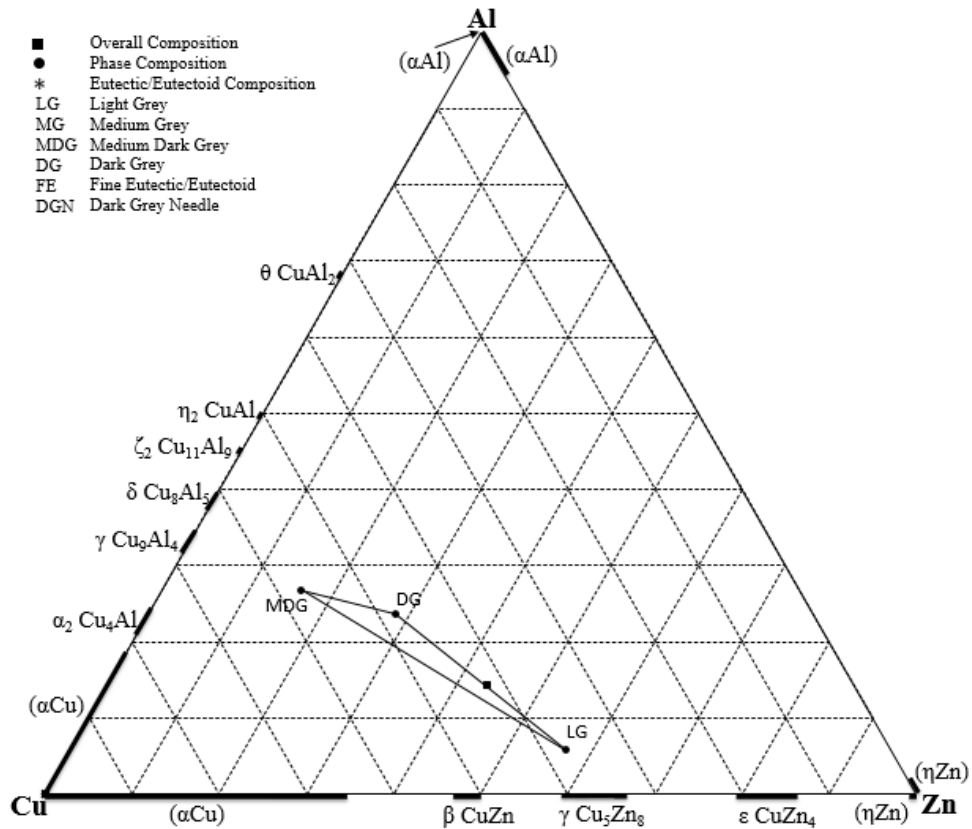
Figure 4.13: Composition plot of Sample 3 annealed at 200ºC.

4.2.1.6. Sample 5, Average Composition Al$_{13}$Cu$_{36.9}$Zn$_{50.1}$ (at.%)

The SEM-BSE image of Sample 5 in Figure 4.14 shows two phases (light grey and dark grey) and a fine eutectic. The dark grey phases were barely two microns across; therefore their analyses could have been affected by the surrounding phases. This is indicated by the higher scatter in their EDS data in Table 4.7. In Figure 4.15, the overall analysis lies within the triangle formed by the analyses of the three phases. Hence, all major phases of the sample were identified.
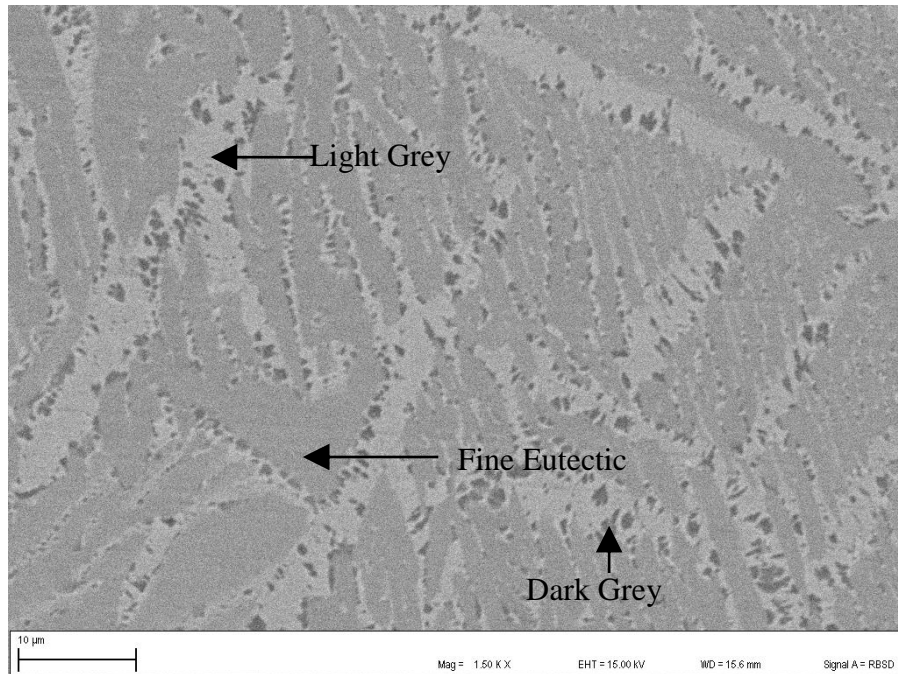
Figure 4.14: SEM-BSE image of Sample 5 annealed at 200ºC showing light grey and dark grey phases and a fine eutectic.

Table 4.7: EDS data for Sample 5 annealed at 200ºC.

Phase Description	Composition (at.%)			Phase
	Cu	Zn	Al	
Overall	36.9±0.2	50.1±0.1	13.0±0.1	—
Light Grey	40.9±0.3	48.8±0.5	10.3±0.3	γ Cu_5Zn_8
Fine Eutectic	35.1±0.2	51.8±0.3	13.1±0.3	ε $CuZn_4$ + γ Cu_5Zn_8
Dark Grey	45.3±0.6	32.7±1.0	22.0±0.5	τ $Cu_5Zn_2Al_3$

Figure 4.15: Composition plot of Sample 5 annealed at 200ºC.

4.2.1.7. Sample 7, Average Composition Al$_{41.9}$Cu$_{42.2}$Zn$_{15.9}$ (at.%)

The SEM-BSE image of Sample 7 in Figure 4.16 shows a medium dark grey matrix with a light grey phase and a dark grey phase. Significant scatters were expected in the analyses of the light grey phase and the dark grey phase in the eutectoid which were small, but this was not reflected in their EDS data in Table 4.8. On the contrary, their standard deviations were lower than those of the matrix. All phases were identified because the overall composition was within the triangle formed by the plots of the three phases in Figure 4.17.
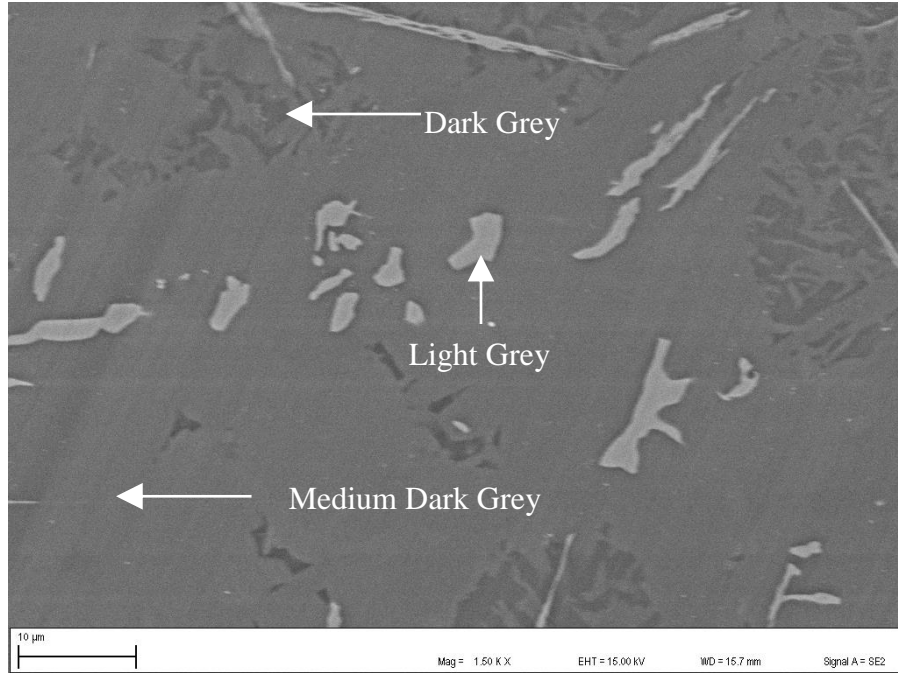
Figure 4.16: SEM BSE image of Sample 7 annealed at 200ºC showing a medium dark grey matrix with light grey and dark grey phases.

Table 4.8: EDS data for Sample 7 annealed at 200ºC.

Phase Description	Composition (at.%)			Phase
	Cu	Zn	Al	
Overall	42.2±0.6	15.9±0.3	41.9±0.4	—
Light Grey	21.1±0.2	76.0±0.3	2.9±0.2	ε $CuZn_4$
Medium Dark Grey	45.3±0.1	11.2±0.1	43.5±0.1	η_2 CuAl
Dark Grey	40.5±0.2	13.2±0.4	46.3±0.3	τ Cu_3ZnAl_4
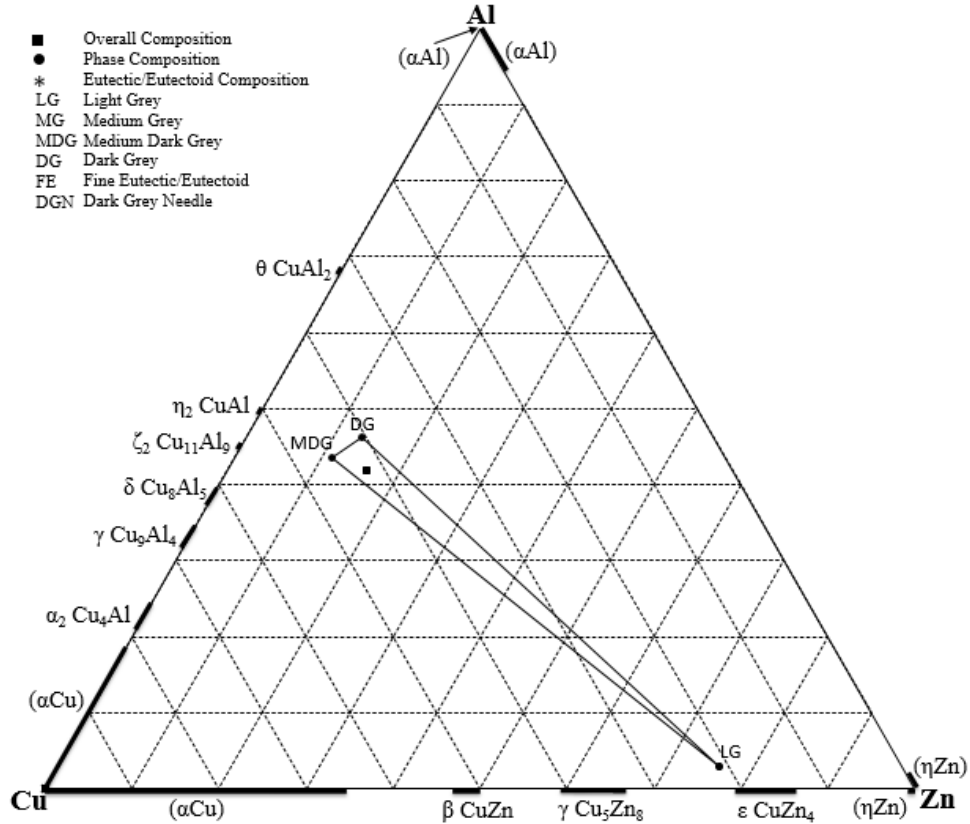
Figure 4.17: Composition plot of Sample 7 annealed at 200ºC.

4.2.1.8. Sample 8, Average Composition Al$_{25.8}$Cu$_{38.9}$Zn$_{35.3}$ (at.%)

Sample 8 had grain boundary porosity as illustrated by the SEM-BSE image in Figure 4.18. Its high magnification SEM-BSE image in Figure 4.19 looks like a eutectic of medium grey, dark grey and light grey phases, with occasional light grey precipitates in the medium grey and the dark grey phases. Their EDS data is shown in Table 4.9. The overall composition showed higher scatter in Table 4.9 and its plot in Figure 4.20 fell slightly outside the triangle bounded by the three phases. This was attributed to the grain boundary porosity observed in Figure 4.18 which occurred on solidification across the sample making homogenisation difficult. Figure 4.18 also shows that the light grey phase solidified last along the grain boundaries.

53
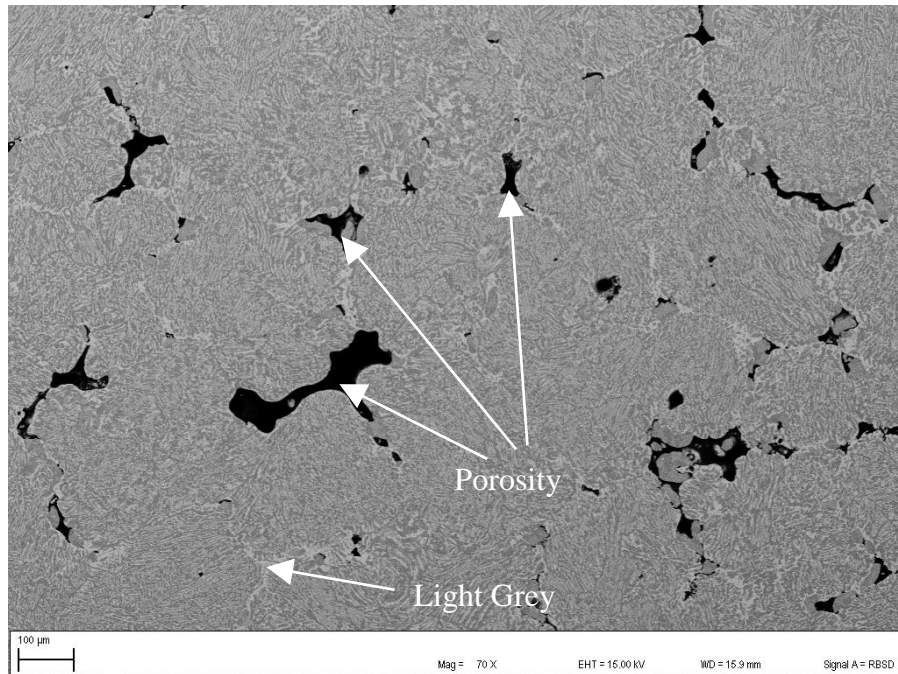
Figure 4.18: SEM-BSE image of Sample 8 annealed at 200ºC showing grain boundary porosity at low magnification.

Table 4.9: EDS data for Sample 8 annealed at 200ºC.

Phase Description	Composition (at.%)			Phase
	Cu	Zn	Al	
Overall	38.9±0.3	35.3±0.8	25.8±0.5	—
Light Grey	24.7±0.2	71.4±0.2	3.9±0.2	ε CuZn$_4$
Medium Grey	49.0±0.3	13.3±0.4	37.7±0.3	ζ_2 Cu$_{11}$Al$_9$
Dark Grey	47.6±0.2	25.9±0.1	26.6±0.2	τ Cu$_5$Zn$_2$Al$_3$
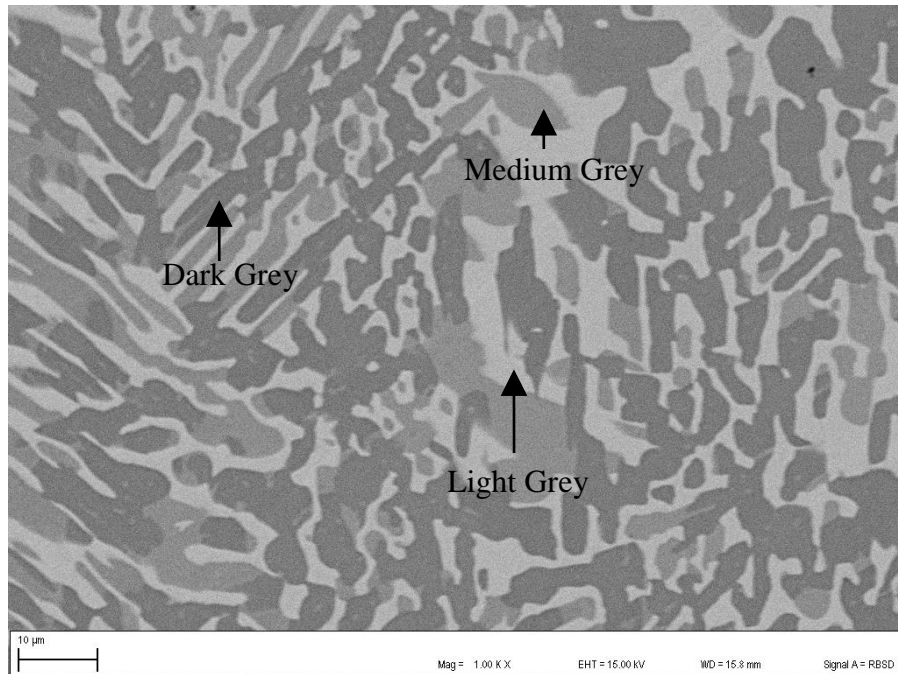
Figure 4.19: SEM-BSE image of Sample 8 annealed at 200ºC showing medium grey and dark grey phases in a light grey matrix.
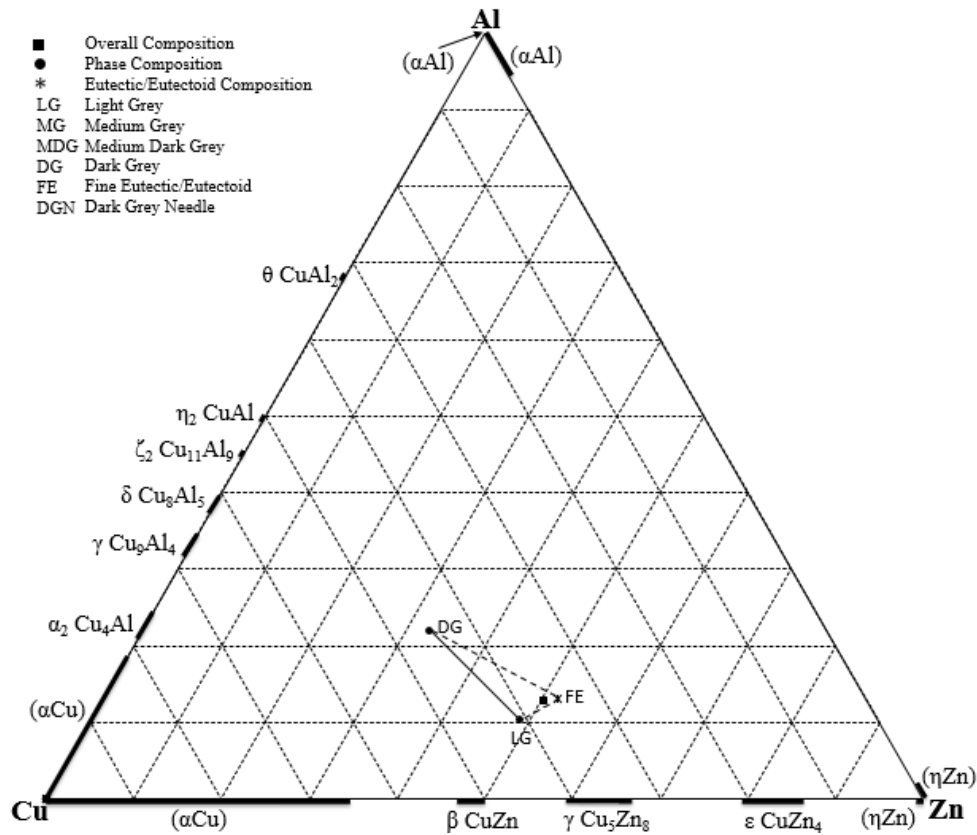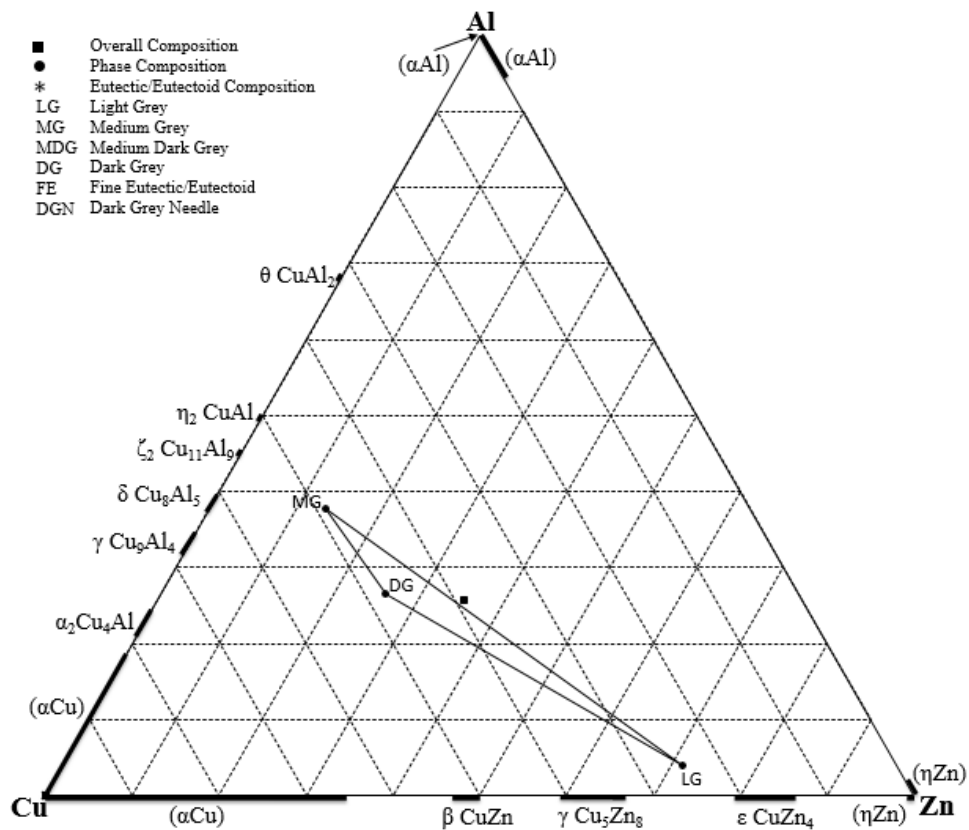

Figure 4.20: Composition plot of Sample 8 annealed at 200ºC.

4.2.1.9. Sample 9, Average Composition Al$_{21}$Cu$_{22.3}$Zn$_{56.7}$ (at.%)

The SEM-BSE image of Sample 9 at low magnification in Figure 4.21 shows that the sample had grain boundary porosity. Phases were more distinct in the SEM-BSE image in Figure 4.22 taken at higher magnification which revealed dark grey phases and dark grey needle precipitates in a light grey matrix. The dark grey needle precipitates were separately analysed to investigate whether they were different phases from the dark grey phases. Even though the EDS data of these precipitates in Table 4.10 implied that they may indeed be a different phase, the close proximity of their data point to that of the dark grey phase in Figure 4.23 suggested otherwise. They are most likely the same phase as the dark grey phase but at different orientations.

The grain boundary porosity in Figure 4.21 hampered homogenisation and could explain why the overall analysis lay outside the area bounded by the three phase analyses in Figure 4.23.
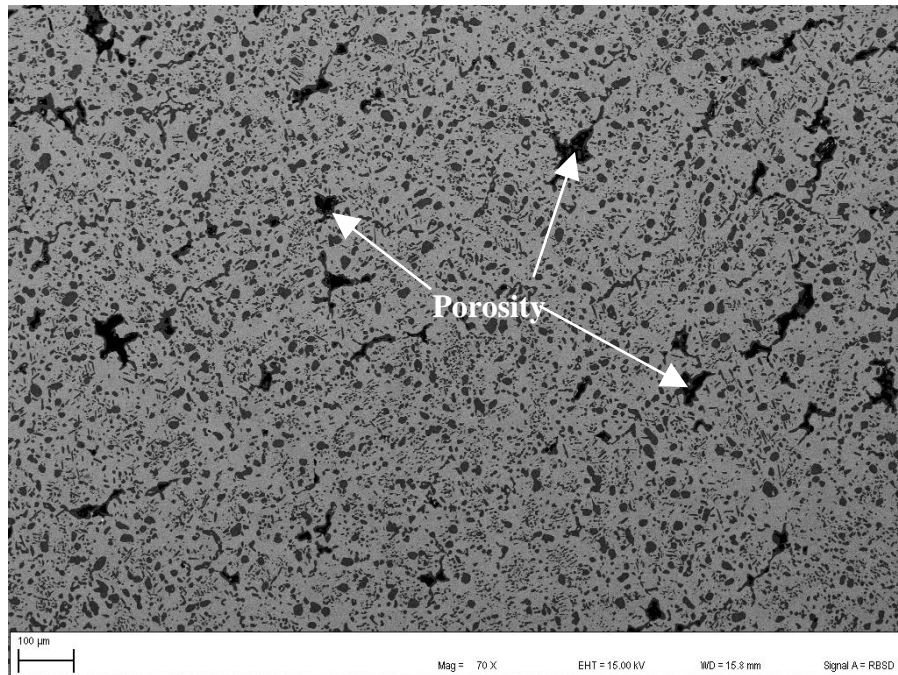
Figure 4.21: SEM-BSE image of Sample 9 annealed at 200ºC showing grain boundary porosity at low magnification.

56

Table 4.10: EDS data for Sample 9 annealed at 200ºC.

Phase Description	Composition (at.%)			Phase
	Cu	Zn	Al	
Overall	22.3±0.6	56.7±2.0	21.0±1.6	—
Light Grey	18.8±0.1	79.4±0.1	1.8±0.1	ε CuZn$_4$
Dark Grey	38.8±0.7	8.7±0.4	52.5±0.5	τ' Cu$_3$ZnAl$_4$
Dark Grey Needle	38.6±0.1	7.4±0.2	54.0±0.2	τ' Cu$_3$ZnAl$_4$

Figure 4.22: SEM-BSE image of Sample 9 annealed at 200ºC showing dark grey and dark grey needle precipitates in a light grey matrix.
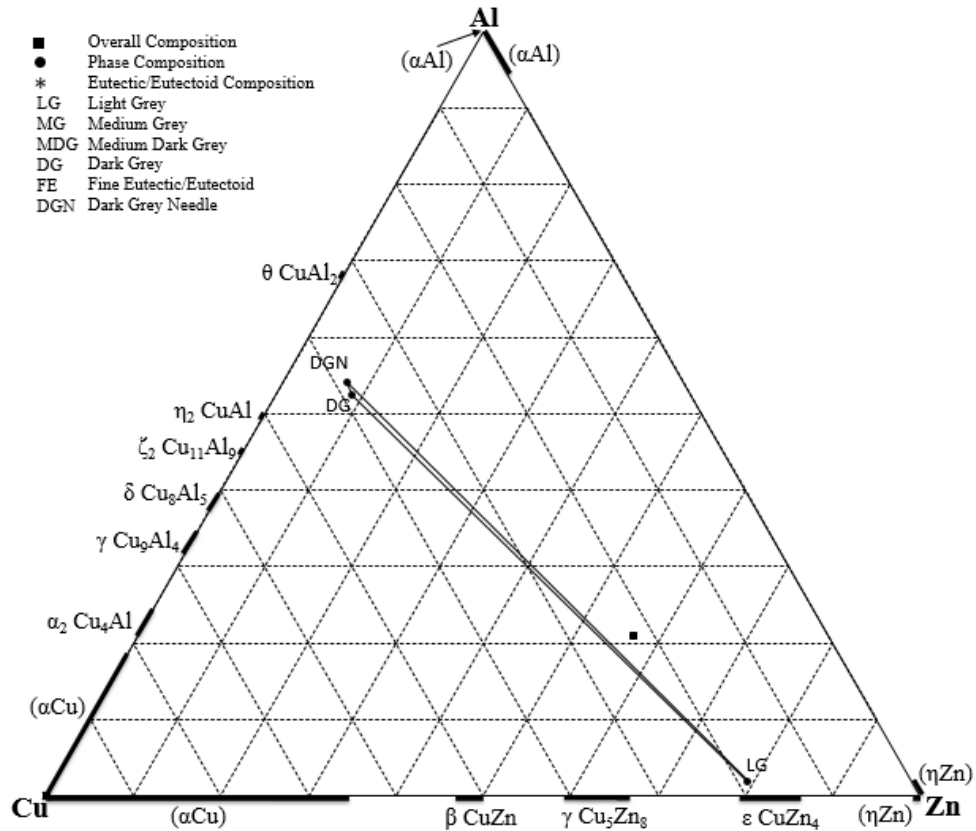
Figure 4.23: Composition plot of Sample 9 annealed at 200ºC.

4.2.1.10.   Sample 12, Average Composition Al$_{10.9}$Cu$_{17.4}$Zn$_{71.7}$ (at.%)

There were high levels of grain boundary porosity in Sample 12 as shown in the SEM-BSE image at low magnification (Figure 4.24). Dark grey phases and dark grey needle precipitates were observed in a light grey matrix at high magnification as shown in the SEM-BSE image in Figure 4.25. Both the dark grey and the dark grey needle precipitates were too small to be analysed accurately. This was confirmed by their higher standard deviations in their EDS data in Table 4.11. Figure 4.26 implies that the dark grey phases and the dark grey needle precipitates may be the same phase that was affected differently by the light grey matrix since both of them are on the tie line. The significant departure of the data point of the overall composition from the

tie line in Figure 4.26 can be explained by either the grain boundary porosity in Figure 4.24 which may have hindered homogenisation, or by the presence of an extra phase that may not have been analysed. The dark patches in Figure 4.25 are carbon and oxides confirmed by the high oxygen and carbon peaks in their EDS spectrum in Figure 2.27.
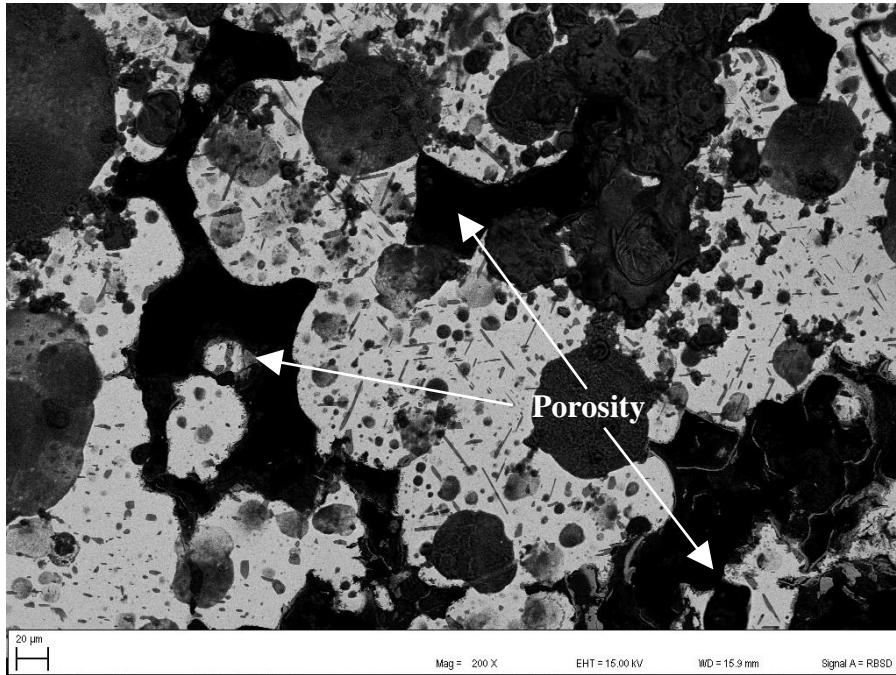
Figure 4.24: SEM-BSE image Sample 12 annealed at 200ºC showing porosity.

Table 4.11: EDS data for Sample 12 annealed at 200ºC.

Phase Description	Composition (at.%)			Phase
	Cu	Zn	Al	
Overall	17.4±1.5	71.7±1.6	10.9±1.6	—
Light Grey	20.4±0.2	77.1±0.2	2.5±0.1	ε CuZn$_4$
Dark Grey	38.4±0.8	9.1±1.2	52.5±0.7	τ' Cu$_3$ZnAl$_4$
Dark Grey Needle	37.3±1.6	13.5±2.2	49.2±0.7	τ' Cu$_3$ZnAl$_4$
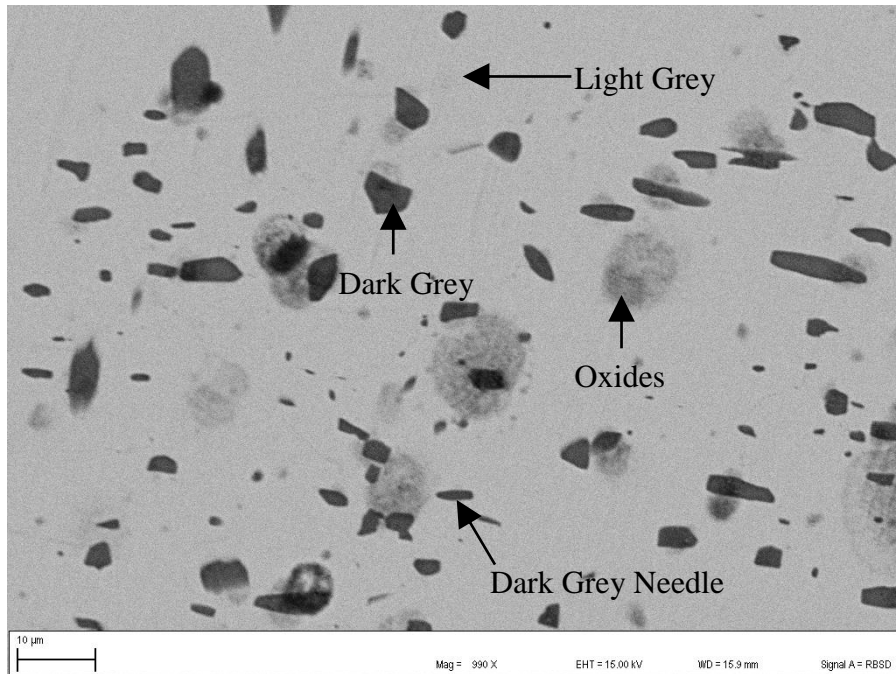
Figure 4.25: SEM-BSE image of Sample 12 annealed at 200ºC showing dark grey and dark grey needle precipitates in a light grey matrix.
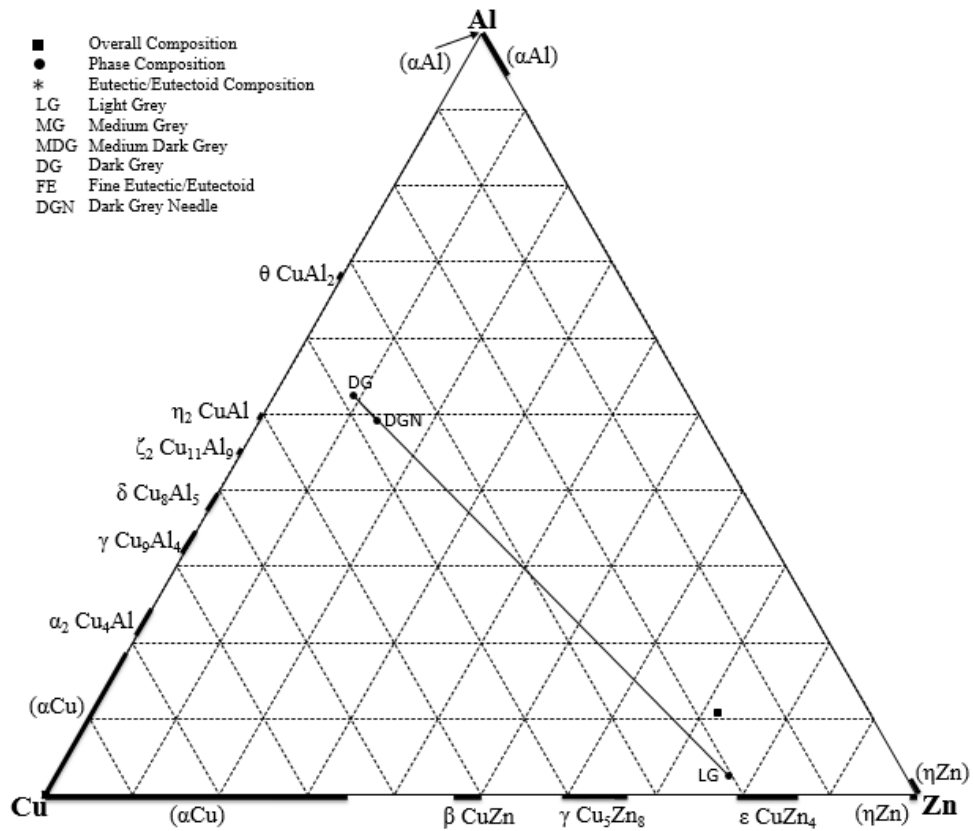
Figure 4.26: Composition plot of Sample 12 annealed at 200ºC.
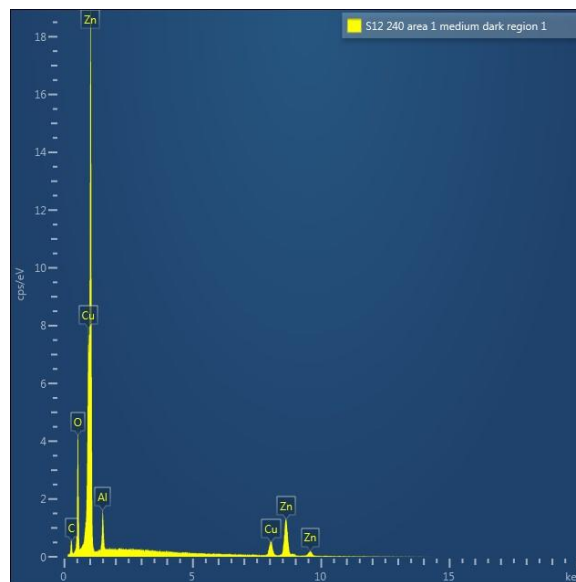
Figure 4.27: EDS spectrum of Sample 12 showing high oxygen and carbon peaks in the analysis of a dark patch.

61

4.2.2. Alloys Heat-Treated at 240ºC

4.2.2.1. Sample 1 (a), Average Composition Al$_{14.7}$Cu$_{68.6}$Zn$_{16.7}$ (at.%)

Figure 4.28 is an SEM-BSE image of Sample 1(a) a showing medium grey phase and a fine eutectic. Since the dark grey phase in the eutectic was small and could not be analysed independently, the eutectic was analysed as areas. The EDS data is in Table 4.12. A plot of the EDS data in Table 4.12 is shown in Figure 4.29.

The surface stain in Figure 4.28 (probably introduced during sample handling) was avoided during EDS analysis to avoid spurious data. The dark spots and patches on the sample had a high oxygen peak as shown in Figure 4.30, meaning that they were oxides of at least one of the constituent elements.
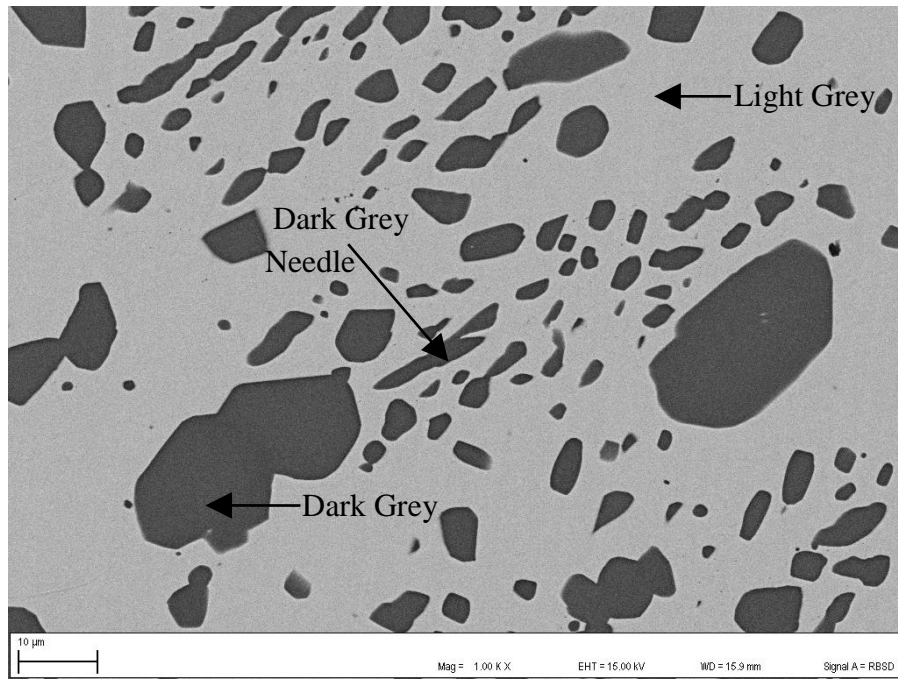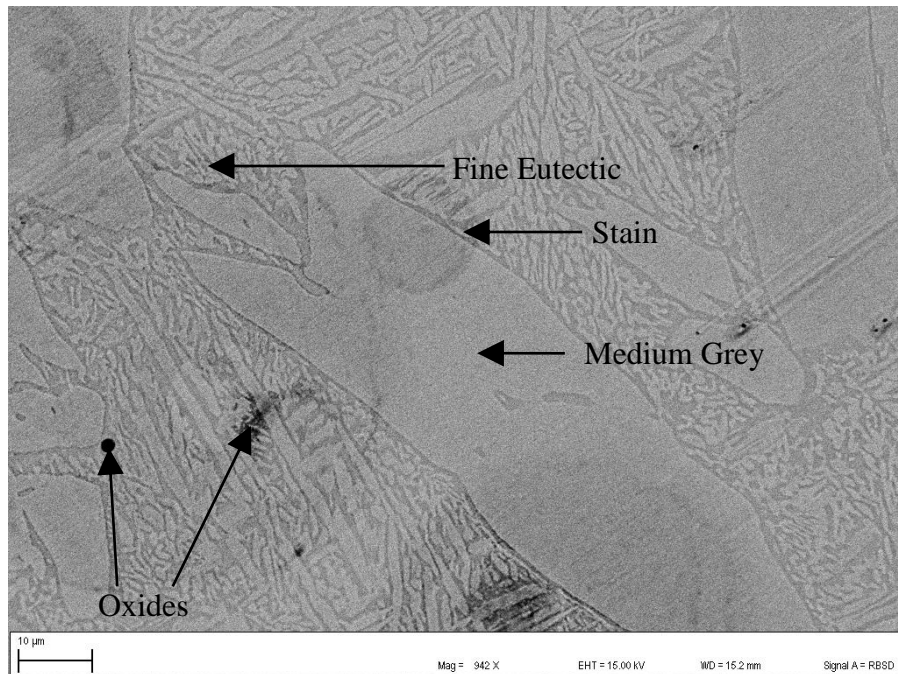

Figure 4.28: SEM-BSE image of Sample 1 (a) annealed at 240ºC showing a medium grey phase and a fine eutectic.

Table 4.12: EDS data for Sample 1 (a) annealed at 240ºC.

Phase Description	Composition (at.%)			Phase
	Cu	Zn	Al	
Overall	68.6±0.2	16.7±0.1	14.7±0.1	—
Medium Grey	71.7±0.3	16.8±0.4	11.5±0.2	(αCu)
Fine Eutectic	67.5±0.7	17.0±0.3	15.5±0.5	(αCu) + γ Cu₉Al₄

Figure 4.29: Composition plot of Sample 1 (a) annealed at 240ºC.
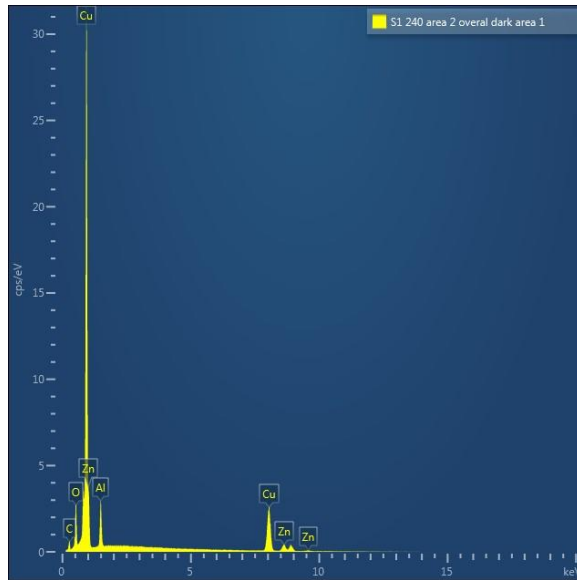
Figure 4.30: EDS spectrum of an dark area scan of Sample 1 (a) showing oxygen and carbon peaks.

4.2.2.2. Sample 1 (b), Average Composition $Al_{16}Cu_{78.9}Zn_{5.1}$ (at.%)

The SEM-BSE image of Sample 1 (b) in Figure 4.31 had poor phase contrast and the sample showed scratches from metallographic preparation. However, closer examination revealed a medium grey phase with medium dark grey areas along the boundaries. The EDS analyses and plot of these dark areas, as shown in Table 4.13 and Figure 4.32, indicated that they were not different phases. Their composition was very close to that of the medium grey phase. Therefore, it was deduced that this sample had a single, medium grey phase that was cored. The dark spots in Figure 4.31 are traces of carbon and oxides, indicated by the oxygen and carbon peaks in the EDS spectrum in Figure 4.33.

64
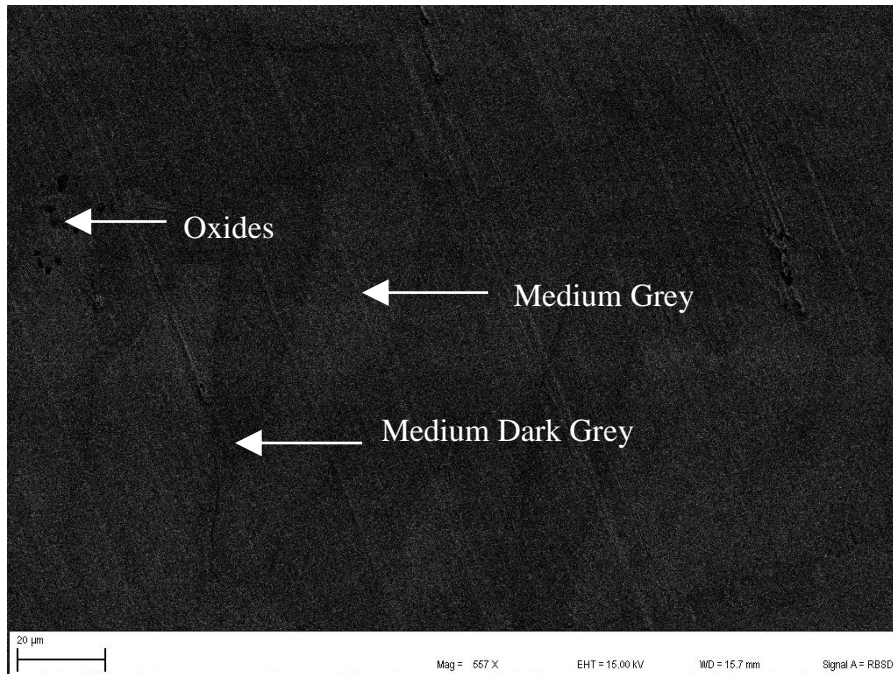
Figure 4.31: SEM-BSE image of Sample 1 (b) annealed at 240ºC showing a cored medium grey phase.

Table 4.13: EDS data for Sample 1 (b) annealed at 240ºC.

Phase Description	Composition (at.%)			Phase
	Cu	Zn	Al	
Overall	78.9±0.1	5.1±0.1	16.0±0.1	—
Medium Grey	79.8±0.3	5.1±0.2	15.1±0.3	(αCu)
Medium Dark Grey	79.1±0.2	5.1±0.2	15.8±0.2	(αCu)
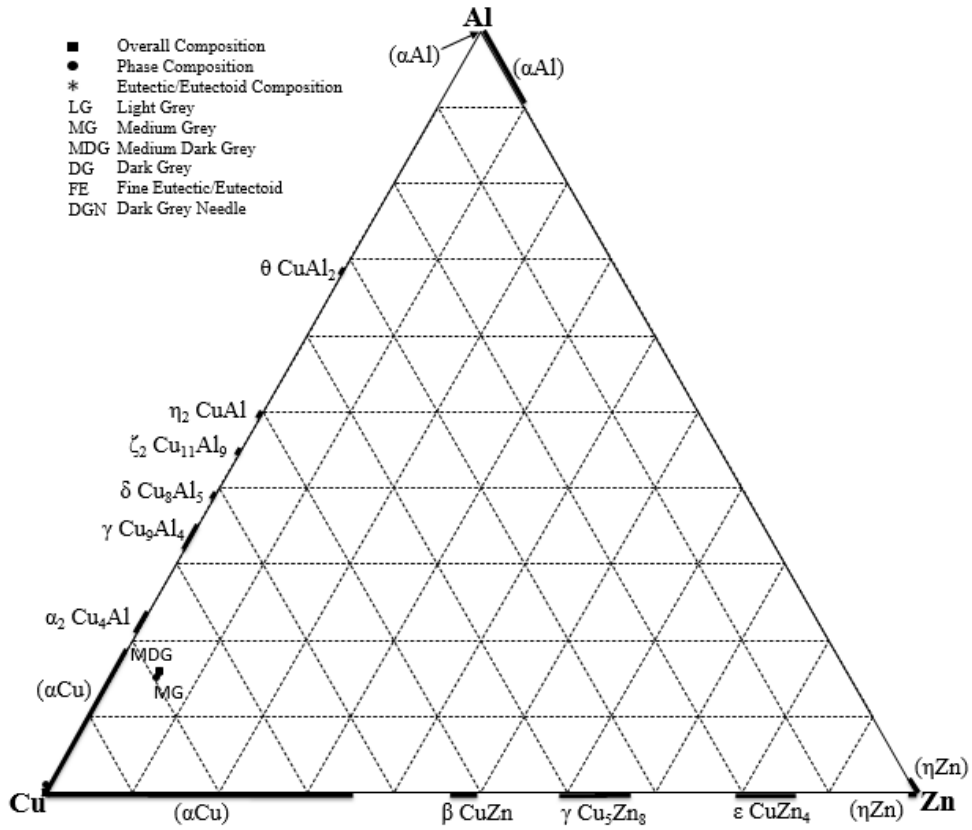
Figure 4.32: Composition plot of Sample 1 (b) annealed at 240ºC.
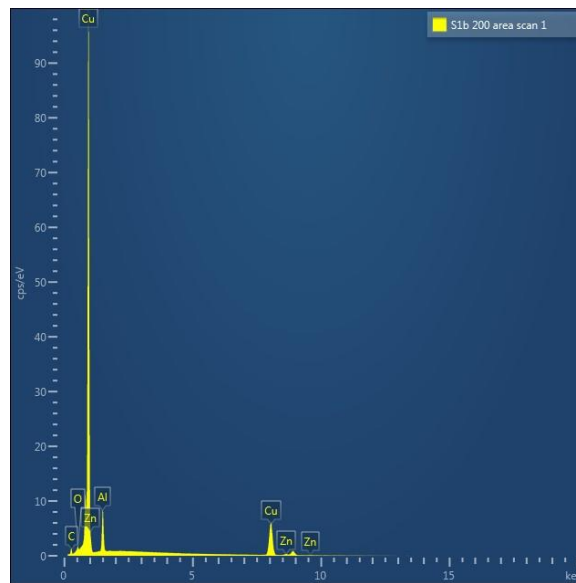
Figure 4.33: The EDS spectrum of an area scan of Sample 1 (b) showing oxygen and carbon peaks.

66

4.2.2.3. Sample 2 (a), Average Composition $Al_{28.1}Cu_{55}Zn_{16.9}$ (at.%)

There was poor contrast between the phases of Sample 2 (a) as shown in Figure 4.34 as well as scratches from sample preparation. Closer examination revealed a medium grey matrix and medium dark grey precipitates. Their EDS results are given in Table 4.14. Since the average overall composition of the sample was on the tie line connecting the two phases in the plot given in Figure 4.35, it is reasonable to conclude that all constituent phases of this samples were analysed. In addition to carbon and oxide inclusions, traces of Si were observed in the dark spot's spectrum in Figure 4.36. The silicon carbide lapping compound used during polishing was deduced to have been the source of the silicon.
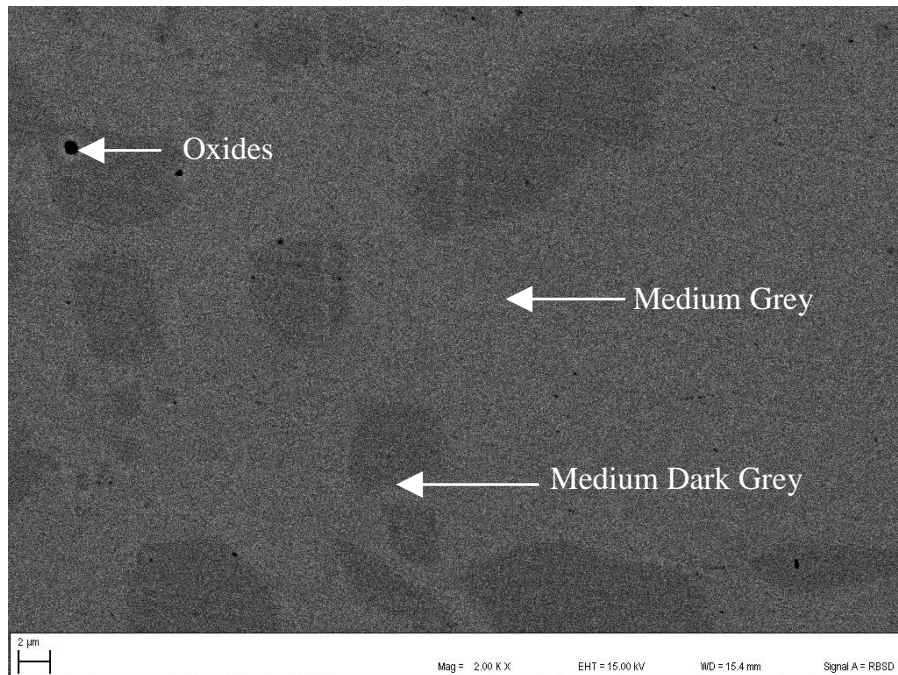
Figure 4.34: SEM-BSE image of Sample 2 (a) showing a medium grey matrix and medium dark grey precipitates.

Table 4.14: EDS data for Sample 2 (a) annealed at 240ºC.

Phase Description	Composition (at.%)			Phase
	Cu	Zn	Al	
Overall	55.0±0.4	16.9±0.5	28.1±0.2	—
Medium Grey	57.6±0.2	13.4±0.2	29.0±0.2	γ Cu$_9$Al$_4$
Medium Dark Grey	47.8±0.1	27.0±0.1	25.2±0.2	τ Cu$_5$Zn$_2$Al$_3$
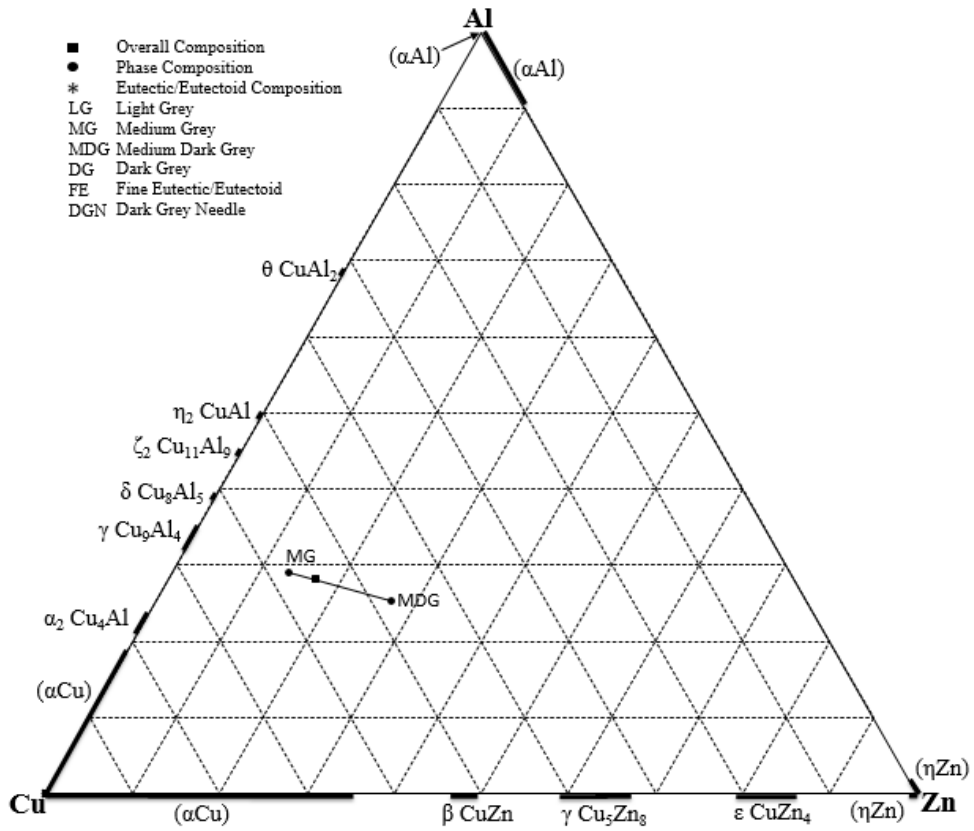
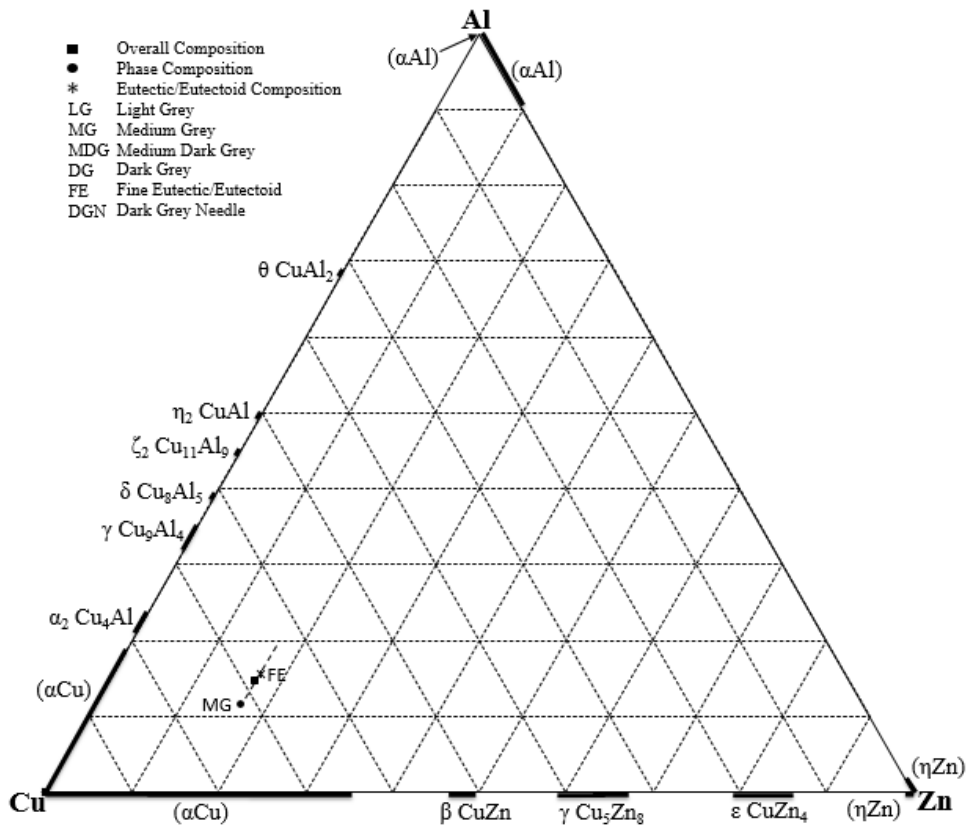*Figure 4.35: Composition plot of Sample 2 (a) annealed at 240ºC.*
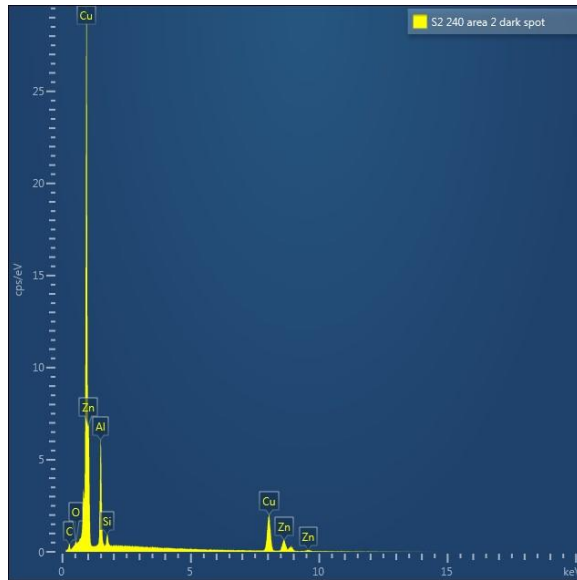
Figure 4.36: The EDS spectrum of an area scan of Sample 2 (a) showing oxygen, carbon and silicon peaks.

4.2.2.4. Sample 2 (b), Average Composition Al$_{19}$Cu$_{74.5}$Zn$_{6.5}$ (at.%)

The SEM-BSE image of Sample 2(b), in Figure 4.37, shows a medium grey phase, a dark grey phase, and a fine eutectic of the two phases. The dark grey phases appeared to be too narrow to be analysed accurately. However, their EDS data in Table 4.15 indicate that their analysis was not significantly affected by the dendrites. Area analyses of the eutectic were also taken. The data point of the overall analysis fell slightly outside the tie line as shown in Figure 4.38, but is within the expected scatter.

69
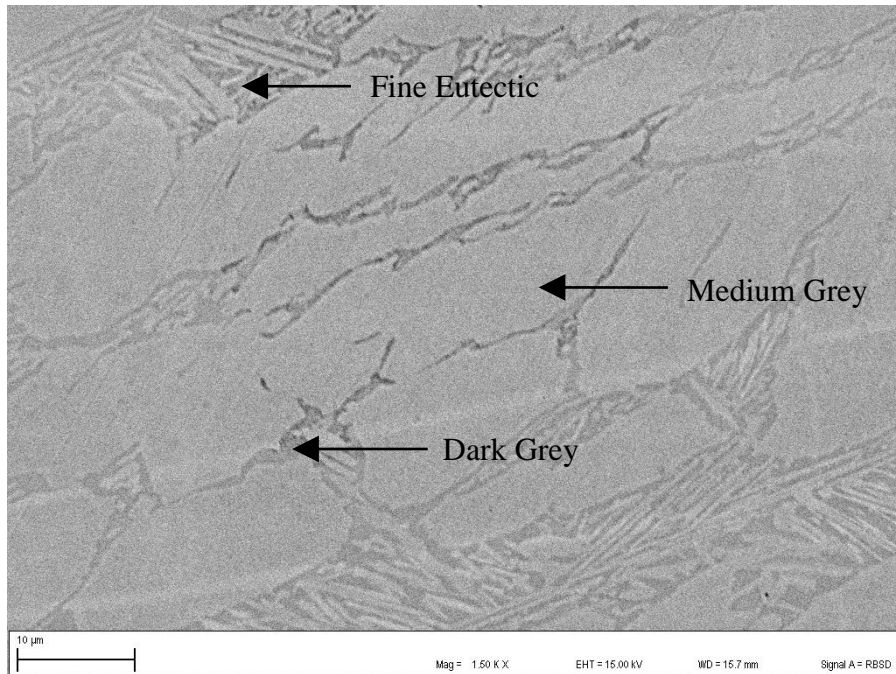
Figure 4.37: SEM-BSE image of Sample 2 (b) annealed at 240ºC showing a medium grey phase, a dark grey phase, and a fine eutectic.

Table 4.15: EDS data for Sample 2 (b) annealed at 200ºC.

Phase Description	Composition (at.%)			Phase
	Cu	Zn	Al	
Overall	74.5±0.4	6.5±0.2	19.0±0.3	—
Medium Grey	76.7±0.4	6.0±0.1	17.3±0.4	(αCu)
Dark Grey	68.7±0.6	5.5±0.3	25.8±0.7	γ Cu_9Al_4
Fine Eutectic	71.5±0.6	6.4±0.3	22.1±0.5	(αCu) + γ Cu_9Al_4
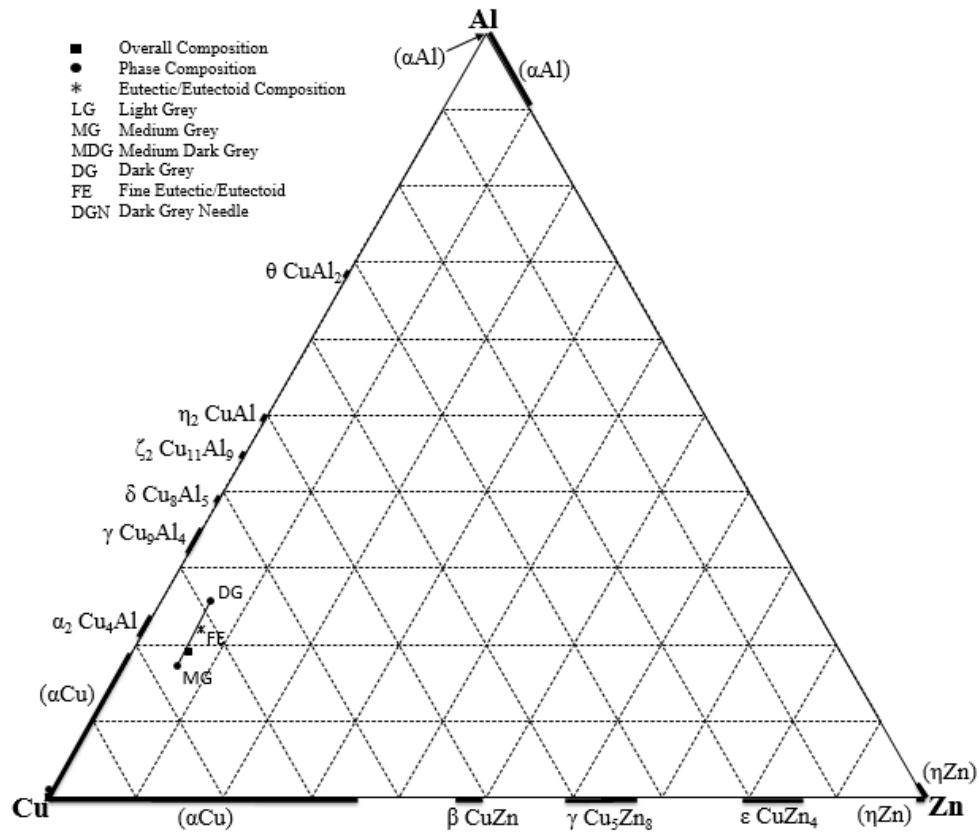
Figure 4.38: Composition plot of Sample 2 (b) annealed at 240ºC.

4.2.2.5. Sample 3, Average Composition Al$_{14.5}$Cu$_{42.9}$Zn$_{42.6}$ (at.%)

Sample 3 had medium grey and dark grey phases in a light grey matrix as shown in Figure 4.39. The EDS data in Table 4.16 shows that there was little scatter in the compositions of the three phases. The sample may not have reached complete homogeneity since the overall composition of the phase was on a tie line rather than inside the triangle as shown in the plot in Figure 4.40.
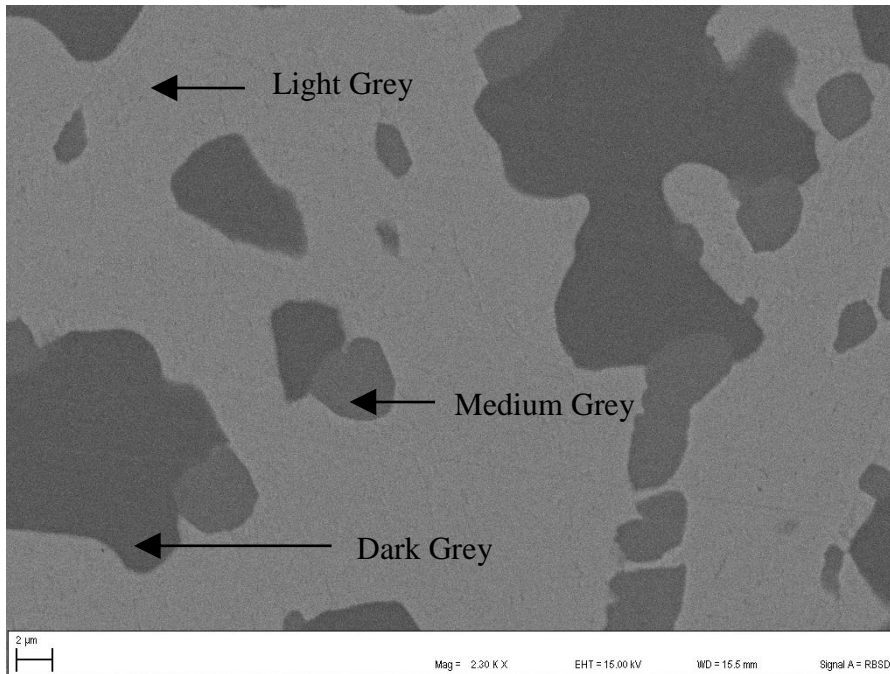
Figure 4.39: SEM-BSE image of Sample 3 annealed at 240ºC showing medium grey and dark grey phases in a light grey matrix.

Table 4.16: EDS data for Sample 3 annealed at 240ºC.

Phase Description	Composition (at.%)			Phase
	Cu	Zn	Al	
Overall	42.9±0.4	42.6±0.8	14.5±0.4	—
Light Grey	39.4±0.1	52.8±0.1	7.8±0.1	γ Cu_5Zn_8
Medium Grey	55.4±0.3	20.3±0.5	24.3±0.3	γ Cu_9Al_4
Dark Grey	48.3±0.1	28.5±0.1	23.2±0.2	τ $Cu_5Zn_2Al_3$
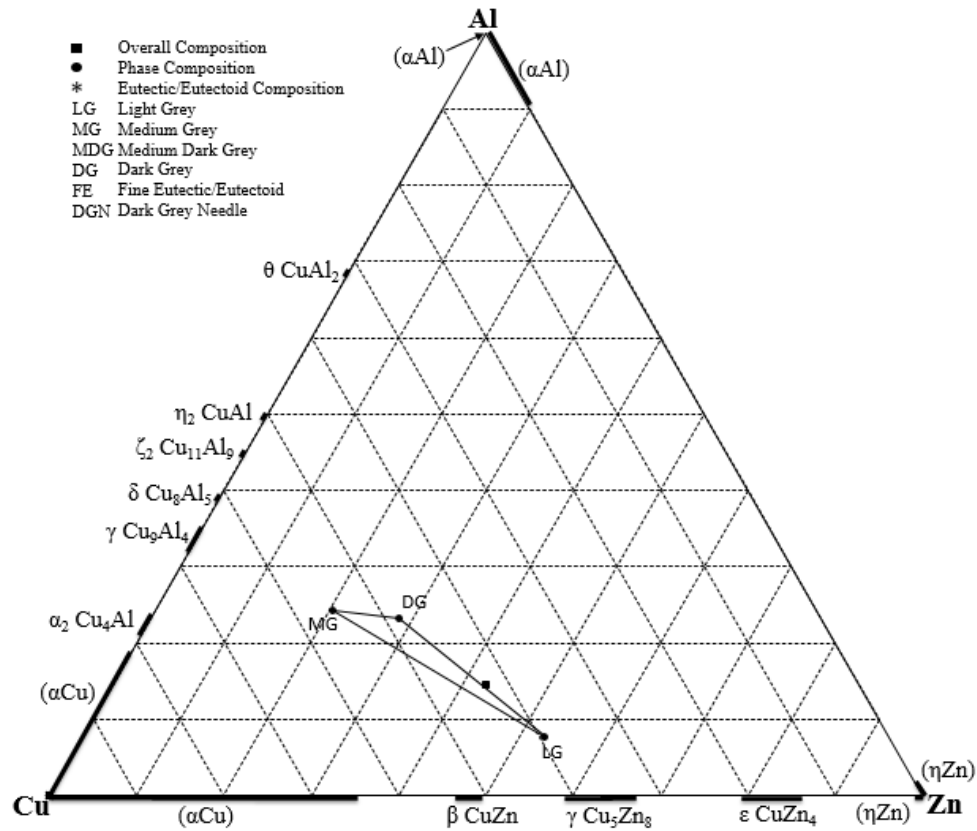
Figure 4.40: Composition plot of Sample 3 annealed at 240ºC.

4.2.2.6. Sample 5, Average Composition Al$_{13.2}$Cu$_{36.8}$Zn$_{50}$ (at.%)

The SEM-BSE image in Figure 4.41 shows a medium grey phase, a medium dark grey phase, a light grey phase and a fine eutectoid of the medium dark grey phase and the medium grey phase. The contrast of the medium grey and the light grey phases was very close but their different EDS data in Table 4.17 indicates that they are different phases. The standard deviation of the overall analysis was relatively high but still lay within the area bounded by the phase data points in Figure 4.42. The dark patches in Figure 4.41 are carbon and oxide inclusions indicated by the carbon and oxygen peaks in the area spectrum in Figure 4.43.
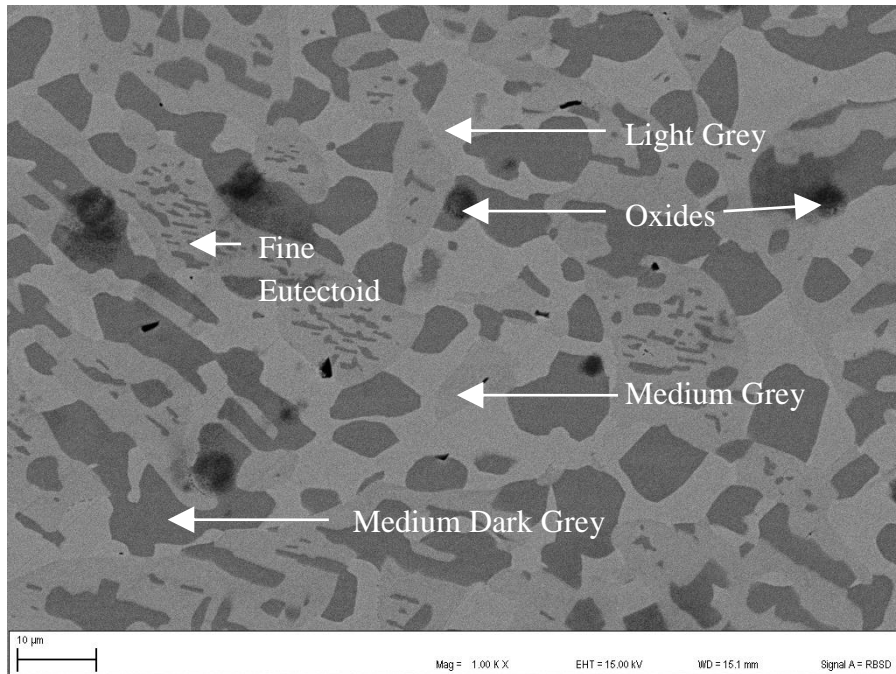
Figure 4.41: SEM-BSE image of Sample 5 annealed at 240ºC showing medium grey, medium dark grey and light grey phases, and a fine eutectoid.

Table 4.17: EDS data for Sample 5 annealed at 240ºC.

| Phase Description	Composition (at.%)			Phase
	Cu	Zn	Al	
Overall	36.8±0.9	50.0±1.4	13.2±0.6	—
Light Grey	37.1±0.2	56.8±0.4	6.1±0.4	γ Cu_5Zn_8
Fine Eutectoid	32.7±0.9	55.9±1.7	11.4±0.8	τ $Cu_5Zn_2Al_3$ + ε $CuZn_4$
Medium Grey	27.1±0.2	67.5±0.3	5.4±0.2	ε $CuZn_4$
Medium Dark Grey	47.9±0.3	27.8±0.2	24.3±0.3	τ $Cu_5Zn_2Al_3$
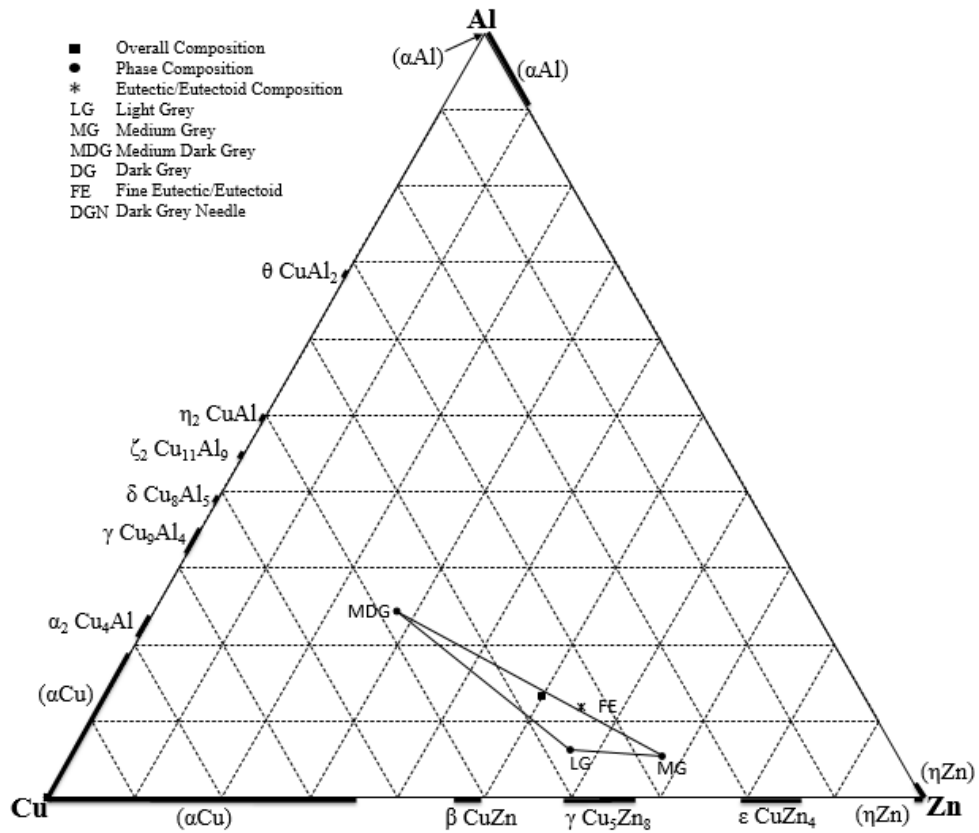
Figure 4.42: Composition plot of Sample 5 annealed at 240ºC.
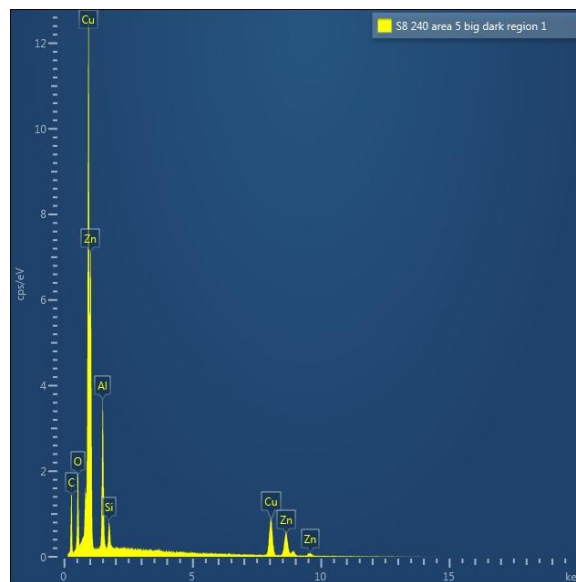
Figure 4.43: The EDS spectrum of a dark patch in Sample 5 showing high oxygen, carbon and silicon peaks.

75

4.2.2.7. Sample 7, Average Composition $Al_{41.6}Cu_{42.3}Zn_{16.1}$ (at.%)

Sample 7 exhibited grain boundary porosity at low magnification as shown in Figure 4.44. Three phases were observed at higher magnification as shown in Figure 4.45: a dark grey matrix, a medium dark grey phase, and a light grey precipitate. The higher scatter in the EDS data of the light grey precipitates in Table 4.18 implies that their analysis could have been affected by the other two phases. Even though the medium dark grey and the dark grey phases showed different contrasts and clear boundaries, they had virtually the same EDS results. Therefore, either the medium dark grey phase was too small to be analysed accurately, or the two are different phases of very close compositions. The porosity in Figure 4.44 most likely hindered complete homogenisation and may explain why the data point of the overall composition is not on the tie line in Figure 4.46.

Figure 4.44: SEM-BSE image of Sample 7 annealed at 240ºC showing porosity at low magnification.

76
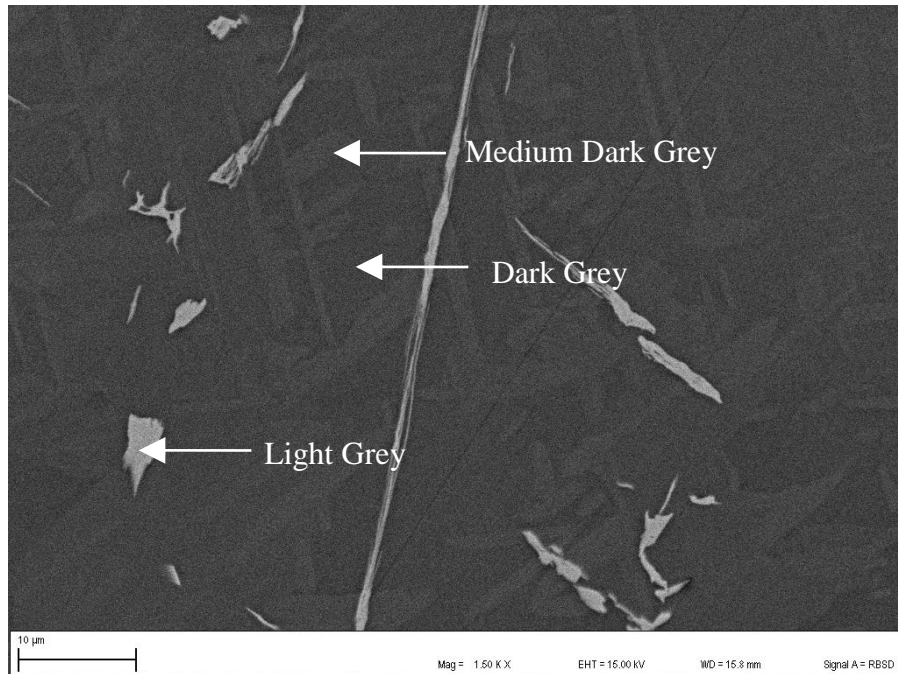
Figure 4.45: SEM-BSE image of Sample 7 annealed at 240ºC showing a dark grey matrix with light grey and medium dark grey precipitates.

Table 4.18: EDS data for Sample 7 annealed at 240ºC.

Phase Description	Composition (at.%)			Phase
	Cu	Zn	Al	
Overall	42.3±0.5	16.1±0.3	41.6±0.4	—
Light Grey	23.0±0.6	72.4±0.9	4.6±0.4	ε CuZn$_4$
Medium Grey	43.5±0.3	15.4±0.2	41.1±0.3	η_2 CuAl
Medium Dark Grey	43.4±0.2	15.4±0.2	41.2±0.2	ζ_2 Cu$_{11}$Al$_9$
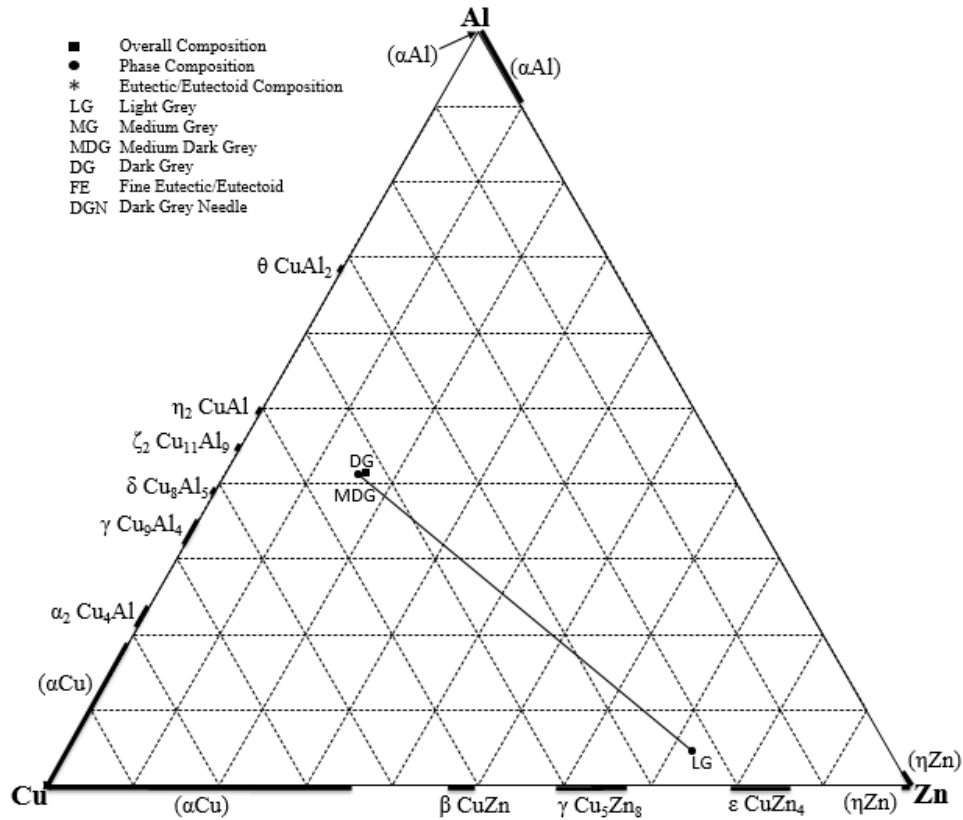
Figure 4.46: Composition plot of Sample 7 annealed at 240ºC.

4.2.2.8. Sample 8, Average Composition Al$_{25.6}$Cu$_{37.8}$Zn$_{36.6}$ (at.%)

Figure 4.47 is the SEM-SE image of Sample 8 at low magnification showing grain boundary porosity. The SEM-BSE image in Figure 4.48 shows that the sample had medium grey and dark grey phases in a light grey matrix. There was considerable scatter in the EDS data of the medium grey phase as recorded in Table 4.19. This may be explained by the fact that some medium grey phases analysed were small and inside the dark grey phase and their analyses may have been affected by them. The grain boundary porosity in Figure 4.47 most likely hindered homogenization and may explain why the overall analysis is outside the area bounded by the data points of the three phases in Figure 4.49.
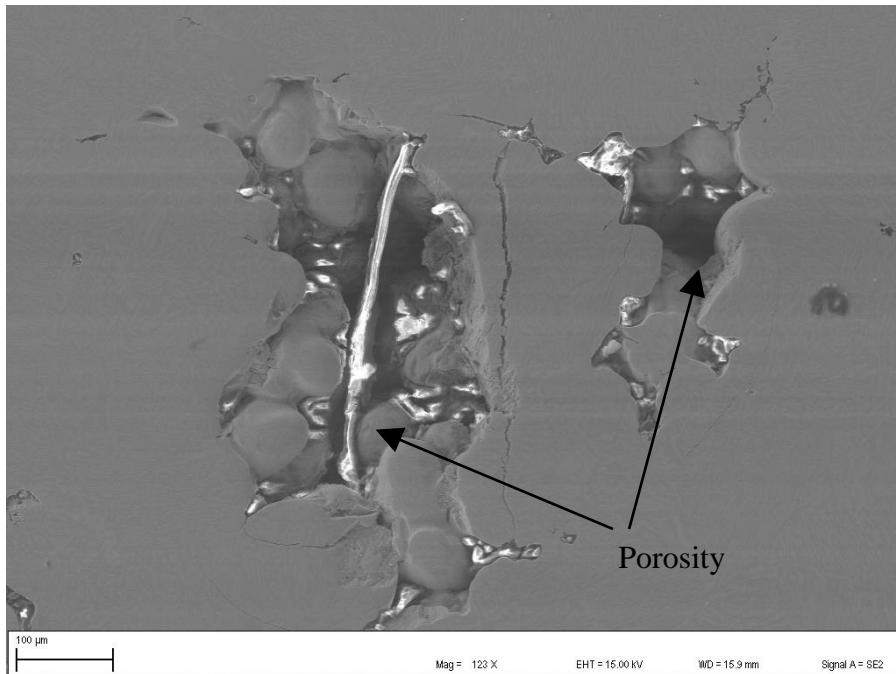
Figure 4.47: SEM-SE image of Sample 8 annealed at 240ºC showing porosity.
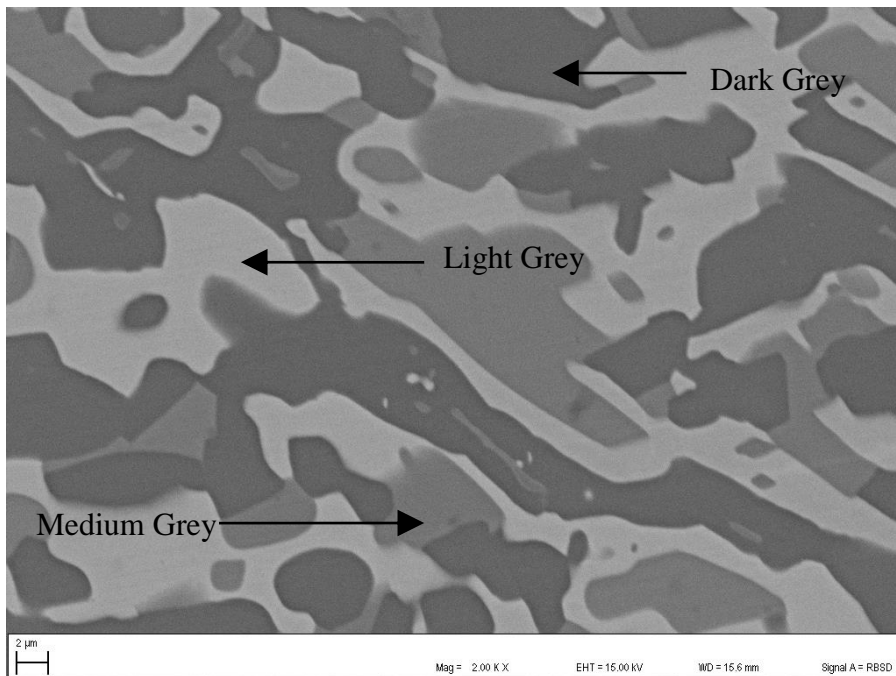
Figure 4.48: SEM-BSE image of Sample 8 annealed at 240ºC showing medium grey and dark grey phases in a light grey matrix.

Table 4.19: EDS data for Sample 8 annealed at 240ºC.

Phase Description	Composition (at.%)			Phase
	Cu	Zn	Al	
Overall	37.7±0.5	36.6±0.8	25.6±0.6	—
Light Grey	26.0±0.4	67.7±0.5	6.3±0.4	ε CuZn$_4$
Medium Grey	44.9±1.0	26.8±1.3	28.3±0.4	τ Cu$_5$Zn$_2$Al$_3$
Dark Grey	48.1±0.2	13.0±0.6	38.9±0.4	ζ$_2$ Cu$_{11}$Al$_9$
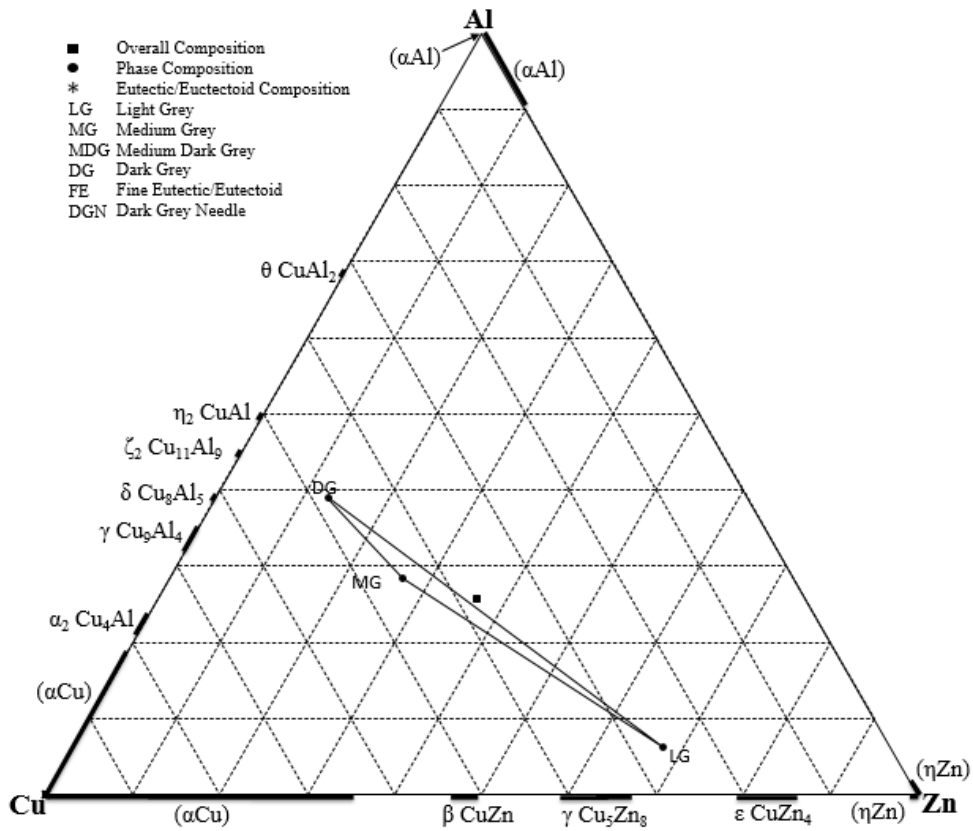
Figure 4.49: Composition plot of Sample 8 annealed at 240ºC.

4.2.2.9. Sample 9, Average Composition Al$_{21}$Cu$_{21.6}$Zn$_{57.4}$ (at.%)

The low magnification SEM-BSE image in Figure 4.50 illustrates the grain boundary porosity observed in Sample 9. Figure 4.51 is a higher magnification image of the sample showing dark grey and dark grey needle precipitates in a light grey matrix. The dark grey and the dark grey needle precipitates are very similar even though they gave slightly different EDS results in Table 4.20. The analyses of the dark grey needle precipitates may have been affected by the light grey matrix. The overall composition analysis of the sample lay outside the phase composition triangle as shown in Figure 4.52 This scatter may be explained by the grain boundary porosity.
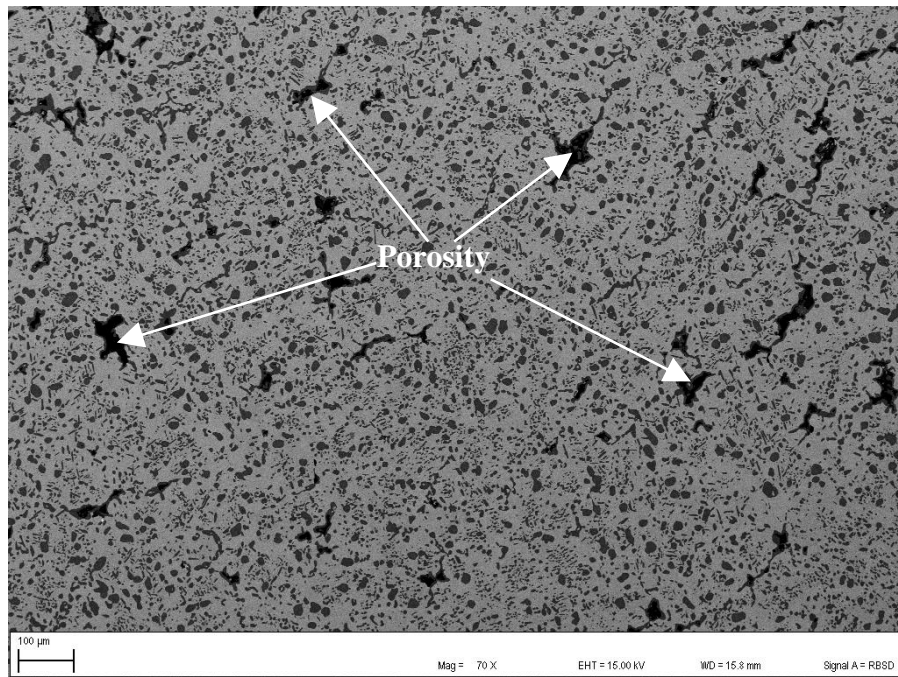
Figure 4.50: SEM-BSE image of Sample 9 annealed at 240ºC showing porosity.
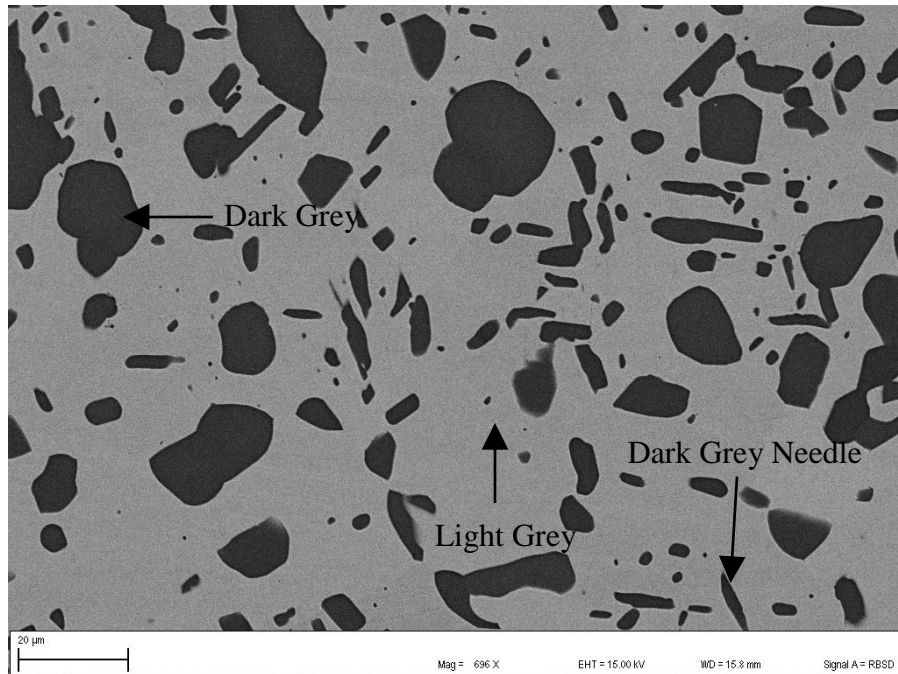
Figure 4.51: SEM-BSE image of Sample 9 annealed at 240ºC showing dark grey and dark grey needle precipitates in a light grey matrix.

Table 4.20: EDS data of Sample 9 annealed at 240ºC.

Phase Description	Composition (at.%)			Phase
	Cu	Zn	Al	
Overall	21.6±0.7	57.4±1.3	21.0±1.0	—
Light Grey	17.6±0.2	80.5±0.2	1.9±0.1	ε $CuZn_4$
Dark Grey	39.1±0.2	7.7±0.8	53.2±1.0	τ′ Cu_3ZnAl_4
Dark Grey Needle	38.4±0.3	6.4±0.6	55.2±0.4	τ′ Cu_3ZnAl_4
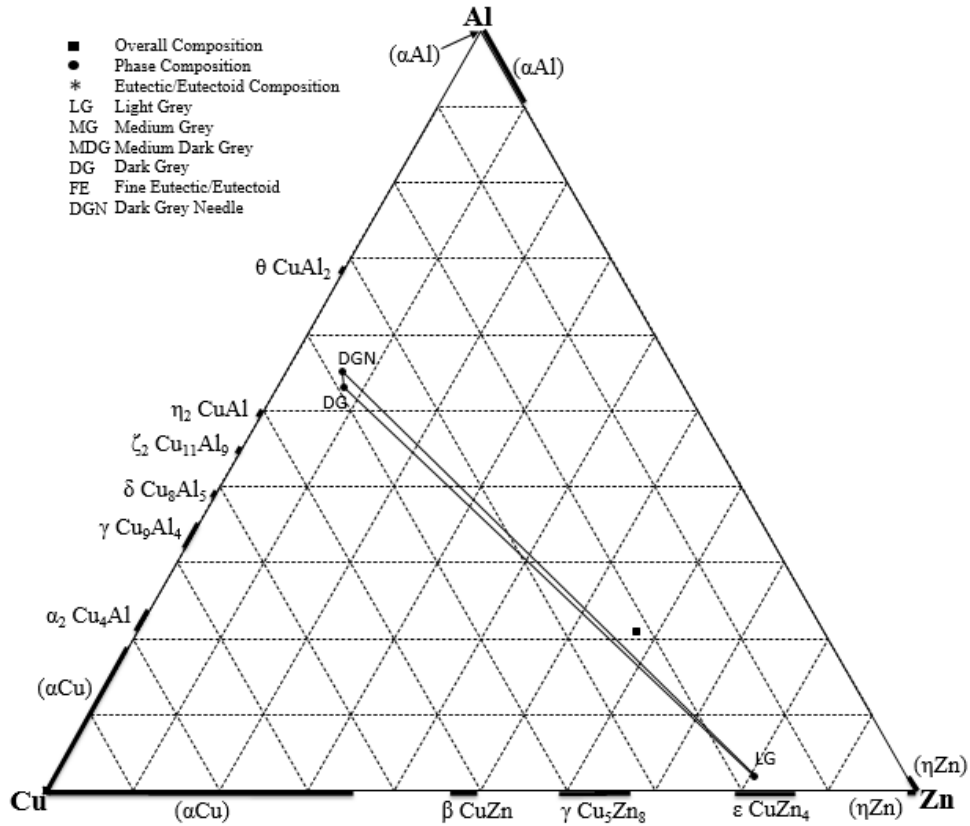
Figure 4.52: Composition plot of Sample 9 annealed at 240ºC.

4.2.2.10. Sample 12, Average Composition Al$_{10.9}$Cu$_{19.3}$Zn$_{69.7}$ (at.%)

The severity of the grain boundary porosity in Sample 12 shown in Figure 4.53 made it difficult to find isolated phase areas for EDS analysis. Figure 4.54 is a high magnification SEM-BSE image of the sample showing dark grey precipitates surrounded by dark patches in a light grey matrix. The EDS data is shown in Table 4.21. The porosity in Figure 4.53 may explain why the overall composition data point is not on the tie line in Figure 4.55, since it could have hampered homogeneity. The dark patches were carbon and oxides of the constituent elements as indicated by the high carbon and oxygen peaks in the spectrum taken from these regions in Figure 4.56.
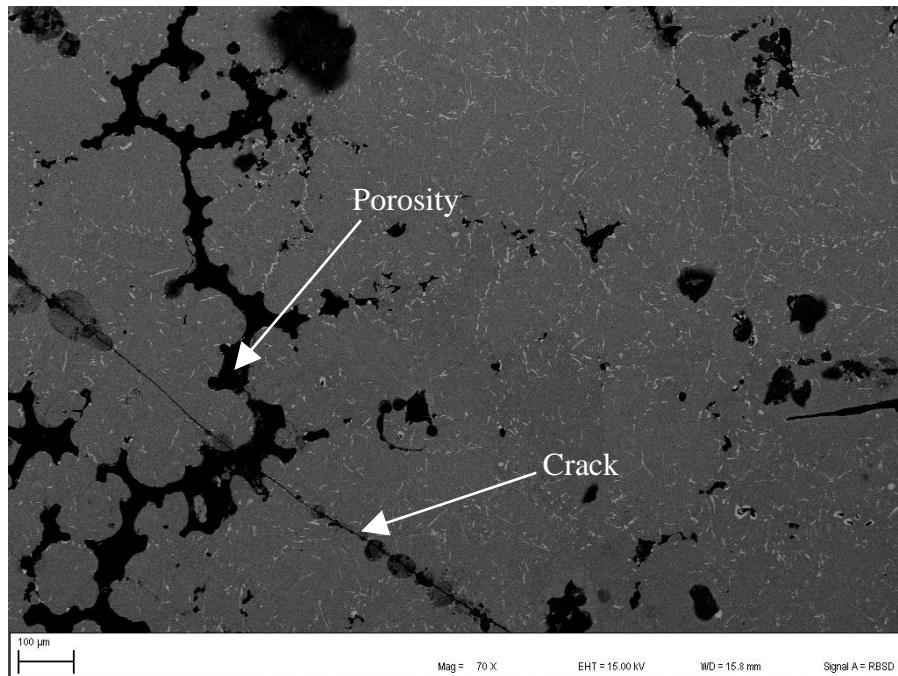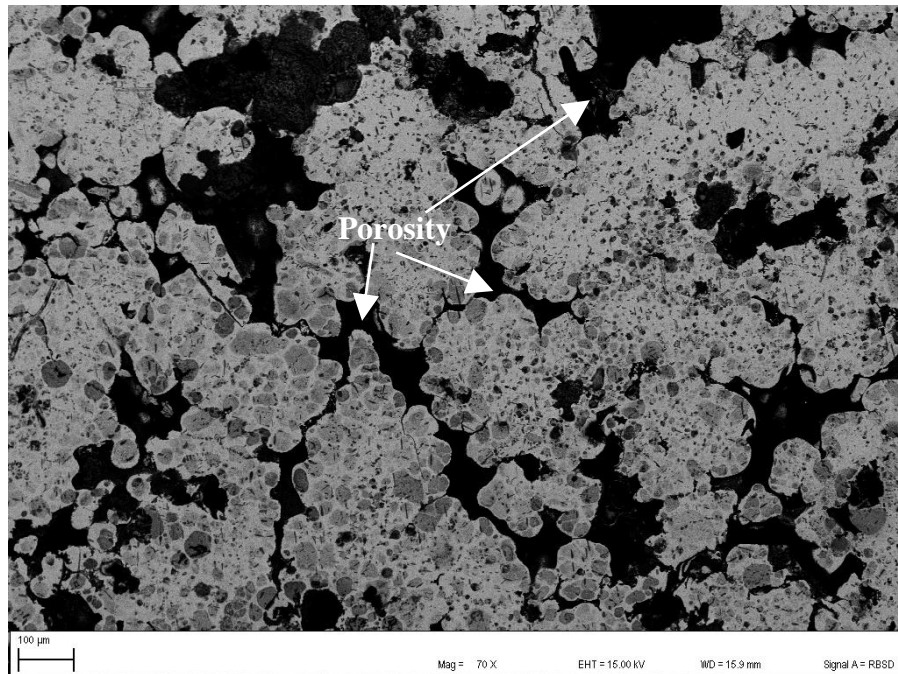
Figure 4.53: SEM-BSE image of Sample 12 annealed at 240ºC showing porosity at low magnification.
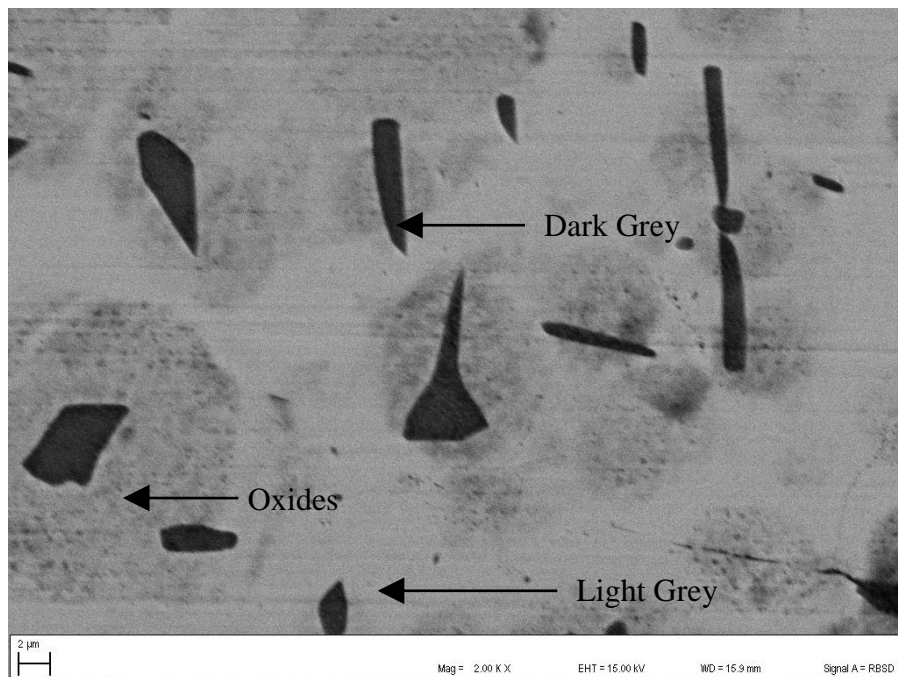
Figure 4.54: SEM-BSE image of Sample 12 showing dark grey precipitates in a light grey matrix.

84

Table 4.21: EDS data for Sample 12 annealed at 240ºC.

Phase Description	Composition (at.%)			Phase
	Cu	Zn	Al	
Overall	19.3±0.3	69.7±0.4	10.9±0.4	—
Light Grey	20.6±0.2	76.2±0.2	3.2±0.1	ε CuZn$_4$
Dark Grey	40.0±0.5	10.0±0.1	50.0±0.5	τ' Cu$_3$ZnAl$_4$
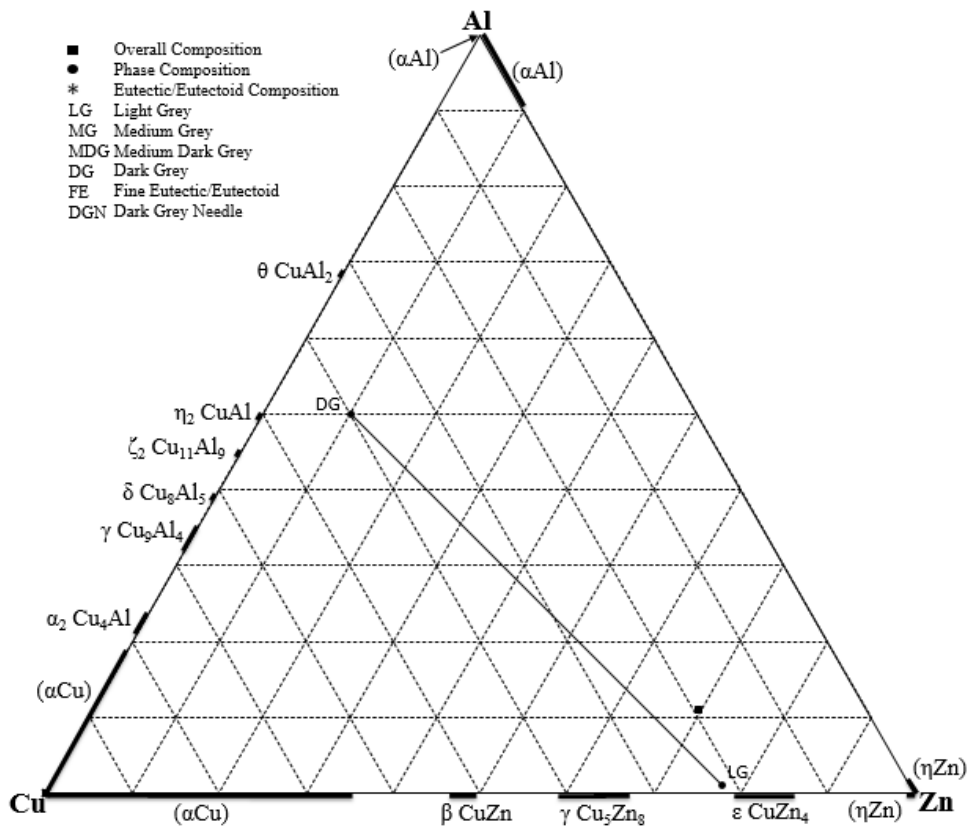
Figure 4.55: Composition plot of Sample 12 annealed at 240ºC.
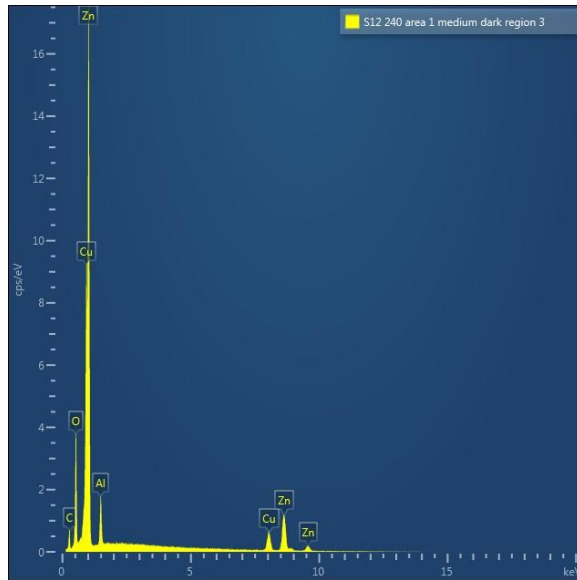
Figure 4.56: The EDS spectrum of a dark patch in Sample 12 showing high oxygen and carbon peaks.

5. DISCUSSION

5.1. Overview

Table 4.1 showed significant differences between the actual sample compositions and the target sample compositions. These differences were attributed to the use of excess Zn to compensate for expected losses and the difficulty of achieving accurate weights using pellets. However, these differences did not impact negatively on the results since apart from Sample 1 (b) annealed at 240ºC, all other sample composition were in multi-phase regions.

The oxide and carbon inclusions observed in virtually all alloys may have been introduced during casting. Moreover, Sample 2 (a) and Sample 5 showed traces of silicon which were deduced to have come from the silicon carbide lapping compound that was used during polishing. However, these contaminations were not significant and were assumed not to have considerably affected the results. Samples 3, 7, 8, 9 and 12 showed significant porosity which hindered complete homogenisation of the samples. This can explain why their overall analyses lay outside the expected regions.

Since the Al-Cu-Zn system is widely researched, its phases are known and can be identified even without XRD data. The phase identities recorded in Table 4.1 to Table 4.21 were identified by comparing their data points (on the composition plots) with the compositions of known binary and ternary phases obtained from the complete isothermal section of the Al-Cu-Zn system at 350ºC [1] shown in Figure 2.12.

5.2. Partial Isothermal Sections

5.2.1. Isothermal Section at 200ºC

Figure 5.1 is a combined plot of all overall and phase compositions of alloys heat treated at 200ºC. Figure 5.2 is an attempt to construct phase boundaries and ranges of composition using the data in Figure 5.1. Since each phase data point represents a phase boundary, data points representing the same phase were joined. For binary phases, the lines were extrapolated to meet their corresponding boundaries on the binary edges.
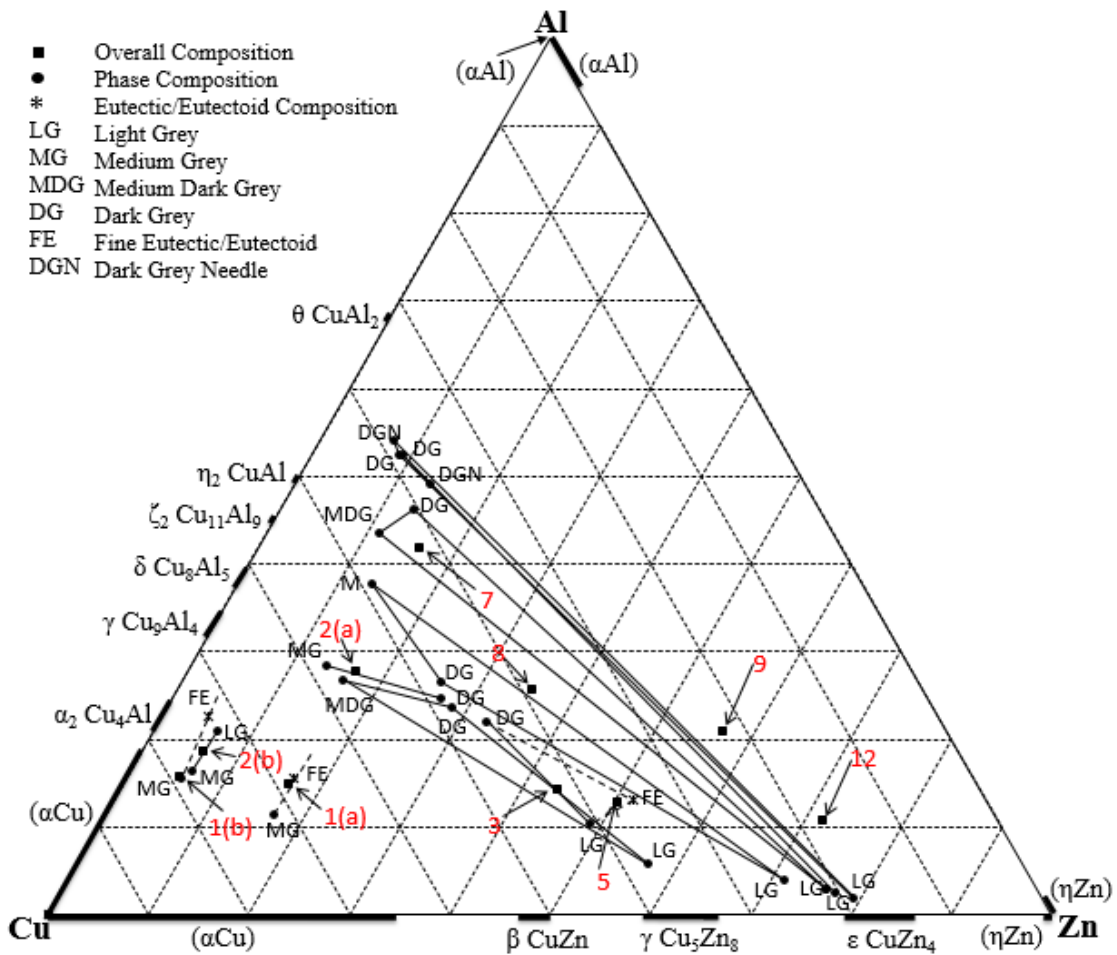
Figure 5.1: Composition plot of all overall and phase composition EDS data of alloys annealed at 200ºC.

Eight phases were identified in alloys annealed at 200ºC namely: the binary (αCu), γ Cu_9Al_4, $η_2$ CuAl, $ζ_2$ $Cu_{11}Al_9$, γ Cu_5Zn_8 and ε $CuZn_4$ phases, and the ternary τ $Cu_5Zn_2Al_3$ and τ′ Cu_3ZnAl_4 phases. No new phases were observed at these temperatures. Although other phases are believed to exist within the studied region, they were not observed in any alloy. Therefore, in Figures 5.3, the possible ranges of composition of $α_2$ Cu_4Al, δ Cu_8Al_5 and β CuZn were estimated using the isothermal section at 350ºC compiled by Ghosh et al. [1].
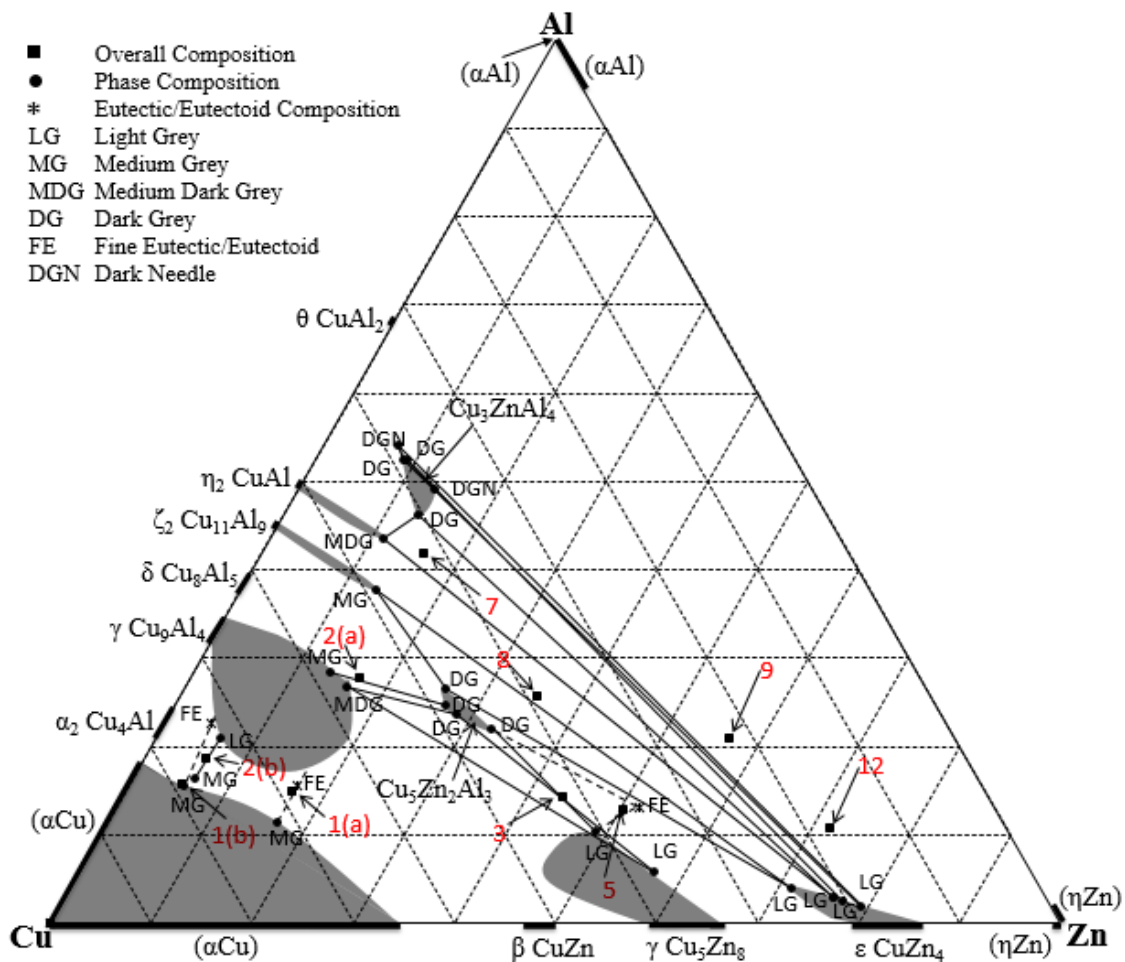
Figure 5.2: Possible phase boundaries and ranges of composition of alloys annealed at 200ºC.

Figure 5.3 is the partial isothermal section at 200°C with the assumed two and three-phase regions drawn as dotted lines since they were inferred.
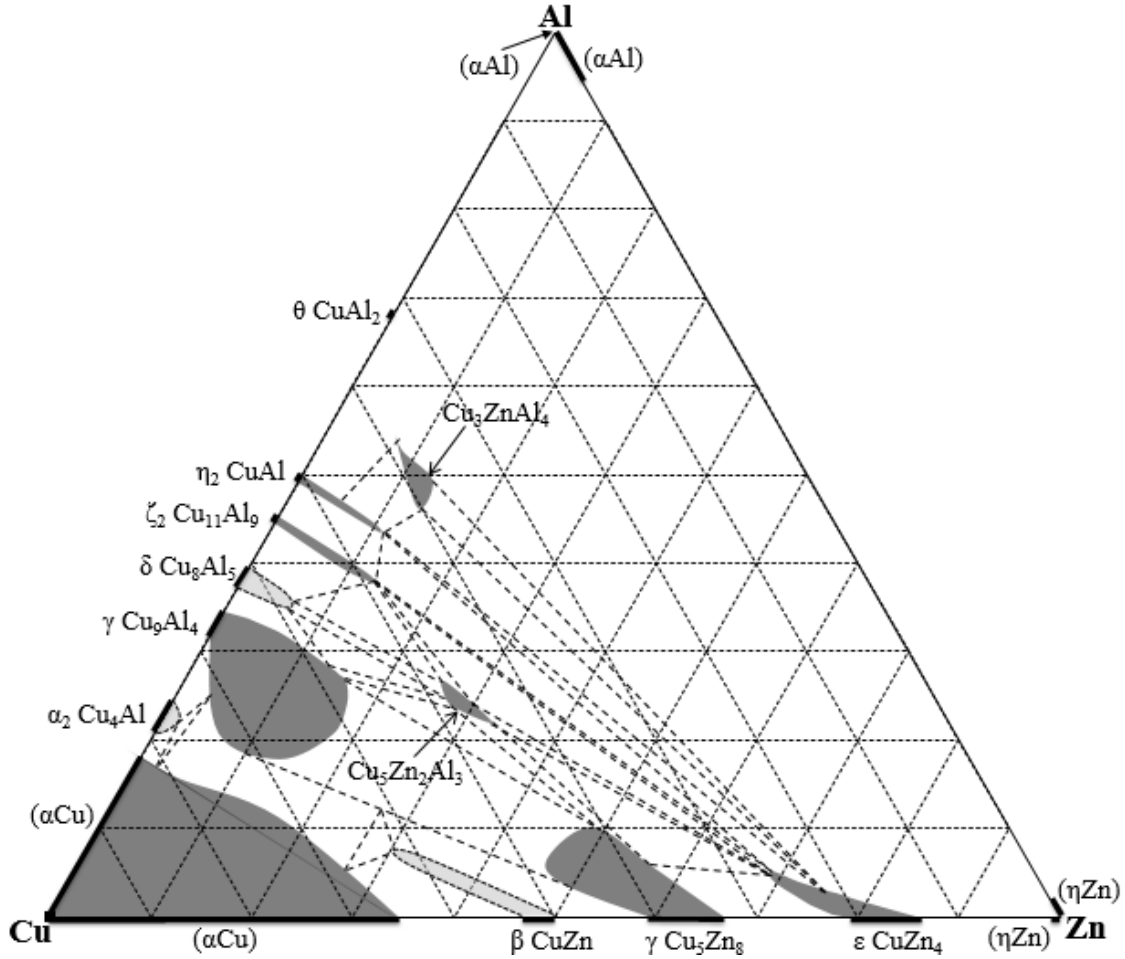
Figure 5.3: Partial isothermal section of Al-Cu-Zn system at 200°C.

The (αCu) solid solution and a eutectic of (αCu) + γ Cu₉Al₄ were present in Samples 1 (a) and 1 (b). The (αCu) boundary from the Al-Cu binary edge to the Cu-Zn edge did not follow the dotted profile inferred by Ghosh et al. [1] in Figure 2.7.

Figures 2.1 and 2.3 shows that the α_2 Cu$_4$Al and β CuZn phases are present at 200ºC. However, they were not observed in any alloy. This may be explain by the fact that the targeted compositions were not met.

As pointed out in the literature survey (Chapter 2), there has been considerable controversy in literature surrounding the nature of the γ phase which Liang and Schmid-Fetzer [7] traced to Bauer and Hansen [67] in 1932. Bauer and Hansen [67] proposed a continuous single solid phase field of the γ phase from the AlCu binary edge to the CuZn edge, even though their assessment did not go past the Cu-rich boundary of γ. This interpretation was accepted in several subsequent works [8-10, 19, 20 and 66]. Liang and Chang [4] still adopted this interpretation in their CALPHAD thermodynamic modelling in 1998, even after Kandaurov et al. [77], in 1972, and Ashrimbetov et al. [78], in 1973, reported a two-phase region between AlCu-side γ and CuZn-side γ and suggested that the two phases only merge at high temperatures where they have the same crystal structure. This work confirmed that γ Cu$_9$Al$_4$ and γ Cu$_5$Zn$_8$ are distinct phases since a three-phase region of γ Cu$_9$Al$_4$, τ Cu$_5$Zn$_2$Al$_3$ and γ Cu$_5$Zn$_8$ was observed in Sample 3.

The ternary phase τ Cu$_5$Zn$_2$Al$_3$ was observed in Samples 2 (a), 3, 5 and 8. The solubility of Cu in τ Cu$_5$Zn$_2$Al$_3$ of Köster and Moeller [19] of between 56 wt% (48.3 at.%) and 58 wt.% (50.3 at.%) Cu at 200ºC did not agree with that in this work of between 45.3 and 48.4 at.% Cu.

The $\tau\prime$ Cu$_3$ZnAl$_4$ phase, which is stable below 277ºC [79], was found in Samples 7, 9 and 12. Its solubility range of between 7.4 and 13.5 at.% Zn differed slightly with that given by Köster and Moeller [19] of between 10 wt% (6.8 at.%) Zn and 18 wt% (13.1 at.%) Zn.

The binary ε CuZn$_4$ phase was identified in Samples 5, 7, 8, 9 and 12. Its plotted phase field in Figure 5.3 extended up to a maximum Cu content of 3.9 at.% Al. This is different from Köster's

and Moeller's [19] diagram in Figure 2.10 which shows that the solubility limit of Al in ε CuZn$_4$ is about 3.5 at.%.

The ζ_2 Cu$_{11}$Al$_9$ and η_2 CuAl phases showed maximum Zn content of 13.3 at.% and 11.2 at.% respectively.

Two factors may account for the differences observed between the results of this work and the earlier work of Köster and Moeller [19] at 200°C. Firstly, the samples may not have been exposed to the correct isothermal temperature since the furnace used was old. It's possible that its thermocouple may not have been working properly. Secondly, cold water (at 20°C) rather than iced-water was used to quench the samples and the ampoule was not broken as the samples were being put in the quenching water. As a result, the quenching effect may not have been severe enough to trap the isothermal phases.

5.2.2. Isothermal Section at 240°C

Overall and phase composition EDS data of all alloys annealed at 240°C were plotted in Figure 5.4 This information was used in tandem with the constituent binary diagrams to join the points representing the same phase resulting in Figure 5.5. Figure 5.6 is the isothermal section at this temperature with the assumed two and three-phase regions drawn in dotted lines as they were inferred.

Phases identified at 240°C were: (αCu), γ Cu$_9$Al$_4$, γ Cu$_5$Zn$_8$, ζ_2 Cu$_{11}$Al$_9$, η_2 CuAl, ε CuZn$_4$, τ Cu$_5$Zn$_2$Al$_3$ and τ' Cu$_3$ZnAl$_4$.

The boundary profile in of (αCu) in Figure 5.6 is different from the dotted profile inferred by Ghosh et al. [1] in Figure 2.8.

Although Gebhardt [20] did not study the entire composition range of τ' Cu$_3$ZnAl$_4$, his diagram in Figure 2.11 shows that it has a minimum Cu composition of 55.3 wt% (38.3 at.%) which is in agreement with the same composition in this work of 38.4 at.%.

Gebhardt's [20] diagram in Figure 2.11 shows that the maximum solubility of Al in ε CuZn$_4$ is about 1.9 wt% (4.5 at.%). That composition is less than the 6.3 at.% in Figure 5.6. This difference in solubility limit of Al in ε between the two diagrams may be explained by the quenching method used in this study which might not have frozen diffusion.
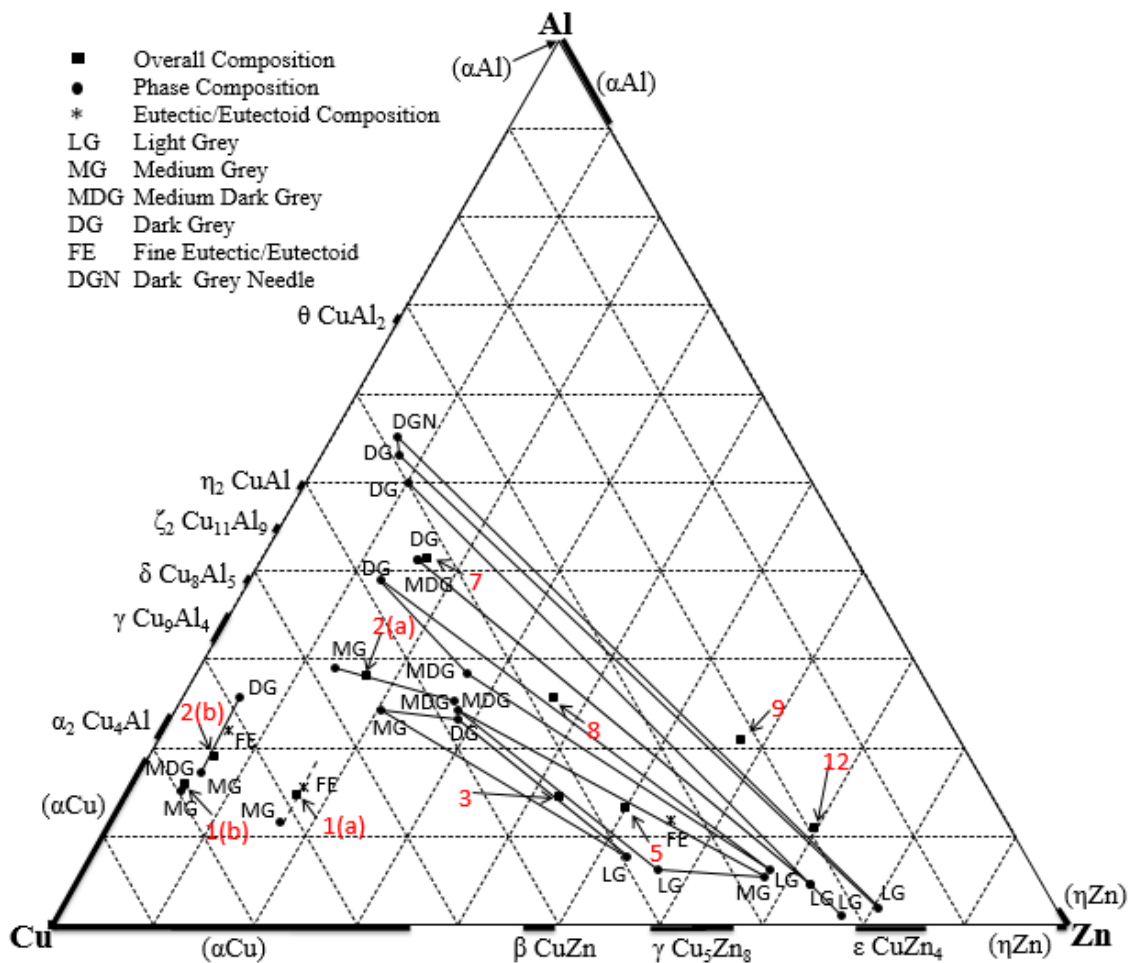
Figure 5.4: Composite plot of the EDS data of all alloys annealed at 240ºC.
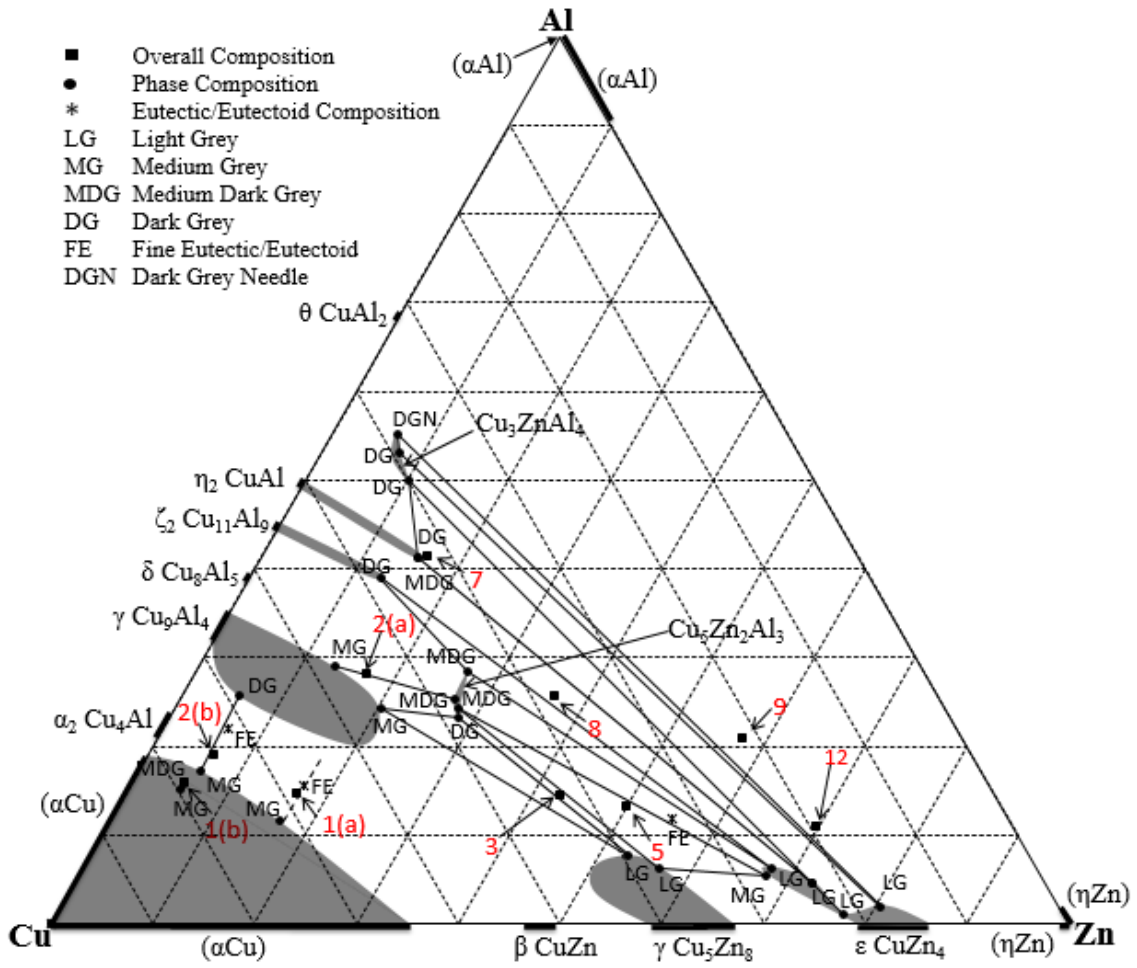
Figure 5.5: Plot of possible phase boundaries of alloys annealed at 240ºC.
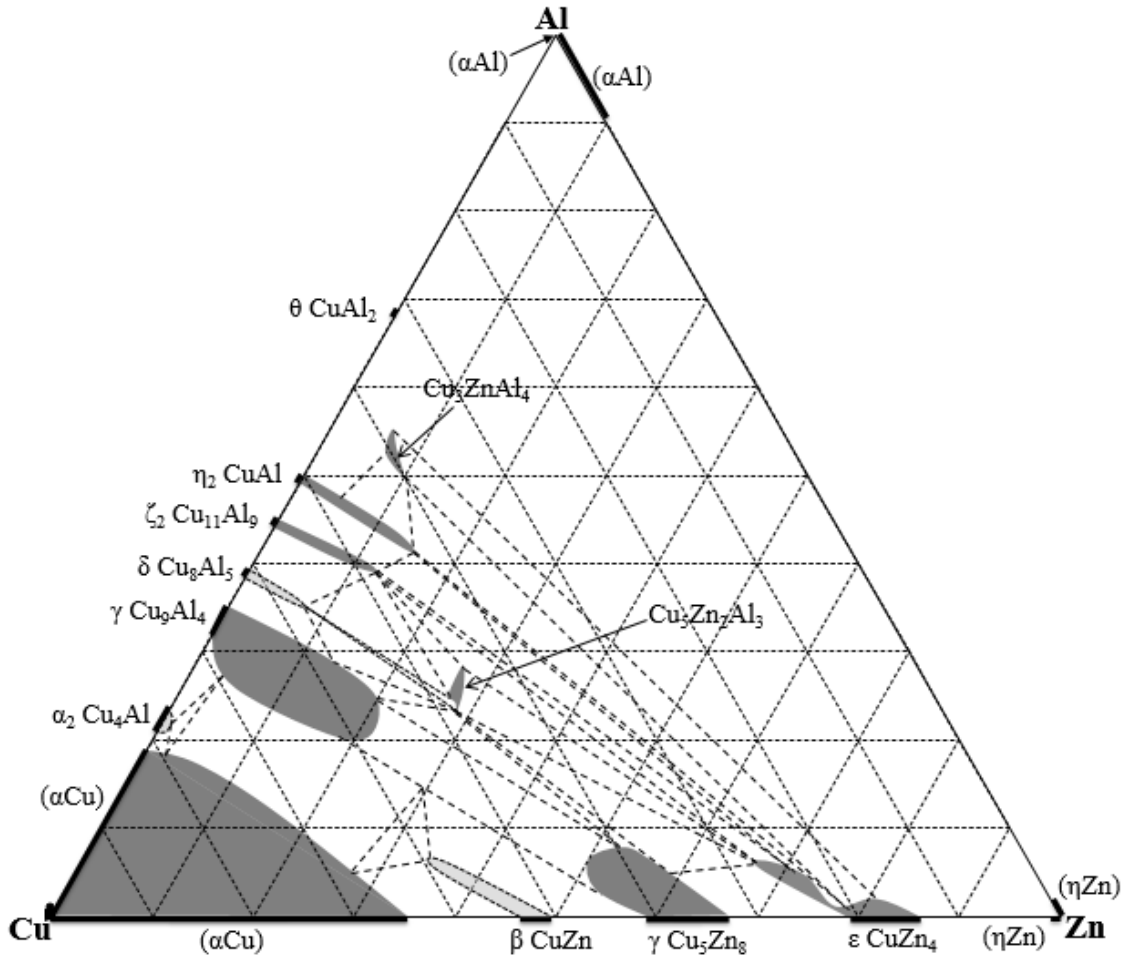
Figure 5.6: Isothermal section of Al-Cu-Zn at 240ºC.

5.2.3. Comparison of the 200ºC and the 240ºC isothermal sections

The dark grey phases and dark grey needle precipitates in sample 9 in Figures 4.19 and 4.43 are most likely the same phase at different orientation. It is very common for precipitates to be on {100} planes which would mean that they are 90º oriented from each other.

The solubility of Al and Zn in (αCu) increased with temperature. This was observed in Sample 1 (b) in which the (αCu) + γ Cu_9Al_4 eutectic identified at 200ºC disappeared at 240ºC leaving the single phase (αCu) solid solution.

The solubility range of Cu in γ Cu_9Al_4 decreased from between 57.2 at.% Cu and 72.8 at.% Cu at 200°C to between 57.2 at.% Cu and 68.7 at.% Cu at 240°C. A three-phase region of γ Cu_9Al_4, γ Cu_5Zn_8 and τ was also observed in Sample 3 annealed at 240°C. This is further confirmation that that γ Cu_9Al_4 and γ Cu_5Zn_8 are different phases.

The τ $Cu_5Zn_2Al_3$ phase was observed to dissolve less Zn (28.5 at.%) at 240°C than at 200°C (32.7 at.%). Compared to the τ' $Cu_3Zn_1Al_4$ at 200°C, the τ' $Cu_3Zn_1Al_4$ phase field at 240°C shrank from between 7.4 and 13.5 at.% Zn to 6.4 and 10.0 at.% Zn.

The ε $CuZn_4$ phase field reduced from a maximum Al content of 13.3 at.% at 200°C in Figure 5.3 to 6.3 at.% in Figure 5.6.

The maximum solubility of Zn in ζ_2 $Cu_{11}Al_9$ slightly decreased from 13.3 at.% at 200°C to 13.0 at.% at 240°C. The solubility of Zn in η_2 CuAl increased with temperature from 11.2 at.% to 15.4 at.% in Figures 5.3 and 5.6 respectively.

6. CONCLUSIONS AND RECOMMENDATIONS FOR FUTURE WORK

6.1. Conclusions

The following conclusions can be drawn from this study:

1. Eight phases were identified at both 200ºC and 240ºC, namely: the binary phases (αCu), γ Cu_9Al_4, η_2 CuAl, γ Cu_5Zn_8, ζ_2 $Cu_{11}Al_9$ and ε $CuZn_4$ phases, and the ternary phases τ $Cu_5Zn_2Al_3$ and τ' Cu_3ZnAl_4.

2. The γ phase exist as two distinct phases (γ Cu_9Al_4 and γ Cu_5Zn_8).

3. No new ternary phases exists at 200ºC and 240ºC.

4. The phases α_2 Cu_4Al, δ Cu_8Al_5 and β CuZn were not observed in any alloy.

5. The ranges of composition of the τ $Cu_5Zn_2Al_3$, τ' Cu_3ZnAl_4 and ε $CuZn_4$ phases found at 200ºC were different from those reported by Köster and Moeller [19] at 200ºC.

6. The solubility limit of Al in ε $CuZn_4$ at 240ºC was different from that observed by Gebhardt [20] at 240ºC.

6.2. Recommendations

The following areas are recommended for further study:

1. To carry out an XRD analysis of the samples prepared in this study to confirm the phases identified by EDS at 200ºC and 240ºC.

2. To determine the phase boundaries of α_2 Cu_4Al, δ Cu_8Al_5 and β $CuZn$ at 200ºC and 240ºC which were not found in this study.

3. To re-evaluate the composition ranges of the ϵ $CuZn_4$, τ $Cu_5Zn_2Al_3$ and τ' Cu_3ZnAl_4 phases at 200ºC to clear the differences between the results of this study and Köster and Moeller's [19], and Gebhardt's [20] earlier studies.

4. To determine of the temperature at which γ Cu_9Al_4 and γ Cu_5Zn_8 form a single phase field from the Cu-Zn to the Al-Cu binary edge.

REFERENCES

1. Ghosh, G., Humbeeck, J. and Perrot, P., Aluminium-Copper-Zinc, Ternary Alloy Systems: Phase Diagrams, Crystallographic and Thermodynamic Data, MSIT, Landolt-Börnstein New Series IV, 11A (2), (2005) 182-205.

2. Gomidželović, L., Mihajlović, I., Kostov, A. and Živković, D., Cu–Al–Zn system: Calculation of thermodynamic properties in liquid phase, *Hemijska Industrija,* 67(1), (2013) 157–164.

3. Huang, W., On the selection of shape memory alloys for actuators, *Materials & Design*, 23 (2002) 11-19.

4. Huang, W.M., Ding, Z., Wang, C.C., Wei, J., Zhao, Y. and Purnawal, H., Shape memory materials, *Materials Today,* 13 (2010) 54–61.

5. Li, J., Zhang, W., Gao, L., Gu, P., Sha, K. and Wan, H. Methanol synthesis on Cu–Zn–Al and Cu–Zn–Al–Mn catalysts, *Applied Catalysis A*, 165 (1997), 411–417.

6. Huber, F., Meland, H., Rønning, M., Venvik, H. and Holmen, A. Comparison of Cu–Ce–Zr and Cu–Zn–Al mixed oxide catalysts for water-gas shift, *Topics in Catalysis*, 45 (2007) 101–104.

7. Martinez-Flores, E., Negrete, J. and Torres-Villasenor, G., Structure and properties of Zn–Al–Cu alloy reinforced with alumina particles, *Materials & Design,* 24 (2003) 281–286.

8. Liang, H. and Chang, Y.A., A Thermodynamic description for the Al-Cu-Zn system*, Journal of Phase Equilibria*, 19(1), (1998) 25-37.

9. Köster, W., The constitution and the volume changes of Zn-Cu-Al alloys. III. Summary of the equilibrium relationships in the system Cu-Al-Zn, *Zeitschrift für Metallkunde,* 33 (1941) 289-296 (in German).

10. Arndt, H.H. and Moeller, K., The ternary phase of the Cu-Al-Zn system. II. The T-phase field above 500ºC, *Zeitschrift für Metallkunde*, 51 (1960) 656-662 (in German).

11. Liang, S.M. and Schmid-Fetzer, R., Thermodynamic assessment of the Al–Cu–Zn system, Part III: Al–Cu–Zn ternary system*, Calphad*, 52, (2016) 21–3722.

12. Miettinen, J.*,* Thermodynamic description of the Cu-Al-Zn and Cu-Sn-Zn systems in the copper-rich corner*, Calphad*, 26(1), (2002) 119-139.

13. Chen, H., Xin, X., Dong, D.Y., Ren, Y.P. and Hao, S.M., Study on the stability of the T' phase in the Al-Zn-Cu ternary system, *Acta Metallurgica Sinica*, 17(3), (2004) 269-273.

14. Villegas-Cardenas, J.D., Saucedo-Muñoz, M.L., Lopez-Hirata, V.M., Dorantes-Rosales, H.J. and Gonzalez-Velazquez, J.L., Effect of phase transformations on hardness in Zn–Al–Cu alloys, *Materials Research*, 17(5), (2014)1137-1144.

15. Zhou, L., Zhu, X., Ji-qing, B., Gen-ying, X. and Zheng, F., Atom exchange of martensite in Cu-13Zn-15Al alloy during non-isothermal aging, *Transaction of Non-ferrous Metals Society of China*, 16 (2006) 1064-1068.

16. Wei, Z.G. and Sandstrom, R., Shape memory materials and hybrid composites for smart systems, *Journal of Materials Science*, 33 (1998) 3743-3762.

17. Kim, S.J., Kim, K.S., Kim, S.S., Kang, C.Y. and Suganuma, K., Characteristics of Zn-Al-Cu alloys for high temperature applications, *Materials Transactions*, 49(7), (2008) 1531-1536.

18. Köster, W. and Moeller, K., The constitution and volume changes of Zn-Cu-Al alloys. V. The division of the ternary phases at low temperatures, *Zeitschrift für Metallkunde,* 34, (1942) 206-207 (in German).

19. Arndt, H.H. and Moeller, K., The ternary phase of the Cu-Al-Zn system. I. The decomposition of the T-phase at 200-300ºC, *Zeitschrift für Metallkunde*, 51, (1960) 596-600 (in German).

20. Gebhardt, E., The constitution and the volume changes of Zn-Cu-Al alloys. VI. Survey of the equilibrium relationships on the Zn-Al side under 350ºC, *Zeitschrift für Metallkunde*, 34, (1942) 208-215 (in German).

21. Alloy Phase Diagrams, ASM Handbook, ASM International, Volume 3 (1992).

22. Ponweiser, N., Lengauer, C.L. and Richter, K.W., Re-investigation of phase equilibria in the system Al–Cu and structural analysis of the high-temperature phase η_1-$Al_{1-\delta}$ Cu, *Intermetallics*, 19 (2011) 1737–1746.

23. Murray, J.L., The Aluminium–Copper System, *International Metal Reviews*, 30 (1985) 211–233.

24. Liu, X.J., Ohnuma, I., Kainuma, R. and Ishida, K., Phase equilibria in the Cu-rich portion of the Cu-Al binary system, *Journal of Alloys and Compounds*, 264 (1998) 201-208.

25. Riani, P., Arrighi, L., Marazza, R., Mazzone, D., Zanicchi, G. and Ferro R., Ternary rare-earth aluminum systems with copper: A review and a contribution to their assessment, *Journal of Phase Equilibrium and Diffusion*, 25 (2004) 22-52.

26. Saunders, N., System Al-Cu, in: I. Ansara, A.T. Dinsdale, M.H. Rand (Eds.), *COST 507 - Thermochemical Database for Light Element Alloys*, 2 (1998) 28-33.

27. Friauf, J.B., The crystal structure of two intermetallic compounds, *Journal of American Chemical Society*, 49 (1927) 3107-3114.

28. Ponweiser, N. and Richter, K.W., New investigation of phase equilibria in the system Al–Cu–Si, *Journal of Alloys and Compounds*, 512 (2012) 252– 263.

29. Preston, G.D., An X-ray investigation of some copper–aluminum alloys, *Philosophical Magazine A,* 12 (1931) 980–993.

30. Bradley, A.J., Goldschmidt, H.J. and Lipson, H., The intermediate phases in the aluminium-copper system after slow cooling, *Journal of the Institute of Metals*, 63 (1938) 149-162.

31. El-Boragy, M., Szepan, R. and Schubert, K.,Crystal structure of Cu_3Al_{2+} (h) and CuAl (r*)*, *Journal of Less-Common Metals*, 29(2) (1972) 133-140 (in German).

32. Lukas, H.L. and Lebrun, N., Al-Cu-Si (aluminium-copper-silicon). In: Effenberg G, Ilyenko S, editors. Springer Materials - The Landolt-Börnstein Database (2005) 135-147.

33. Stockdale, D., The aluminium–copper alloys of intermediate composition, *Journal of the Institute of Metals*, 31 (1924) 275–294.

34. Gulay, L.D. and Harbrecht, B., The crystal structure of zeta (1)-Al_3Cu_4, *Journal of Alloys Compounds*, 367 (2004) 103-108.

35. Dong, C., Zhang, Q.H., Wang, D.H. and Wang, Y.M., Al-Cu approximants in the Al$_3$Cu$_4$ alloy, *The European Physical Jornal B*, 6 (1998) 25-32.

36. Westman, S., Phase analysis at 660ºC of the gamma region of the copper-aluminium system, *Acta Chemica Scandinavica*, 19 (1965) 2369-2372.

37. Seshadri, S.K. and Downie, D.B., High-temperature lattice parameters of copper-aluminium alloys, *Metal Science and Heat Treatment*, 13 (1979) 696-698.

38. Kowalski M. and Spencer P.J., Thermodynamic re-evaluation of the Cu-Zn system, *Journal of Phase Equilibria,* 14(4) (1993) 432-438.

39. Raynor, G.V., Annoted Equilibrium Diagrams, The Institute of Metals, London (1944).

40. Hansen, M., and Anderko, K., Constitution of Binary Alloys, McGraw-Hill Book Company, New York (1958).

41. Massalski, T.B., Murray, J.L., Bennett, L.H. and Baker, H., Binary Alloy Phase Diagrams, American Society for Metals, Metals Park, Ohio (1986).

42. Miodownik, A.P*.,* Binary Alloy Phase Diagrams, Materials Information Society, Materials Park, Ohio (1990).

43. Predel B., Cu-Zn (copper-zinc), Landolt-Börnstein-Group IV Physical Chemistry, 5(d), (1994) 1-11.

44. Roberts-Austen, W.C., Proceedings of the Institution of Mechanical Engineers (London), (1897) 36.

45. Spencer, P.J., A thermodynamic evaluation of the Cu–Zn system, *Calphad,* 10 (1986) 175–185.

46. Kowalski, M. and Spencer, P.J., System Cu–Zn, in: I. Ansara, A.T. Dinsdale, M.H. Rand (Eds.), *COST 507: Thermochemical Database for Light Metal Alloys.* Definition of Thermodynamical and Thermophysical Properties to Provide a Database for the Development of New Light Alloys, 2, (1998)186–191.

47. David, N., Fiorani, J.M., Vilasi, M. and Hertz, J., Thermodynamic reevaluation of the Cu–Zn system by electromotive force measurements in the zinc-rich part, *Journal of Phase Equilibria*, 24 (2003) 240–248.

48. Gierlotka, W. and Chen, S.W., Thermodynamic descriptions of the Cu–Zn system, *Journal of Materials Research*, 23 (2008) 258–263.

49. Wang, J., Xu, H., Shang, S., Zhang, L., Du, Y., Zhang, W., Liu, S., Wang, P. and Liu, Z.K., Experimental investigation and thermodynamic modelling of the Cu–Si–Zn system with the refined description for the Cu–Zn system, *Calphad*, 35 (2011) 191–203.

50. West, E.G., Copper and its alloys, Ellis Horwood Limited, Chichester, England (1982).

51. Balesdent, D., *Bulletin de la Société Chimique de France*, France (1963) 27-56 (in French).

52. Walker, C.B. and Keating, D.T., Neutron diffraction study of short-range order in β-Cu-Zn*, Physical Review*, 130 (1963) 1726-1730.

53. Von Heidenstam, O., Johansson, A. and Westman, S., A redetermination of the redistribution of atoms in Cu$_5$Zn$_8$, Cu$_5$Cd$_8$, and Cu$_9$Al$_4$, *Acta Chemica Scandinavica,* 22 (1968) 653-661.

54. Iwasaki, H. and Okada, M., The γ-brass structure at high temperature, *Acta Crystallographica Section B: Structural Science*, 36 (1980) 1762-1765.

55. Tesfaye, F. and Taskinen, P., Phase equilibria and thermodynamics of the system Zn-As-Cu-Pb-S at temperatures below 1173 K, *Science and Technology*, 7 (2011) 1-46.

56. Presnyyakov, A. A., Goltban, Y. A. and Cherptyyakova V. C., Concerning the equilibrium diagram of the Al-Zn alloys, *Russian Journal of Physical Chemistry,* 35 (1961) 623–633 (in Russian).

57. Goldak, G.R. and Parr, J.G., A high-temperature X-ray-diffractometer study of the aluminium-zinc system in the region 40-75 wt% Zn, *Journal of the Institute of Metals*, 93 (1963) 230-233.

58. Murray, J.L., The Al-Zn (aluminium-zinc) system, *Bulletin of Alloy Phase Diagram*, 4(1), (1983) 55-73.

59. Shepard, E.S., Aluminium-zinc alloys, *The Journal of Chemical Physics,* 9 (1905) 504-512.

60. Ewen, D. and Turner, T. The aluminium-zinc alloys, *Journal of the Institute of Metals,* 4 (1910) 140-156.

61. Owen, E.A. and Pickup, L., X-ray study of aluminium-zinc alloys at elevated temperatures, *Philosophical Magazine,* 20 (1935) 761-777.

62. Nayak, A.K., Thermal and quantitative thermal analysis of Al-Zn alloys and determination of the equilibrium diagram of the binary system, *Journal of the Institute of Metals 101*, (1973) 309-314.

63. Martinez-Flores, E. and Torres-Villasenor, G., Hybrid materials based on Zn-Al alloys, Metals, Ceramics and Polymeric Composites for Various Uses, John Cuppoletti (Ed.), (2011) 149-170.

64. Sandoval-Jimenez, A., Negrete, J. and Torres-Villasenor, G., The triclinic high-temperature modification of the α phase of the Zn-Al system, *Materials Research Bulletin*, 34 (14/15) (1999) 2291-2296.

65. Watanabe, H., Fundamental Studies 75S. I. Investigations on the phase diagram of the Al-Zn-Cu System, *Nippon Kinzoku Gakkai Shi*, 21 (1957) 333-337 (in Japanese).

66. Köster, W. and Moeller, K., The constitution and the volume changes of Zn-Cu-Al alloys. The relation of CuAl with the ternary phase, *Zeitschrift für Metallkunde,* 33 (1941) 284-288 (in German).

67. Bauer, O. and Hansen, M., The effect of third metal on the constitution of brass alloy. IV. The effect of Al/A constitution on the ternary system Cu-Zn, *Zeitschrift für Metallkunde*, 24 (1932) 1-6 (in German).

68. Bauer, O. and Hansen, M., The effect of third metal on the constitution of brass alloy. IV. The effect of Al/A constitution on the ternary system Cu-Zn, *Zeitschrift für Metallkunde*, 24 (1932) 73-78 (in German).

69. Bauer, O. and Hansen, M., The effect of third metal on the constitution of brass alloy. IV. The effect of Al/A constitution on the ternary system Cu-Zn, *Zeitschrift für Metallkunde*, 24 (1932) 104-106 (in German).

70. Murphy, S*.,* Solid state reactions in the low-copper part of the aluminium-copper-zinc system, *Zeitschrift für Metallkunde*, 71 (1980) 96-102 (in German).

71. Borggren, U. and Selleby, M., A thermodynamic database for special brass, *Journal of Phase Equilibria*, 24 (2003) 110–121.

72. Van, T.D., Segers, L. and Winand, R., Determination of thermodynamic properties of ternary Al-Cu-Zn alloys by electromotive force method, *Journal of Electrochemical Society*, 141(4), (1994) 927-933.

73. Gebhardt, E., The Zn-corner of the Zn-Al-Cu ternary system, *Zeitschrift für Metallkunde*, 32, (1940) 78-85 (in German).

74. Philips, H.W.L., Al-Cu-Zn in equilibrium diagrams of aluminium alloy systems, *Aluminium Development Association*, (1961) 74-77.

75. Hume-Rothery, W., The Effect of manganese, iron and nickel on the α/β brass, *Philosophical Magazine*, 39, (1948) 89-97.

76. Köster, W. and Moeller, K., The constitution and the volume changes of Zn-Cu-Al alloys. I. The partitioning of the concentration plane at 350ºC, *Zeitschrift für Metallkunde*, 33 (1941) 278-283 (in German).

77. Kandaurov, N.E., Begimov, T.B., Presnyakov, A.A., Melikhov, V.D. and Ashirimbetov, Z. A., Structure of alloys in the γ-region of the copper-aluminum-zinc system at room temperature, *Journal of Theoretical and Applied Physics,* 3 (1972) 269–275.

78. Ashirimbetov, Z.A., Kandaurov, N.E., Kalina, M.M., Melikhov, V.D. and Presnyakov, A.A., Structure and properties of solid solutions of the γ-region of the Cu-Al-Zn system*, Journal of Theoretical and Applied Physics,* 5 (1973) 210-213.

79. Ren, Y.P., Ding, H. and Hao, S.M., Abnormal refining of stepped-annealing microstructure in an Al alloy containing low copper and high zinc, *Journal of Materials Science Letters,* 22 (2003) 433-436.